博 士 学 位 论 文

相对论重离子碰撞中方位角的各向异性和电荷平衡函数的纵向性质

论文作者： 李 娜
指导教师： 吴元芳 唐爱红 许怒
申请学位： 理学博士
专业名称： 粒子物理与原子核物理
研究方向： 相对论重离子碰撞

华中师范大学物理科学与技术学院

二零一零年五月

博士学位论文

DOCTORAL DISSERTATION

A Dissertation for Doctor of Philosophy in Physics

Azimuthal Anisotropy and Longitudinal Property of Charge Balance Function in Relativistic Heavy Ion Collisions

by

Na Li

Co-Supervisor: Yuanfang Wu, Aihong Tang and Nu Xu

Huazhong Normal University

May 2010

摘　　要

夸克胶子等离子体是量子色动力学描述的由（近乎）自由的夸克和胶子组成的一种特殊物质形态。它只存在于高温高密的环境，曾经广泛存在于宇宙诞生后的百万分之几秒内。建造位于美国布鲁克海汶国家实验室的相对论重离子对撞机的目的便是通过极高能量的重离子束流对撞，来创造产生夸克胶子等离子体的条件并研究这种物质的特性。

在相对论重离子对撞机上发现夸克胶子等离子体的主要两个依据是集体流和喷注-淬火现象。它们分别描述了软部分子的集体行为和硬部分子穿过介质的能量损失。在碰撞的不同时期，软部分子和硬部分子的产生起着不同的主导作用，其观测量也会相应发生的变化。在本文中，我们研究了不同横动量区间方位角的各向异性。它能够反应在重离子碰撞过程中软硬过程的联系和转化，从而能够帮助我们确定碰撞的时间线，并提供碰撞中动力学的内部信息。

通常情况下，我们用粒子动量分布的傅立叶展开系数来描述方位角的各向异性。在非对心碰撞中，两个碰撞核重叠区域的密度梯度随着系统的膨胀会转化成方位角的各向异性。在低横动量区，二阶系数椭圆流的值与流体力学的预言接近，表明介质的性质可能与理想流体相近。在中横动量区域，人们观测到了“组分夸克标度性”，意味着强子产生于解禁闭的部分子态。然而，考虑实际效应的模型，如海夸克和胶子参与的强子结构，强子内夸克的动量分布等等，都会造成组分夸克标度性的破缺。而在高横动量区，当来自初始碰撞硬散射的硬部分子穿过非对称的重叠区域时，在不同方向上穿越的路径长度不同，因此能量损失也不同，从而导致了方位角的各向异性。

在本文中，我们测量了在200 GeV 下金-金对撞横动量0 到6 GeV/c的π, p ($\bar{p}$), K^0_S, Λ ($\bar{\Lambda}$) 粒子的椭圆流。在p_T/n_q 约等于0.5 到1.5 GeV/c 的区间，π 介子的椭圆流比重子的椭圆流大20% 左右，而考虑真实效应的模型只预言了最多5% 的介质和重子的区别。这是目前为止首次在实验上观测并界定组分夸克标度性的破缺的区域。在我们测量的p_T/n_q和$(m_T - m)/n_q$ 最大的区间，只有考虑了部分子碎裂贡献的联合模型才能描述标度性破缺的程度。这个意味着的部分子碎裂的粒子产生机制此区域开始起主导作用。我们还测量了横动量高至15 GeV/c的带电粒子的椭圆流。直到10 GeV/c 左右，

椭圆流的值仍然是大于0 的。这与部分子能量损失图像的预言一致，也是高密物质产生的证据之一。

测量量v_4/v_2^2被认为是衡量系统理想流体行为的探针之一，它与系统热化的程度直接相关。我们测量了带电粒子和各种已鉴别粒子的v_4/v_2^2，发现在横动量为2 GeV/c 左右的区间，所有粒子v_4/v_2^2 的值都基本上等于1，大于理想流体预测的值。这有可能是由于v_2 和v_4 的起伏造成，也可能意味着系统并未完全热化。

电荷平衡函数是被定义用来测量电荷平衡的观测量。它对于电荷产生机制和随后平衡电荷的扩散十分敏感。因此，电荷平衡函数能够给我们提供单元碰撞中粒子产生过程的内部信息。

在本文中，我们第一次研究了在强子-强子和核-核碰撞中电荷平衡函数的平移不变性。在NA22/EHS 实验组的π^+p and K^+p 22 GeV 碰撞中，我们发现电荷平衡函数在全快度区间是平移不变的。也就是说，$B(\delta y|y_{\rm w})$ 和$(1-\delta y/|y_{\rm w}|)$ 的比值在整个相空间中，不依赖于观测窗口的大小和位置。我们同样在STAR/RHIC 实验组的金-金200 GeV的实验中观测到这一纵向性质。为了与实验结果相比较，我们用PYTHIA和AMPT 蒙特-卡洛模型验证了这个结果。

传统意义上，平移不变性指的是单粒子的密度分布不依赖于快度。电荷平衡函数的平移不变性意味着，除了电荷守恒，带电粒子的产生同时受到电荷平衡的约束。并且，末态粒子的电荷关联在纵向洛仑兹变换的坐标系下是不变的。除此之外，这一纵向性质表明电荷平衡函数是一个不受探测器接收度约束的观测量。也就是说，有着不同的快度覆盖范围的不同实验组，他们测量的标度电荷平衡函数，$B_s(\delta\eta)$ 可以进行定量的比较。

电荷平衡函数的宽度被认为可以测量晚期强子化。在NA22/EHS 实验组的π^+p and K^+p 22 GeV 碰撞中，虽然没有QGP的产生，我们发现电荷平衡函数的宽度仍然会随着多重数的增加变窄。为了确定这个效果的影响，我们用PYTHIA 蒙特-卡洛模型模拟了$p+p$碰撞在能量为22, 64, 130, 200 GeV 时电荷平衡函数的宽度。结果表明电荷平衡函数的宽度先随着多重数的增加变窄，在多重数大约大于20 以后，这一依赖性消失。当我们用同样大小的观测窗口测量电荷平衡函数，发现它的宽度不依赖于碰撞能量，这与强子-强子碰撞中瞬间强子化图像的一致。电荷平衡函数的宽度依赖于观测窗口的大小，这与电荷的关联和起伏的结果一致。在STAR/RHIC 实验组的金-金200

GeV 的实验中，电荷平衡函数的宽度随着横动量和碰撞中心度的增加而减少。这一现象与横向径向流相关，它们潜在的联系能够给我们提供相对论重离子碰撞中粒子产生的动力学提供更多的信息。

关键词: 集体流, 组分夸克标度性, 电荷平衡函数，平移不变性，相对论重离子碰撞

Abstract

A Quark-Gluon Plasma(QGP) is a phase of quantum chromodynamics (QCD) which consists of (almost) free quarks and gluons. It only exists at extremely high temperature and/or density, and is believed to indwell in the first few microseconds after the Big Bang. The goal of the Relativistic Heavy-Ion Collider (RHIC) at Brookhaven National Laboratory (BNL) is to create the condition which may lead to the formation of the QGP and study the property of the new kind of matter.

Collective flow and jet quenching are two main results to claim the discovery of QGP at RHIC. They described the collective motions of soft partons and the energy loss of hard partons traversing trough the medium, respectively. The productions of soft and hard partons dominate in different period of a collision, and result in the different behaviors of the observations. In this thesis, we study the azimuthal anisotropy in different p_T range, which can offer the connection and transition between the soft and hard processes. Thus it may help us to map the time line of the heavy ion collisions and give the insight information of the dynamics.

Usually, the azimuthal anisotropy is described by Fourier coefficients of the particle momentum distribution. It comes from the collective expansion of the bulk matter, arising from the density gradient of the overlap region of two colliding nuclei in non-central collision. At low p_T, the 2^{nd} harmonic called elliptic flow, v_2, comes close to values predicted by hydrodynamics, which indicates that the medium behaves like ideal liquid. While at intermediate p_T, the so called number of constituent quark (NCQ) scaling is found, and it implies that hadrons are produced out of a deconfined partonic state by coalescence or recombination. However, the models that take the realistic effects into account, e.g., adding sea quarks and gluons to the hadron structure and considering the momentum distribution of quarks inside hadrons, may lead to the violation of NCQ scaling. At high p_T, when hard partons, resulting from initial hard scatterings, transverse the asymmetrical overlap region, they experience different path lengths and therefore

different energy loss which leads to an azimuthal anisotropy.

In this thesis, we measure elliptic flow of identified particles (π, p ($\bar{p}$), K^0_S, Λ ($\bar{\Lambda}$)) up to 6 GeV/c in Au + Au collisions at $\sqrt{s_{NN}}$ = 200 GeV. A deviation from the exact NCQ of pions compared to baryons by approximately 20% from 0.5 up to $p_T/n_q \simeq 1.5$ GeV/c, while models with realistic effects included can only explain a deviation up to 5% from a meson-baryon difference.It is so far the first observation of breaking of NCQ scaling in experiment. Since the Coalescence models require a significant fragmentation contribution to account for the large deviation from scaling at the upper end of the measured p_T/n_q and $(m_T - m)/n_q$ range. This suggests that fragmentation may kick in and becomes more dominant in this region. We also measure v_2 for charged particles up to 15 GeV/c. The sizable v_2 has been observed up to p_T = 10 GeV/c. This is consistent with the scenario of parton energy loss, which is also the evidence for the formation of very dense matter.

The ratio v_4/v_2^2 is proposed as a probe of ideal hydrodynamic behavior, and it is directly related to the degree of thermalization. The measured ratio v_4/v_2^2 is studied for both charged particle and identified particles. We find that the ratio v_4/v_2^2 is about 1 when p_T is about 2 GeV/c for all the particles, which is larger than the ideal hydrodynamic prediction. This may be due to the fluctuation of the measured v_2 and v_4, but also may indicate the incomplete thermalization of the system.

The charge balance function (BF) is an observable specifically designed to measure the charge balance. It is sensitive to the mechanisms of charge formation and the subsequent relative diffusion of the balancing charges. Therefore, it can provide insight into the particle production processes in elementary collisions.

In this thesis, it is the first time to observed the boost invariance of BF in both hadron-hadron and nuclear-nuclear collisions. In π^+p and K^+p collisions from NA22/EHS at $\sqrt{s_{NN}}$ = 22 GeV, the BF is found to be invariant under longitudinal boost over the whole rapidity (y) range of produced particles ($-5 < y < 5$), i.e., the ratio of $B(\delta y|y_{\rm w})$ to $(1 - \delta y/|y_{\rm w}|)$ is independent of the observed window, $|y_w|$, and corresponds to the BF of the whole rapidity range. Such longitudinal property is also observed in Au + Au

collisions from STAR/RHIC at $\sqrt{s_{NN}} = 200$ GeV within a relatively wide pseudorapidity (η) coverage ($|\eta| < 1.3$). Furthermore, the boost invariance of BF is observed in PYTHIA and the AMPT Monte Carlo models for the whole phase space.

Conventionally, boost invariance refers to single particle density being independent of rapidity. The boost invariance of BF means that besides the charge conservation, the production of charged particles are constrained by charge balance at the same time, and the charge correlation between final state particles is the same in any longitudinally-Lorentz-transformed frame. Moreover, the BF can be considered as a good measurement which free from the restriction of finite longitudinal acceptance, i.e, the scaled BF, $B_s(\delta\eta)$, can be quantitively compared from different experiments with different pseudorapidity coverages.

It is argued that the width of charge balance function, $\langle\Delta y\rangle$ ($\langle\Delta\eta\rangle$), can be considered as a probe of late hadronization. In π^+p and K^+p collisions from NA22/EHS at $\sqrt{s_{NN}} =$ 22 GeV, where no QGP phase space is expected, $\langle\Delta y\rangle$ is found to be narrower as multiplicity increasing. To investigate this trivial effect, we studied $\langle\Delta y\rangle$ in $p + p$ collisions at $\sqrt{s_{NN}} = 22$, 64, 130, 200 GeV using PYTHIA Monte-Carlo generator. The result shows that the width of BF first decreases with increasing multiplicity, and it changes little when multiplicity is about larger than 20. When the same size of observation window is used, the width of BF is independent of colliding energy, which is consistent with expectation of instantaneous hadronization in hadron-hadron collisions. Also, $\langle\Delta y\rangle$ is found sensitive to the size of observed windows, and it is consistent with charge correlation and fluctuation. In Au + Au collisions from STAR/RHIC at $\sqrt{s_{NN}} = 200$ GeV, $\langle\Delta\eta\rangle$ decreases with increasing transverse momentum and increasing centrality. The origin of these narrowings is associated with transverse radial flow and their possible connections should provide more insight into the particle production dynamics in relativistic heavy ion collisions.

Keywords: collective flow, number of constituent quark scaling, charge balance function, boost invariance, relativistic heavy-ion collision

Table of Contents

1 Introduction **1**

2 Relativistic Heavy Ion Collisions **6**

2.1 Experimental observations 7

2.1.1 Hard probes 7

2.1.2 Collective flow 10

2.1.3 Correlations 19

2.2 Models 23

3 Experimental Set-up **26**

3.1 RHIC 26

3.2 The STAR Experiment 27

3.2.1 STAR TPC 29

3.2.2 STAR FTPCs 32

4 Analysis Method **33**

4.1 Event and track selection 33

4.2 Particle Identification 37

4.3 K^0_S and Λ Reconstruction 39

4.4 Standard event plane method 43

4.4.1 Fourier expansion 43

4.4.2 Event plane determination 44

4.4.3 Detector effect 45

4.5 Invariant Mass Method 50

4.6 Cumulant Method 52

4.6.1 Integral v_2 . . . 52
4.6.2 Differential v_2 . . . 54
4.7 Mixed Harmonics method . . . 55

5 Results I: Azimuthal anisotropy . . . 57
5.1 The 2^{nd} order anisotropic flow v_2 . . . 57
5.1.1 Centrality dependence and non-flow effect . . . 57
5.1.2 Particle species dependence . . . 61
5.1.3 Number of constituent quark scaling of v_2 . . . 65
5.2 The 4^{th} order anisotropic flow v_4 . . . 70
5.2.1 Centrality dependence and non-flow effect . . . 70
5.2.2 Particle species dependence . . . 73
5.2.3 Number of constituent quark scaling of v_4 . . . 74
5.3 Comparison with ideal hydrodynamic . . . 75
5.4 Summary . . . 79

6 Results II: Longitudinal property of Charge Balance Function . . . 81
6.1 Boost invariance of charge balance function . . . 81
6.1.1 Hadron-hadron collisions . . . 81
6.1.2 Nucleus-nucleus collisions . . . 83
6.1.3 Transverse momentum dependence . . . 86
6.1.4 Centrality dependence . . . 87
6.1.5 Model investigation . . . 88
6.2 The width of charge balance function and delay hadronization . . . 93
6.2.1 Multiplicity dependence . . . 93
6.2.2 Energy Dependence . . . 94
6.2.3 Transverse momentum and centrality dependencies . . . 96

6.3 The relation with charge correlation and fluctuation 98

6.4 Summary 100

7 Outlook 102

7.0.1 Test thermalization 102

7.0.2 Beam energy scan 103

References 106

Presentations and publication List 111

Acknowledges 114

List of Figures

1.1 Standard Model of Elementary Particles 1
1.2 QCD effective coupling α_s 2
1.3 Color Screen of confining potential 3
1.4 Lattice QCD calculation 4
1.5 QCD phase diagram 5

2.1 Heavy Ion Collision 6
2.2 Hard Probe 8
2.3 Anisotropy 10
2.4 Coordinate System 11
2.5 v_2 vs p_T 13
2.6 NCQ scaling from Run II 13
2.7 v_2/ε vs $\frac{1}{S}dN/dy$ 15
2.8 Knudsen fit 16
2.9 Azimuthal shape 17
2.10 v_2 and v_4 vs p_T 18
2.11 Ratio v_4/v_2^2 19
2.12 Clocking hadronization 20
2.13 Balance Function from STAR 21
2.14 Balance Function from NA49 22
2.15 Time evolution of initial transverse energy density 24

3.1 RHIC complex 26
3.2 STAR detector perspective view 28
3.3 STAR detector cutaway side view 29

3.4 STAR TPC 30
3.5 Subsector 30
3.6 Anode pad 31
3.7 STAR FTPCs 32

4.1 Reference multiplicity distribution and centrality definition of Run IV . . 35
4.2 Global reference multiplicity distribution and centrality definition of Run VII 37
4.3 dE/dx distribution 38
4.4 The relative dE/dx peak position 39
4.5 $n\sigma_p$ distribution 40
4.6 V0 decay topology 42
4.7 Invariant mass distribution 43
4.8 TPC ϕ and ϕ weight Distribution 46
4.9 TPC event plane distribution 47
4.10 FTPC event plane distribution 47
4.11 v_2 resolution 49
4.12 Event plane method 50
4.13 Invariant mass method 51
4.14 v_4 resolution 55

5.1 Charged particle v_2 20-60%. 58
5.2 Centrality dependence of charged particle v_2. 60
5.3 Pion and Proton v_2. 61
5.4 Kshort and Lambda v_2. 62
5.5 Identified particle v_2 63
5.6 FTPC event plane v_2. 64

5.7 NCQ Scaling 65
5.8 Centrality dependence of v_2/n_q vs p_T/n_q 67
5.9 Centrality dependence of v_2/n_q vs $(m_T - m)/n_q$ 67
5.10 NCQ Scaling. 69
5.11 Minimum bias v_4. 71
5.12 Centrality v_4. 72
5.13 Minimum bias V0 v_4 73
5.14 Ks and Lambda v_4 74
5.15 v_4 Scaling 75
5.16 v_4/v_2^2 for Charged particle. 76
5.17 v_4/v_2^2 for PID particle. 77

6.1 $B(\delta y|Y_{\rm w})$ from NA22 82
6.2 dN/dy from NA22 83
6.3 $B(\delta y|Y_{\rm w})$ and $B(\delta y|\infty)\cdot(1-\frac{\delta y}{Y_{\rm w}})$ from NA22 84
6.4 $B(\delta\eta|\eta_{\rm w})$ and $B_s(\delta\eta)$ from STAR 84
6.5 Charge conservation test from STAR 85
6.6 p_T dependence of Balance Function from STAR 86
6.7 Centrality dependence of balance function from STAR 87
6.8 $B(\delta\eta|\eta_{\rm w})$ from PYTHIA 89
6.9 $B(\delta\eta|\eta_{\rm w})$ from AMPT 90
6.10 p_T dependence from PYTHIA 91
6.11 p_T dependence from AMPT 92
6.12 Multiplicity dependence of balance function from NA22 93
6.13 Energy dependence of δy from PYTHIA 95
6.14 Rapidity distribution from PYTHIA 95

6.15 Energy dependence of δy in $-3 \leq y \leq 3$ from PYTHIA 96

6.16 p_T and centrality dependence of the width of Balance function from STAR 97

6.17 Correlation function R from PYTHIA 98

6.18 $D(Q)/4$ from NA22 99

List of Tables

4.1 Trigger and events selection 33

4.2 Trigger and events selection 34

4.3 Centrality definition for Run IV 34

4.4 Centrality definition for Run VII 36

4.5 K^0_S and Λ ($\bar{\Lambda}$) weak decay 40

4.6 K^0_S cuts 41

4.7 Λ ($\bar{\Lambda}$) cuts 42

4.8 Flow track selection 45

6.1 Multiplicity dependence of $\langle \delta y \rangle$ 94

6.2 The widths $\langle \delta\eta \rangle$ of the $B_s(\delta\eta)$ 97

CHAPTER 1

Introduction

Scientists always work on finding the most fundamental bricks building up the world. The Standard Model of particle physics is a theory of the fundamental interactions and the elementary particles that take part in these interactions. In the Standard Model, as shown in Figure 1.1, the quarks, leptons are elementary particles which make up all visible matter in the universe while particles transmit forces among each other by exchanging gauge bosons.

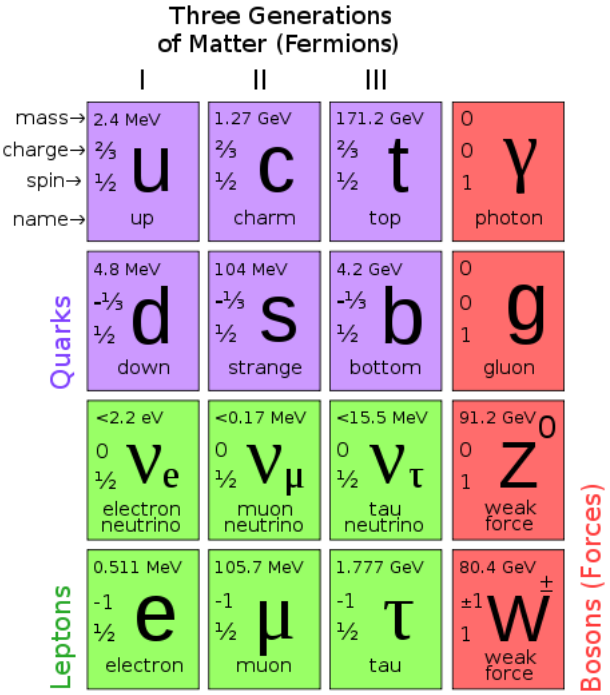

Figure 1.1: The Standard Model of elementary particles, with the gauge bosons in the rightmost column.

Quantum ChromoDynamics (QCD) [Dis03a] is an important part of the Standard Model of particle physics. It is a theory of the strong interaction (color force), a fun-

damental force describing the interactions of the quarks and gluons making up hadrons. Different from Quantum ElectroDynamics (QED) - the gauge theory describing electromagnetic interaction, QCD is based on the non-Abelian gauge group SU(3), with gauge bosons (color octet gluons), and hence the gluons could have self-interacting. This results in a negative β-function and asymptotic freedom at high energies and strong interactions at low energies.

There are two peculiar properties in QCD theory: 1) asymptotic freedom and 2) confinement. Asymptotic freedom means in very high-energy reactions, quarks and gluons interact very weakly. The effective QCD coupling constant α_s is used to describe the strength of interaction. The $\alpha_s = g_s^2/4\pi$ depends on the renormalization scale [Bet03a], and can be written as:

$$\alpha_s(\mu) \approx \frac{4\pi}{\beta_0 \ln(\mu^2/\Lambda^2_{\rm QCD})}, \tag{1.1}$$

where β_0 is a constant dependent on the number of quarks with mass less than μ and $\Lambda_{\rm QCD}$ is one of the important QCD parameters.

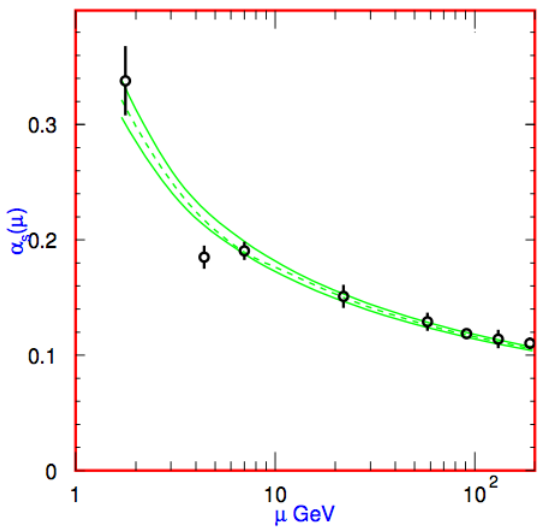

Figure 1.2: QCD effective coupling α_s as a function of momentum transfer scale μ. The figure is taken from [Ams08a].

Figure 1.2 shows α_s at different momentum transfer scale [Ams08a]. From the plot we can see that the coupling constant decreases with increasing energy, and it means that the strong force between quarks becomes weaker at larger distances when they are

separated. $\alpha_s \to 0$ as $\mu \to \infty$ and QCD becomes strongly coupled at $\mu \sim \Lambda_{\rm QCD}$. The α_s has to be determined from experiment. The world average α_s at common energy scale $\mu = M_Z$ is $\alpha_s(M_Z) = 0.1176 \pm 0.002$ [Eid04a], and the QCD scale $\Lambda_{\rm QCD} \sim 200$ MeV.

QCD is formulated in terms of quarks and gluons while the experimentally observed states are hadrons. As mentioned previously, the method of perturbation QCD (pQCD) theory is appropriate in the high-momentum scale, short-distance regime in principal. While when the partons are strongly coupled, pQCD can not be used and some other methods are needed, e.g., Lattice QCD [Wil74].

Confinement means that there is force between quarks as they are separated. The confinement properties can be described by potential:

$$V_0(r) \sim \sigma r, \tag{1.2}$$

where r is the separation between quarks and the string tension σ measures the energy per unit separation distance. At sufficiently high density, we expect color screening to set in and the potential Eq. 1.2 becomes

$$V(r) \simeq \sigma r[\frac{1-\exp(-\mu r)}{\mu r}], \tag{1.3}$$

where μ is the color screening mass [Sat00a].

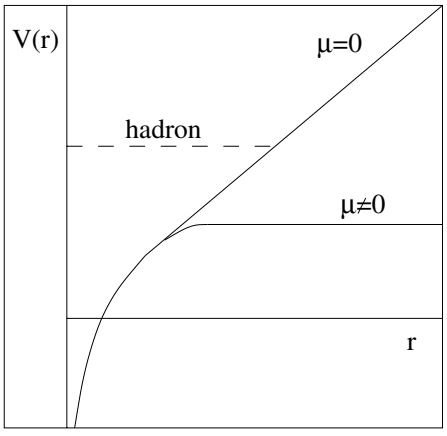

Figure 1.3: Color screening of confining potential. The calculations are from [Sat00a].

The potential between quarks also depends on the temperature. Figure 1.3 shows the potential as a function of r for different temperature. At low temperature, the

potential increases linearly with the distance between quarks, which means that the quarks are bounded within the hadrons. When the temperature is higher than the confined temperature, the confinement potential is "melted", then quarks are free. So far we have never observed a so called deconfined quark which means the quark can move in a volume much larger than the volume of a hadron.

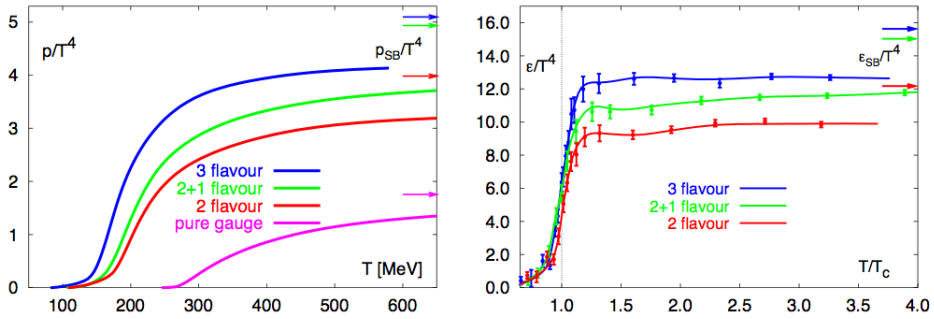

Figure 1.4: Results from lattice QCD calculation for the pressure (left) and energy density (right) divided by T^4 of strongly interacting matter as a function of temperature. The calculations are from [Kar02a]

Recent advances in the formulation of thermodynamical lattice QCD at finite temperature and density however, suggests that when sufficiently high temperature and density are reached, quarks become effectively deconfined. Figure 1.4 shows the pressure and the energy density scaled by T^4 (where T is the system temperature). Both variables rise as T increases. The magnitude of ε/T^4 reflects the number of degrees of freedom in the thermodynamic system, and it quickly increases at a critical temperature T_c. The rise corresponds to a transition in the system to a state where the quarks and gluons have become relevant degrees of freedom. The pressure changes relatively slowly compared to the increase of the energy density, ande it means that the pressure gradient in the system is significant reduced during the phase transition.

A Quark-Gluon Plasma (QGP) is a phase of QCD existing at extremely high temperature and/or density. Figure 1.5 shows a schematic QCD phase diagram. The behavior of nuclear matter, as a function of temperature and baryon density, is governed by its equation of state (EOS). Conventional nuclear physics focuses on the lower left portion of the diagram at low temperature and near normal nuclear matter density. It is predicted

that a hadron-quark phase transition will occur if the temperature or baryon density is high enough. The QGP phase is believed to exist in the first few microseconds after the Big Bang (the high temperature case) and possibly exist in the cores of heavy neutron stars (the high density case).

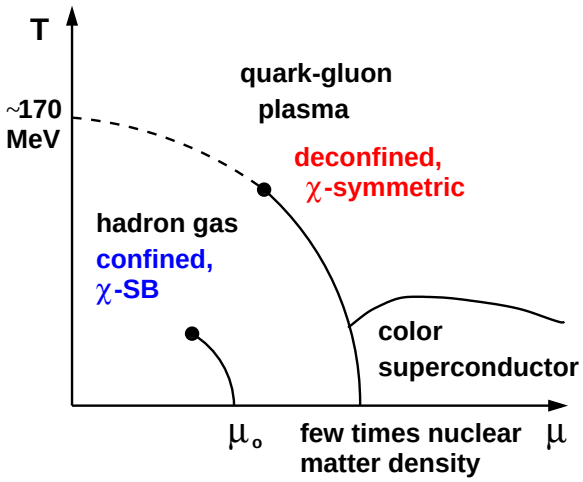

Figure 1.5: Sketch of the QCD phase diagram. The figure is from [Kar06a]

The goal of heavy ion physics is to create the condition which may lead to the formation of the QGP and study the property of the new kind of nuclear matter and also try to explore the phase transition and map the phase diagram.

CHAPTER 2

Relativistic Heavy Ion Collisions

The main goal of building the Relativistic Heavy Ion Collider (RHIC) in Brookhaven National Laboratory (BNL) is to create a condition with extreme high temperature and density which may lead to the matter of deconfined quarks and gluons. The new form of matter created in the laboratory is believed to exist at very early stage of universe evolution. Studying QGP formation will help us to understand the fundamental structure of the matter and evolution of our universe.

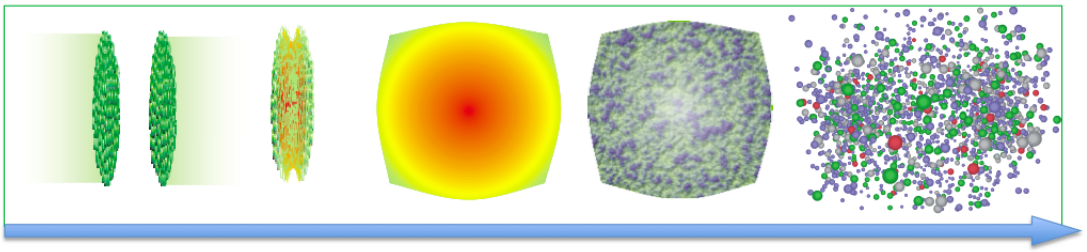

Figure 2.1: A schematic picture of the evolution of a relativistic heavy ion collision.

The evolution of a relativistic heavy-ion collision is shown schematically in Figure 2.1. The two nuclei can be described as two thin disks due to the Lorentz contraction when they are approaching each other at near the speed of light. At the collision, protons and neutrons in the overlapping region of two nuclei experience strong multiple scattering and the longitudinal kinetic energy is transformed into the local energy concentrated at the collision point with extremely high temperature. Nucleons will dissolve at such an high temperature and quarks and gluons are deconfined. The strong interactions between quarks and gluons are expected to be sufficient to lead to local thermal and chemical equilibrium after a very short time, and then the QGP is formed. At this stage the partonic scatterings with high momentum transfer are dominant and high

energy leptons and jets are created, such as $q\bar{q}$ pairs, gluons and direct photons. As the system expands rapidly and cools down, mesons and baryons start to be created by fragmentation and quark coalescence. The fireball then reaches chemical freeze-out, evolving into an strongly interacting hadronic gas. After that, the system reaches kinetic freeze-out and particles stop interacting with each other and the collision ends at this point. The freeze-out hadrons move freely till they reach the detectors.

It is hard to directly determine whether the QGP is produced since its lift time is too short. Experimentally it is studied by looking at the information provided by the particles that shower out from the collision.

2.1 Experimental observations

The QGP state formed in nuclear collisions is a transient rearrangement of the correlations among quarks and gluons. Heavy ion collisions at relativistic energies offer a unique environment for the creation and study of the QGP phase in laboratory. Lots of probes have been proposed [Bas99a, Ada05a] to study the novel state of matter for experimental aspects. A QGP is taken to be a (locally) thermalized state of matter in which quarks and gluons are deconfined, so that color degrees of freedom become manifest over the nuclear, rather than merely nucleonic , volumes. The thermalization and deconfinement are the two experimental concentrations to claim the QGP formation. In this section, we review some experimental probes and results.

2.1.1 Hard probes

In relativistic heavy ion collisions, the high p_T particles are believed to be produced from hard scattering processes and parton fragmentation. The interaction of the hard partons (jet) with the medium can provide a class of unique, penetrating probes. When the hard partons (jets) interact with the medium, they suffer energy lose. The amount of the energy loss should reflect the gluon density of the medium. The softened partons fragmenting into hadrons will lead to the suppression of high p_T hadrons in the final

state compared to that of no medium effects ($p + p$ collisions). This effect is so called jet quenching.

Left panel in Fig. 2.2 shows the azimuthal distribution of hadrons with $p_T > 2$ GeV/c relative to a trigger hadron ($p_T^{\rm trig} > 4$ GeV/c). A hadron pair from a single jet will generate the near-side correlation T ($\Delta\phi \approx 0$) as observed in $p + p$, $d +$ Au and Au + Au collisions. While a hadron pair from back-to-back di-jets will generate the away-side correlation ($\Delta\phi \approx \pi$) as observed in $p + p$ and $d +$ Au collisions. The significant disappearance of back-to-back correlation is observed in central Au + Au collisions.

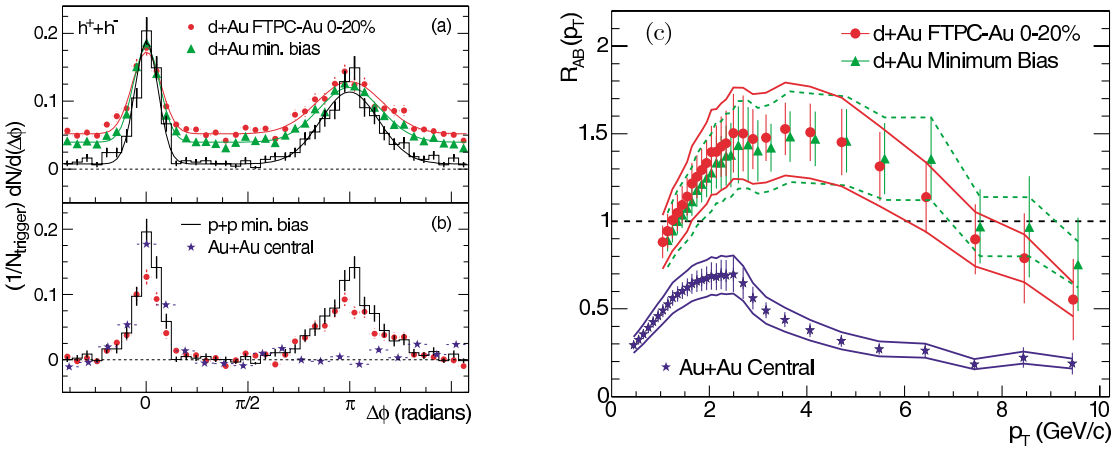

Figure 2.2: (a) Two-particle azimuthal distributions in $d +$ Au collisions for minimum bias and central data, and for $p + p$ collisions. (b) Comparison of two-particle azimuthal distributions in central $d +$ Au collisions to in $p + p$ and Au + Au collisions. (c) $R_{AB}(p_T)$ for minimum bias and central $d +$ Au collisions, and central Au + Au collisions. The normalization uncertainties are shown as shaded bands, which are highly correlated point-to-point and between the two d + Au distributions. The plot is from [Ada05a].

Modifications of high p_T particle production in nuclear collisions with respect to $p + p$ interactions are given by the nuclear modification factor defined by:

$$R_{AB}(p_T) = \frac{d^2\sigma_{AB}/dp_T d\eta}{< N_{\rm bin} > d^2\sigma_{pp}/dp_T d\eta}, \tag{2.1}$$

where A and B are colliding nuclei, $d^2\sigma_{pp}/dp_T d\eta$ is the inclusive cross section measured in $p + p$ collisions and $< N_{\rm bin} >$ accounts for the geometrical scaling from $p + p$ to nuclear collisions as described by the Glauber model. If an Au + Au collision is an incoherent superposition of p+p collisions, the ratio would be unity. Nuclear effects such

as energy loss and shadowing will reduce the ratio below unity while anti-shadowing and the Cronin effect lead to a value about unity. The Cronin effect, an enhancement of the particle yield at intermediate p_T, is usually attributed to multiple soft parton scatterings before a hard interaction of the parton (p_T broadening). The shadowing of the structure function modifies the particle yield depending on the parton momentum fraction, $x_{\rm Bj}$, probed in the partonic scattering. An alternative model of the initial state of a nucleus is the gluon saturation or color glass condensate(CGC) in which the gluon population at low $x_{\rm Bj}$ is limited by non-linear gluon-gluon dynamics. Those effects in Au + Au collisions can be isolated through studies of d + Au collisions. Figure 2.2 shows R_{AB} for charged particles in d + Au and central Au + Au collisions. An enhancement is observed in d + Au collisions instead of suppression. Therefore, the suppression in Au + Au is due to final state effect and indicates that a dense medium is created in central Au+Au collisions.

In addition to the nuclear modification factor, R_{AB}, di-hadron azimuthal correlations can be used to study the effect of jet quenching. The azimuthal correlations of two high p_T particles from jets are expected to show a narrow near-side correlation and a broader away-side correlation. However, in the case of strong jet quenching the away-side jet would be suppressed by energy loss in the traversed medium. Figure 2.2(c) shows the azimuthal correlations of high p_T particles with 2 GeV/c < p_T < $p_T^{\rm trig}$ relative to the trigger particle with $4 < p_T < 6$ GeV/c in p + p, d + Au and Au + Au collisions. The near-side and away-side peaks are clearly visible in p + p, minimum bias and central d + Au collisions. In central Au + Au collisions, a similar near-side peak appears while the away-side peak has disappeared. The suppression only occurs in Au + Au collisions and shows that this is a final state effect as expect from partonic energy loss mechanisms.

These results provide experimental evidence that the hot and dense medium has bee formed at RHIC.

2.1.2 Collective flow

The flow refers to a collective expansion of the bulk matter. It arises from the density gradient from the center to the boundary of the created fireball in nuclear collisions. Interactions among constituents push matter outwards; frequent interactions lead to a common constituent velocity distribution. This so-called collective flow is therefore sensitive to the strength of the interactions. Collective flow is additive and thus accumulated over the whole system evolution, making it potentially sensitive to the equation of state of the expanding matter [Bas99a, Sto81a, Sto86a, Sor97b, Oll92a, Rei04a]. At lower energies, the collective flow reflects the properties of dense hadronic matter, while at RHIC energies, a large contribution from the pre-hadronic phase is anticipated.

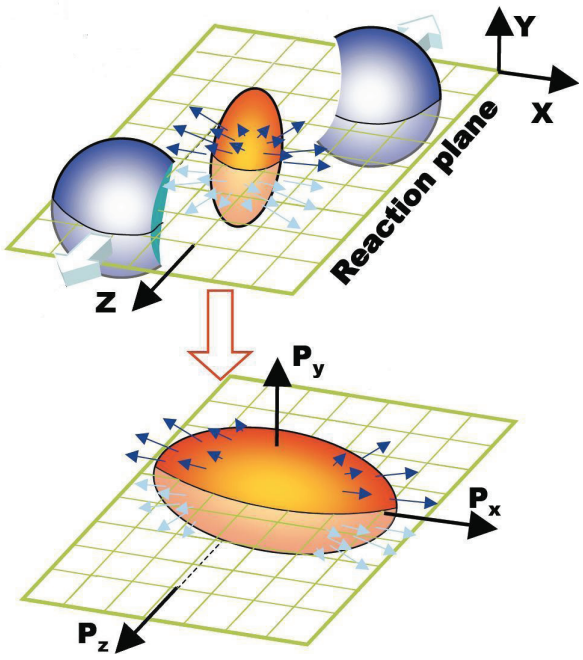

Figure 2.3: Sketch of an almond shaped fireball, where z direction is the beam direction and x is the direction of impact parameter b.

In heavy ion collisions, the size and the shape of the colliding region depend on the distance between the centers of the nuclei in the transverse plane (impact parameter b). The plane is called the reaction plane and defined by the beam direction and the impact parameter ($x - z$ plane in Fig.2.4). In non-central collisions, the overlapping reaction

zone of two colliding nuclei is not spherical (shown in Fig.2.3). Their overlap area in the transverse plane has a short axis parallelling to the impact parameter, and a long axis perpendicularing to it. Due to the pressure gradient, this almond shape of the initial profile is converted into a momentum asymmetry, thus more particles are emitted along the short axis [Oll92a], as shown in Figure 2.3. The spatial anisotropy is largest in the early evolution of the collision. As the system expanding, it becomes more spherical, and this driving force quenches itself. Therefore, the momentum anisotropy is particularly sensitive to the early stages of the system evolution [Sor97a]. In addition, since the anisotropic flow depends on rescattering, it is sensitive to the degree of thermalization of the system.

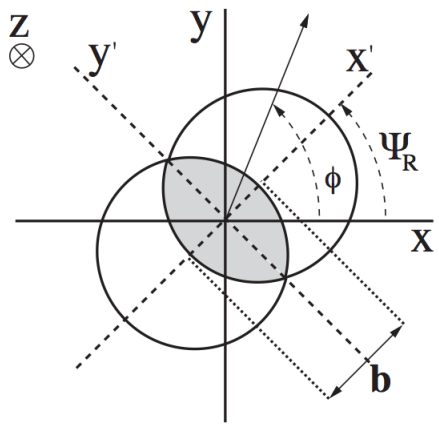

Figure 2.4: Sketch of an almond shaped fireball, where z direction is the beam direction and x is the direction of impact parameter b.

The initial spatial anisotropy in the reaction region can be characterized by the eccentricity defined as:

$$\varepsilon_{\text{std}} = \frac{\langle y^2 - x^2 \rangle}{\langle y^2 + x^2 \rangle}, \tag{2.2}$$

where x and y are the spatial coordinates in overlapping region as shown in Figure 2.4. However, the nucleons participating in the collision could fluctuate from event to event even at fixed impact parameter. Therefore, the center of the overlap zone can be shifted and the orientation of the principal axes of the interaction zone can be rotated with respect to the conventional coordinate system. To modify this effect, the participant

eccentricity $\varepsilon_{\rm part}$ is defined as:

$$\varepsilon_{\rm part} = \frac{\langle y'^2 - x'^2 \rangle}{\langle y'^2 + x'^2 \rangle}, \tag{2.3}$$

where the eccentricity is calculated relative to the new coordinate system which is defined by the major axis of the initial system.

The average values of $\varepsilon_{\rm std}$ and $\varepsilon_{\rm part}$ are rather similar except the most peripheral collisions for interactions of heavy nuclei such as Au + Au. However, for smaller systems, fluctuations in the nucleon positions become quite important for all centralities and the average eccentricity can vary significantly [Alv07a].

The anisotropy in momentum space is usually studied by the Fourier expansion of azimuthal angle distribution of produced particles with respect to the reaction plane [Oll92a, Oll93a, Vol96a]:

$$E\frac{d^3N}{d^3p} = \frac{1}{2\pi}\frac{d^2N}{p_T dp_T dy}(1 + \sum_{n=1}^{\infty} 2v_n \cos[n(\phi - \Psi_r)]), \tag{2.4}$$

where p_T and y are the transverse momentum and rapidity of a particle, ϕ is its azimuthal angle, v_n is the $n^{\rm th}$ harmonic coefficient and Ψ_r is the azimuthal angle of the reaction plane in the laboratory frame (see Fig. 2.4 for the definition of the coordinate system). The different harmonic coefficients represent different aspects of the global flow behavior. v_1 is so called directed flow, v_2 is so called elliptic flow since it is the largest component characterizing the ellipse shape of the azimuthal anisotropy, and v_4 is the $4^{\rm th}$ harmonic.

Elliptic flow, v_2, is the second harmonic coefficient in the description of particles azimuthal distribution w.r.t. the reaction plane by Fourier expansion. It is argued that the centrality dependence of v_2 can be used to probe local thermodynamic equilibrium [Vol00a] and might provide a indication of the phase transition [Sor99a]. It gains a lot of interests [Ada05a, Adc03a] in heavy ion collisions.

Figure 2.5 shows the measured v_2 distribution as a function of p_T from minimum bias data in Au + Au collisions at $\sqrt{s_{NN}} = 200$ GeV from STAR and PHENIX experiments [Ada05b, Adl03b]. Identified particle v_2 are shown for $\pi^{\pm}$, K^0_S, p ($\bar{p}$) and Λ ($\bar{\Lambda}$). At a given p_T , the heavier particle has the smaller v_2 than the lighter particle up to 1.6 GeV/c. This characteristic mass-ordering comes from radio flow which is predicted by

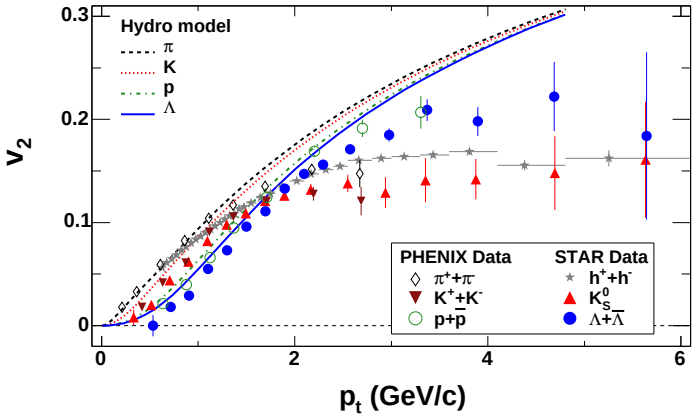

Figure 2.5: v_2 as a function of p_T for $h^{\pm}$ (stars), $\pi^{\pm}$ (diamonds), p ($\bar{p}$) (circles), K^0_S (triangles) and Λ ($\bar{\Lambda}$) (inverse triangles) in Au + Au minimum bias collisions at 200 GeV. Hydro calculations are shown as different kinds of curves. The figure is from [Ada05b].

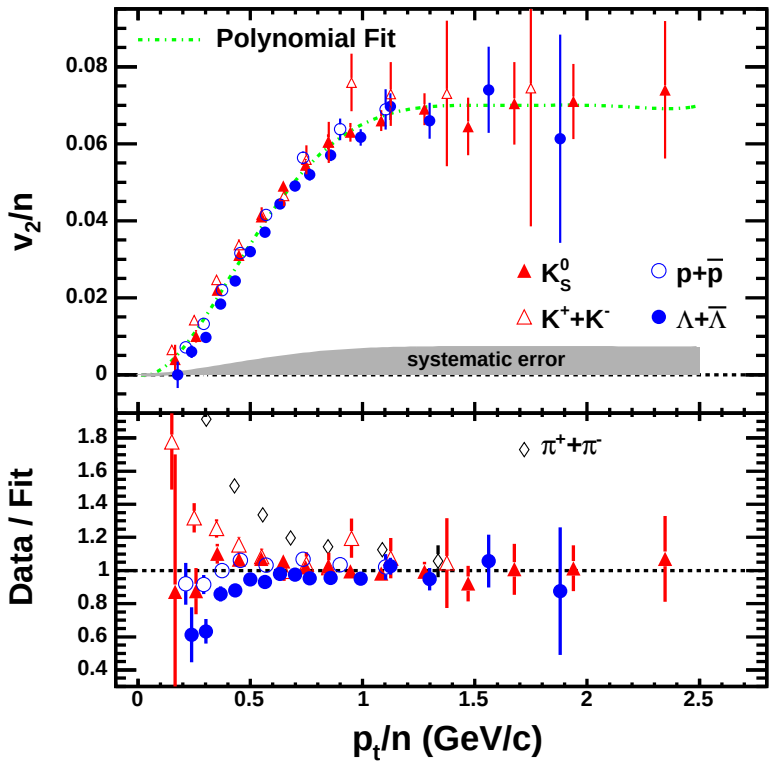

Figure 2.6: Number of constituent quark (n_q) scaled v_2 as a function of scaled p_T for $\pi^{\pm}$ (diamonds), p ($\bar{p}$) (circles), K^0_S (triangles) and Λ ($\bar{\Lambda}$) (inverse triangles)at 200 GeV Au+Au minimum bias collisions. The figure is from [Ada05b].

the hydrodynamic calculation [Huo01a, Huo03a, Huo05a] represented by the dot-dashed lines. It indicates the collectivity has been developed at RHIC. The hydrodynamics calculations achieve agreement with data. This is especially a critical test in assessing QGP claims since the hydrodynamical calculations assume local thermalization while the system is most likely to reach thermalization in central collisions.

A particle type (baryon versus meson) difference in $v_2(p_T)$ was observed for $\pi^{\pm}$, p ($\bar{p}$), K^0_S and Λ ($\bar{\Lambda}$) at the intermediate p_T region. This particle type dependence of the $v_2(p_T)$ is naturally accounted for by quark coalescence or recombination models [Vol02a, Fri04a, Hwa04a, Gre03a]. In these hadronization models, hadrons are formed dominantly by coalescing massive quarks from a partonic system with the underlying assumption of collectivity among these quarks. The collectivity among u-, d-, and s- quarks near hadronization are the same, and these models predict a universal scaling of v_2 and the hadron transverse momentum p_T with the number of constituent quarks (n_q). The scaling has previously been observed to hold within experimental uncertainties for the K^0_S and the Λ when $p_T/n_q \geq 0.7$ GeV/c. Figure 2.6 (top panel) shows v_2 as a function p_T for the identified particles in Figure 2.5, where v_2 and p_T have been scaled by the number of constituent quarks (n). A polynomial function has been fit to the shown scaled values. In order to investigate the quality of agreement between particle species, the data from the top panel are scaled by the fitted polynomial function and plotted in the bottom panel. For $p_T/n > 0.6$ GeV/c, the scaled v_2 of $\pi^{\pm}$, p ($\bar{p}$), K^0_S, Λ ($\bar{\Lambda}$) lie on a universal curve within statistical errors. The pion points, however, deviate significantly from this curve even above 0.6 GeV/c. This deviation may be caused by the contribution of pions from resonance decays. Alternatively, it may reflect the difficulty of a constituent-quark-coalescence model to describe the production of pions whose masses are significantly smaller than the assumed constituent-quark masses.

In the low density limit, the mean free path λ is comparable or larger than the system size, and the integrated v_2 is proportional to the spatial anisotropy and the number of rescatterings in the transverse plane:

$$v_2 \propto \varepsilon \frac{1}{S}\frac{dN}{dy}, \tag{2.5}$$

where dN/dy is the multiplicity density and $S = \pi\sqrt{\langle x^2\rangle\langle y^2\rangle}$ is a measure of the initial transverse size of the collision region. The brackets $\langle\cdots\rangle$ denotes an average weighted with the initial density.

Since in the hydro limit, where complete thermalization is expected, the centrality dependence of v_2 is mostly defined by the elliptic anisotropy of the overlapping region of the colliding nuclei, e.g., eccentricity. While v_2 is proportional to eccentricity and the multiplicity in the low density limit. The eccentricity increases while the multiplicity decreases with increasing impact parameter respectively, thus the integrated elliptic flow has its maximum at an intermediate impact parameter.

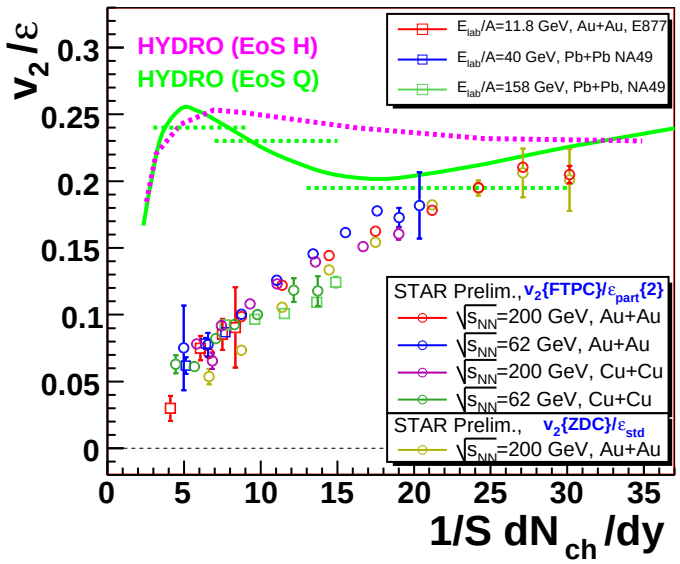

Figure 2.7: Charge particle v_2/ε versus $\frac{1}{S}dN_{\rm ch}/dy$ at AGS, SPS to RHIC energies. The figure is from [Vol06a].

The elliptic flow increases with the increase of particle density. Eventually, it saturates at the hydrodynamical limit, where the mean free path is much less than the geometrical size of the system and complete thermalization is reached. Therefore, v_2/ε is approximately constant [Oll92a]. Figure 2.7 shows charge particle v_2/ε as a function of $\frac{1}{S}dN_{\rm ch}/dy$, and $\frac{1}{S}dN_{\rm ch}/dy$ is the measured charged particle density in midrapidity. At RHIC energies, the results from STAR are presented for Au + Au and Cu + Cu collisions at both 62.4 GeV and 200 GeV. At SPS energies, NA49 measurements are

presented for Pb + Pb collisions at 40A GeV and 158A GeV. At AGS energies, E877 measurements is shown for Au + Au collisions at 11.8A GeV. By dividing v_2 with ε, the effect of initial geometry of the different centralities is supposed to be removed. The particle density increases with centrality and increasing beam energy. The values of v_2/ε fall approximately on a single curve, independent of beam energy or impact parameter. The v_2/ε data shown at the full RHIC energy for near central collisions is close to ideal hydro calculations, and it indicates that the system created in heavy ion collisions evolves towards the thermalization.

On the other hand, if equilibration is incomplete, then eccentricity scaling is broken and v_2/ε also depends on the Knudsen number $K = \lambda/R$, where λ is the length scale over which a parton is deflected by a large angle and R is its transverse size. The centrality dependence of v_2/ε can be described by [Bha05a]:

$$\frac{v_2}{\varepsilon} = \frac{v_2^{\text{hydro}}}{\varepsilon} \frac{1}{1 + K/K_0}, \tag{2.6}$$

v_2/ε is largest in the hydrodynamic limit $K \to 0$. The first order corrections to this limit, corresponding to viscous effects, are linear in K. For a large mean-free path, $v_2/\varepsilon \sim 1/K$ vanishes like the number of collisions per particle which is far from the hydrodynamic limit.

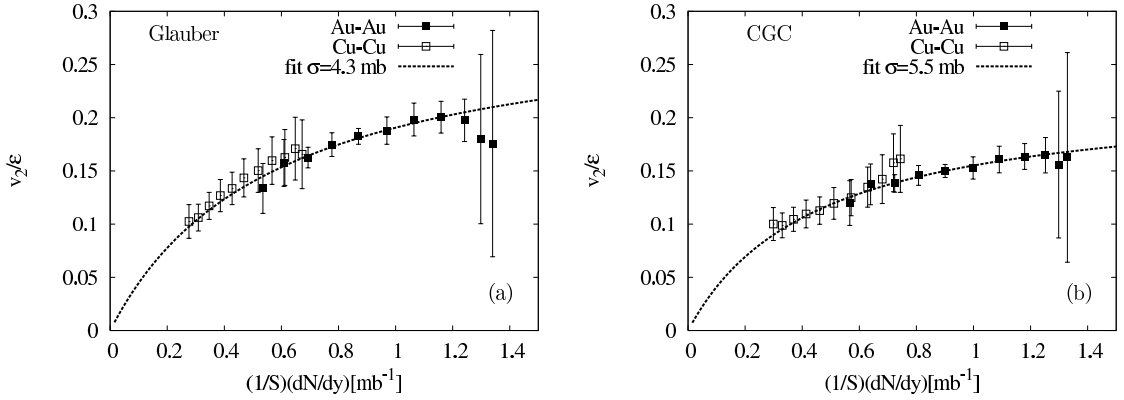

Figure 2.8: Variation of the scaled elliptic flow with the density. The initial conditions are assumed from the (a) Glauber [Mil03a] model and (b) CGC model. The curve is a two-parameter fit using Eq. 2.6 and Eq. 2.8. The figure is from [Oll07a].

Elliptic flow develops gradually during the early stages of the collision. Because of the strong longitudinal expansion, the thermodynamic properties of the medium depend

on the time τ. The average particle density, for instance, decreases like $1/\tau$ [Dum07a].

$$\rho(\tau) = \frac{1}{\tau S}\frac{dN}{dy}, \tag{2.7}$$

where dN/dy denotes the total (charged + neutral) multiplicity per unit rapidity, and S is the transverse overlap area between the two nuclei. The Knudsen number K is defined by evaluating the mean-free path $\lambda = 1/\sigma\rho$ (σ is a partonic cross section) at $\tau = R/c_s$. Thus,

$$\frac{1}{K} = \frac{\sigma}{S}\frac{dN}{dy}c_s. \tag{2.8}$$

Figure 2.8 displays v_2/ε as a function of $\frac{1}{S}\frac{dN}{dy}$ for Au + Au and Cu + Cu collisions at various centralities, with initial conditions of the Glauber and CGC approaches, respectively. For both types of initial conditions, the values of the fit parameters clearly depend on the initial conditions, which has important consequences for the physics. The data for the scaled flow shows a saturate trend at high densities to a hydrodynamic limit, the elliptic flow is at least 25% below the (ideal) "hydrodynamic limit", even for the most central Au + Au collisions.

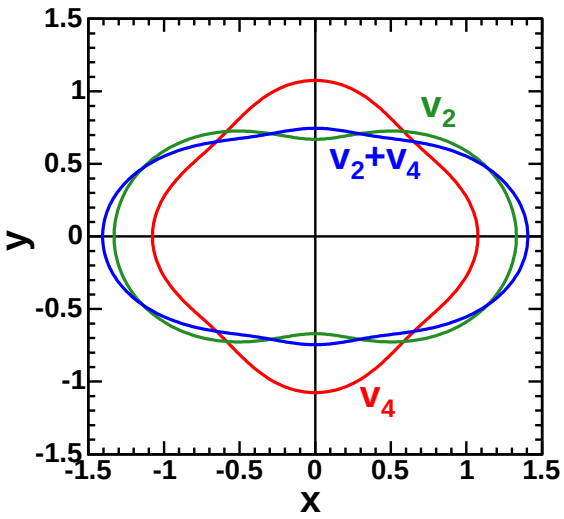

Figure 2.9: A polar graph of the distribution $1 + 2v_2\cos(2\phi) + 2v_4\cos(4\phi)$. Plotted are the distributions for $v_2 = 16.5\%$ showing the waist, $v_4 = 3.8\%$ having a diamond shape, and both coefficients together. The figure is from [Ada05b].

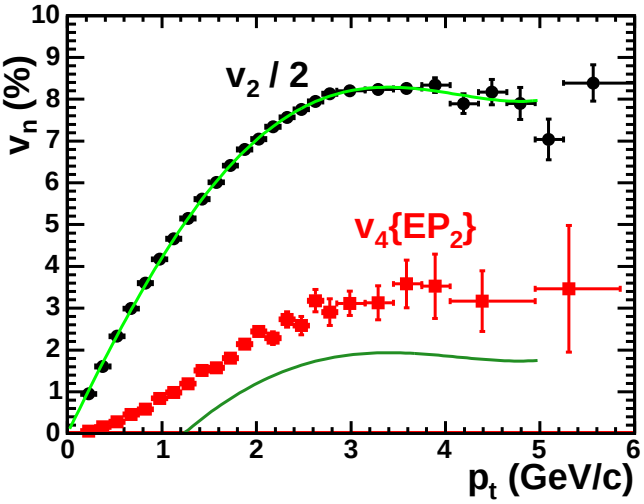

Figure 2.10: v_2 divided by 2, and $v_4\{EP_2\}$ vs. p_T for charged hadrons from minimum bias events. Using a fit to the v_2 values, the lower solid line is the predicted v_4 needed to just remove the "peanut" waist. The figure is from [Ada05b].

v_4 is the fourth harmonic coefficient in the description of particles azimuthal distribution w.r.t. the reaction plane by Fourier expansion.

It is argued that the azimuthal shape in momentum space is no longer elliptic, instead, it becomes "peanut" shaped with large v_2 value [Kol03b] as shown in Figure 2.9. Experimentally we measured the amplitude of v_4 as shown in Figure 2.10 in Au + Au collisions at 200 GeV. v_4 and the scaled v_2 is are shown for comparison. The experimental v_4 values shown in Fig. 2.10 considerably larger than the value which is predicted in [Kol03b] to eliminate the peanut waist.

In ideal hydro calculation, the ratio v_4/v_2^2 will approach to 0.5 at high p_T [Bor06a]. Figure 2.11 shows the result of STAR data and ideal hydro calculation as a function of transverse momentum. The dashed lines are ratio come out of calculations by solving Boltzmann equations with Monte Carlo simulation, with different Knudsen number K. When the Knudsen number is small, it recovers the hydrodynamic limit as indicated the solid line. The plot shows that the system exhibits considerable deviation from ideal hydrodynamic limit ($K \ll 1$), and the data is consistent with a incomplete thermalized system with $K > 0.5$.

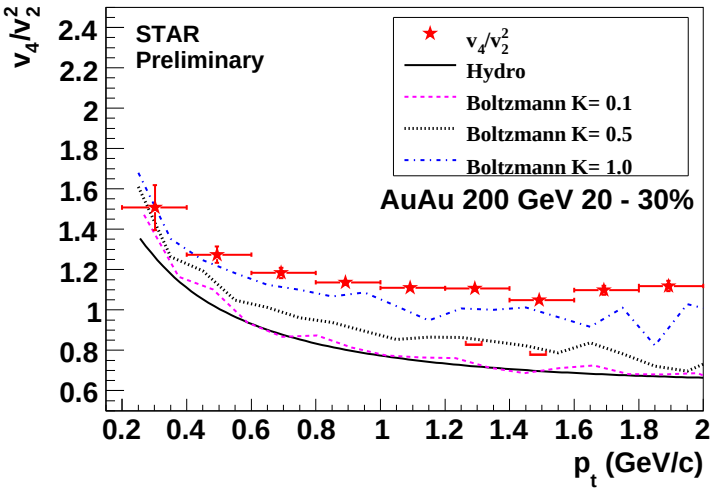

Figure 2.11: The ratio of v_4/v_2^2 as a function of p_T for charged particles at $|\eta| < 1.3$ in Au + Au collisions at $\sqrt{s_{NN}} = 200$ GeV. The brackets show the systematic uncertainty of non-flow effect. The curves correspond to two hydrodynamic calculations. The figure is from [Tan08a].

2.1.3 Correlations

The observables related to correlations [Jeo00a, Asa02a, Asa00a] are considered sensitive to QGP state. The study of correlations is expected to provide us additional information on particle production mechanism in high energy nuclear collisions.

The electric charge balance function (BF) is sensitive to whether the transition to a hadronic phase was delayed, as expected if the quark-gluon phase were to persist for a substantial time [Bas00b]. It is defined in terms of a combination of four different conditional densities of charged hadrons, and measures how the net charge in the phase space is rearranged if the charge at a selected point changes. Projected on to the pseudorapidity difference $\delta\eta = \eta_1 - \eta_2$ of two charged particles in a given pseudorapidity window η_w, the BF becomes

$$B(\delta\eta|\eta_{\rm w}) = \frac{1}{2}\left[\frac{n_{+-}(\delta\eta,\eta_{\rm w}) - n_{++}(\delta\eta,\eta_{\rm w})}{< n_{+}(\eta_{\rm w}) >} + \frac{n_{-+}(\delta\eta,\eta_{\rm w}) - n_{--}(\delta\eta,\eta_{\rm w})}{< n_{-}(\eta_{\rm w}) >}\right] \tag{2.9}$$

where $n_{+}(\eta_{\rm w})$ and $n_{-}(\eta_{\rm w})$ are respectively the number of measured positively and negatively charged particles. $n_{+-}(\delta\eta,\eta_{\rm w})$ is the number of pairs of particles with opposite charges separated by pseudorapidity $\delta\eta$.

The widths of balance function is defined as:

$$< \delta\eta >= \frac{\sum_i B_s(\delta\eta_i)\delta\eta_i}{\sum_i B_s(\delta\eta_i)} \tag{2.10}$$

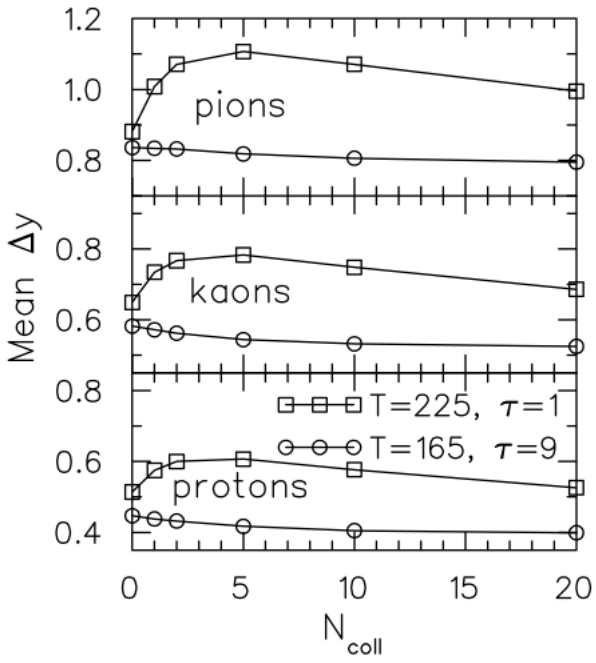

Figure 2.12: The mean width of BF is shown as a function of the number of collisions for the case where particles are created early ($\tau = 1$ fm/c, $T = 255$ MeV) and late ($\tau = 9$ fm/c, $T = 165$ MeV). The figure is from [Bas00b].

Due to local charge conservation, when particles and their antiparticles are pair produced, they are correlated initially in coordinate space. If hadronization occurs early, the members of a charge/anticharge pair would be expected to separate in rapidity due to expansion and rescattering in the strongly interacting medium. Alternatively, delayed hadronization would lead to a stronger correlation in rapidity between the particles of charge/anticharge pairs in the final state. To Measure this correlation, the uncorrelated charge/anticharge pairs need to be subtracted on an event-by-event basis as shown in the Eq. 2.9. The remaining charge/anticharge particle pairs are examined to determine the correlation as a function of the relative rapidity, Δy, between the members of the pairs. Figure 2.12 shows the widths of BF for the case where particles are created early (squares) and late (circles). It is clear that the BF is narrower for a scenario with delayed

hadronization, and is therefore sensitive to the conjecture that a quark-gluon plasma may be produced.

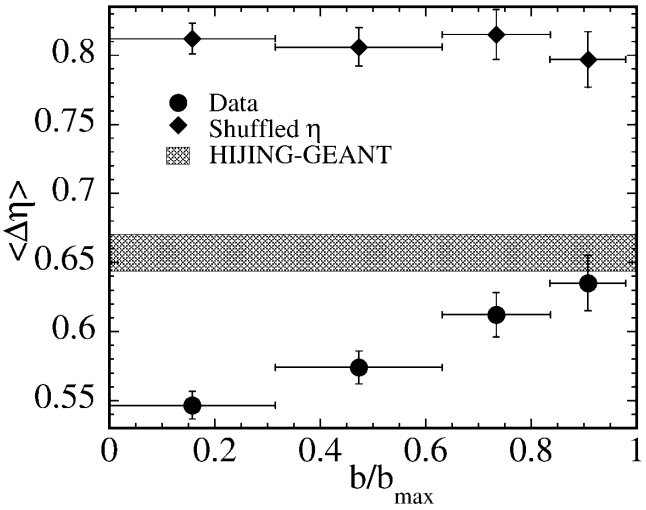

Figure 2.13: The width of balance function for charged particles, $< \Delta\eta >$, as a function of normalized impact parameter ($b/b_{\rm max}$). Error bars shown are statistical. The result from HIJING events is shown as a band and the widths from the shuffled pseudorapidity events are also plotted for comparison.

The widths of BF was studied in Au + Au collisions at $\sqrt{s_{NN}}$ =200 GeV from STAR experiment [Ada03c]. Figure 2.13 shows the widths of balance function as a function of the impact parameter fraction $b/b_{\rm max}$. From the plot we can see that the width of the balance function measured in central collisions, where QGP is more possible to be produced, is significantly smaller than that in peripheral collisions. The results for the mid-peripheral and mid-central centrality classes decrease smoothly and monotonically from the peripheral collision value. It indicates that since the width observed in peripheral collisions is consistent with the HIJING prediction, a variation in the underlying particle production dynamics between these two classes of events.

The similar dependence has also been observed in different colliding system at low energy by in NA49 experiment [Alt05a]. Figure 2.14 shows that the widths of balance function as a function of wounded nucleons for p + p, C + C, Si + Si and Pb + Pb collisions at $\sqrt{s_{NN}}$ =17.2 GeV. Data shows the narrowing trend, while the HJING model failed to described data.

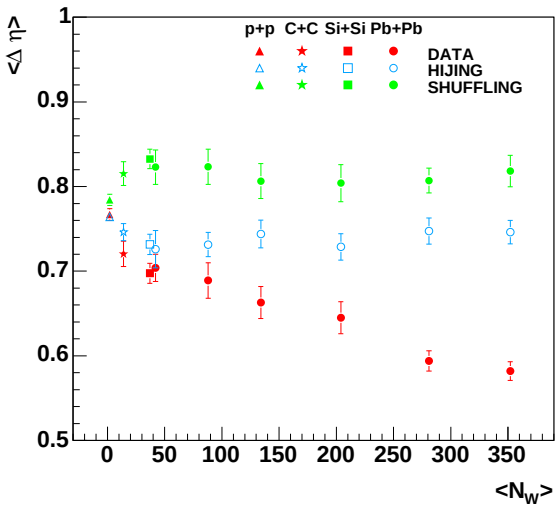

Figure 2.14: The width of balance function is shown as a function of the number of wounded nucleons for $p+p$, $C+C$, Si + Si and Pb + Pb collisions at $\sqrt{s_{NN}}$ =17.2 GeV. The figure is taken from the NA49 paper [Alt05a].

Since both STAR and NA49 experiments cover limited acceptance, it is important to study the acceptance effect on the width of balance function. In Ref. [Bas00b], based on the assumption of longitudinal boost invariance, a relation between the balance function in a rapidity window $B(\delta y|Y_{\rm w})$ and in the full rapidity range $B(\delta y|Y=\infty)$ is supposed as follow,

$$B(\delta y|Y_{\rm w}) = B(\delta y|\infty)(1-\delta y) \tag{2.11}$$

where $Y_{\rm w}$ is the size of the rapidity window.

The charge balance function is a differential combination of all possible charge correlations, and its integral over rapidity space is related to measures of charge fluctuation [Jeo02a]. The charge fluctuation $D(Q)$ is defined as

$$D(Q) = \frac{4\langle(Q-\langle Q\rangle)^2\rangle}{\langle N_{\rm ch}\rangle} \tag{2.12}$$

where $Q = n_+ - n_-$ and $n_{\rm ch} = n_+ + n_-$. The charge fluctuation is approximately related to the BF by

$$\frac{D(Q)}{4} = 1 - \int_0^{Y_{\rm w}} B(\delta y|Y_{\rm w}){\rm d}\delta y + \mathcal{O}\left(\frac{\langle Q\rangle}{\langle n_{\rm ch}\rangle}\right), \tag{2.13}$$

2.2 Models

In this section we give a brief description of theory and phenomenological models used in comparison with the measurements.

Hydrodynamics

Hydrodynamics is a macroscopic approach to study the dynamical evolution of heavy ion collisions. In the model, the central assumption is that the strong interactions happen among the matter constituents, and shortly after that, the system reaches local thermalization. Only when the system is close to local thermal equilibrium, the hydrodynamic properties, i.e., its pressure, entropy density and temperature, are well defined. Only under these conditions, the equation of state of strongly interacting matter at high temperatures can be estimated.

At relativistic heavy ion collisions, the approximate longitudinal boost invariant boundary conditions in central phase space simplify hydrodynamic equations greatly [Bjo83a]. Based on the local conservation law for energy, momentum and other conserved currents (e.g., baryon number):

$$\begin{aligned} \partial_\mu T^{\mu\nu}(x) &= 0 \\ \partial_\mu j^\mu(x) &= 0, \end{aligned} \tag{2.14}$$

the ideal fluid decompositions can be written as [Kol00a]

$$T^{\mu\nu}(x) = (e(x) + p(x))u^\mu(x)u^\nu(x) - g^{\mu\nu}p(x) \tag{2.15}$$

$$j^\mu(x) = n(x)u^\mu(x). \tag{2.16}$$

where $e(x)$ is the energy density, $p(x)$ the pressure and $n(x)$ the conserved number density at point $x^\mu = (t, x, y, z)$; $u^\mu(x) = \gamma(1, v_x, v_y, v_z)$ with $\gamma = 1/\sqrt{1 - v_x^2 - v_y^2 - v_z^2}$ is the local four velocity of the fluid. The great advantage of hydrodynamics is that it provides a covariant dynamics only depending on the equation of state (EOS) which is directly related to the lattice QCD calculations. While the disadvantage of hydrodynamics is that it can not describe the initial condition and the final freeze-out hypersurfaces, and all of these need to be modified by other models/assumptions.

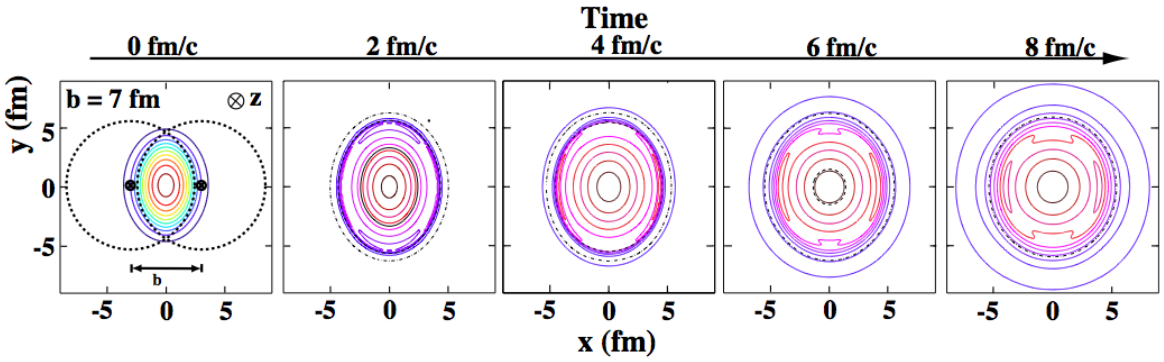

Figure 2.15: The time evolution of initial transverse energy density in coordinate space for non-central heavy ion collisions.

A phase transition from the QGP phase to a hadron gas causes a softening of the EOS: as the temperature crosses the critical temperature, the energy and entropy densities increase rapidly while the pressure rises slowly. The derivative of pressure to energy density has a minimum at the end of the mixed phase, known as the softest point. The diminishing driving force slow down the build-up of flow. Figure 2.15 shows the contours of constant energy density in initial condition and times 2, 4, 6 and 8 fm/c after thermalization. The azimuthal anisotropy is introduced through the spatial deformation of the nuclear overlap zone at non-central collisions (see Fig.2.3). The system, which is driven by its internal pressure gradients, expands more strongly in its short direction (i.e. into the direction of the impact parameter) than perpendicular to the reaction plane where the pressure gradient is smaller. It is clear that the anisotropy becomes less and less as system evolves.

Transport models

There are several transport Monte Carlo models trying to study the process of heavy ion collisions. The goals of those hadronic transport models, such as the Hadron-String Dynamics (HSD), Relativistic Quantum Molecular Dynamics (RQMD) and Ultrarelativistic Quantum Molecular Dynamics model (uRQMD) are to gain understanding of physical phenomena, i.e., creation of dense hadronic matter at high temperatures, properties of

nuclear matter, creation and transport of rare particles in hadronic matter, *etc.*

Among them, a multiphase transport (AMPT) model is a model with both partonic phase and hadronic phase [Lin05a]. There are four main components in the model: the initial conditions, partonic interactions, conversion from the partonic to the hadronic matter, and hadronic interactions. The initial conditions, which include the spatial and momentum distributions of mini-jet partons and soft string excitations, are obtained from the heavy ion jet interaction generator (HIJING) model. Zhang's parton cascade (ZPC) is then used to describe scatterings among partons. There are two versions of AMPT model: the default AMPT model (version 1.11) which has a hadronization process based on the Lund string fragmentation model and the AMPT model with string melting (version 2.11) which uses a quark coalescence model instead. In the AMPT model with string melting, hadrons, which would have been produced from string fragmentation, are converted instead to their valence quarks and antiquarks. Scatterings among the resulting hadrons are described by a relativistic transport (ART) model. It is found that the default AMPT model gives a reasonable description of rapidity distributions and transverse momentum spectra, while the AMPT model with string melting describes both the magnitude of the elliptic flow at mid-rapidity and the pion correlation function with a parton cross section of about 6 mb.

PYTHIA

PYTHIA [Ben87a] is a model for the generation of high-energy physics events, i.e. for the description of collisions at high energies between elementary particles such as $e^{\pm}$ and p ($\bar{p}$) in various combinations. It contains theory and models for a number of physics aspects, including hard and soft interactions, parton distributions, initial- and final-state parton showers, multiple interactions, fragmentation and decay.

CHAPTER 3

Experimental Set-up

The analysis of heavy ion collisions described in this thesis is performed on data taken with the STAR experiment at Relativistic Heavy-Ion Collider (RHIC). In this chapter, we introduce the experimental setup, the track reconstruction, the trigger configuration, the centrality definition and the particle identification.

3.1 RHIC

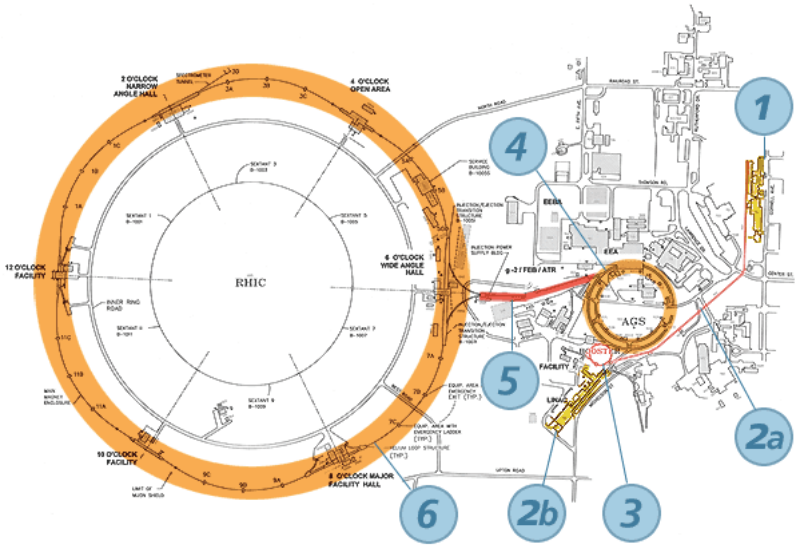

Figure 3.1: RHIC complex.

The Relativistic Heavy-Ion Collider (RHIC) locating at Brookhaven National Laboratory (BNL) in New York is the first collider in the world capable of colliding heavy ions [RHIC]. It is constructed to investigate the strongly interacting matter and search for QGP which is expected to be created in heavy ion collisions [Hah03b]. In a collision,

the center-of-mass energy can be up to 200 GeV per nucleon pair, and this is about a factor of ten larger than the highest energies reached at previous fixed target experiments. Also, as high as 500 GeV center-of-mass energy can be reached for polarized proton-proton collisions in order to study spin physics.

The Relativistic Heavy Ion Collider complex is consisted of a group of accelerators which are constructed for different physics aims as shown in Figure 3.1. To remove some of their electrons using static electricity, atoms are accelerated firstly to 15 MeV per nucleon in the Tandem Van de Graaff accelerator. Then the ions are sent towards the circular Booster (3) through a transfer line (2a). The Booster synchrotron accelerates the ions to 95 MeV per nucleon and then feeds the beam into the Alternating Gradient Synchrotron (AGS) where the ions are accelerated to 10.8 GeV per nucleon. Finally the ions injected to the beams via another AGS-to-RHIC Line (5) into the two rings of RHIC (6), and accelerated to the colliding energy 100 GeV per nucleon.

There are six intersection points in RHIC's 3.8 kilometer ring. Two rings of accelerating magnets cross at those points, and the particle beams to collide there. Four of the intersections occupied by experiments: BRAHMS collaboration located at 2 o'clock position, STAR collaboration located at 6 o'clock position, PHENIX collaboration located at 8 o'clock position and PHOBOS collaboration located at 10 o'clock position.

3.2 The STAR Experiment

STAR experiment was constructed to investigate the behavior of strongly interacting matter at high temperature and density, and also to search for signatures of QGP formation. Its large acceptance makes it particularly suited for event-by-event characterization of heavy ion collisions and also for the detection of hadron jets [Har03a].

The perspective view of the STAR detector is shown in Figure 3.2, and a cutaway side view is displayed in Figure 3.3 as configured for the RHIC 2004 run. The STAR detector consists of several subsystems, and they integrate to the whole functionality of the detector. The Time Projection Chamber (TPC) [Tho02a] is the primary tracking

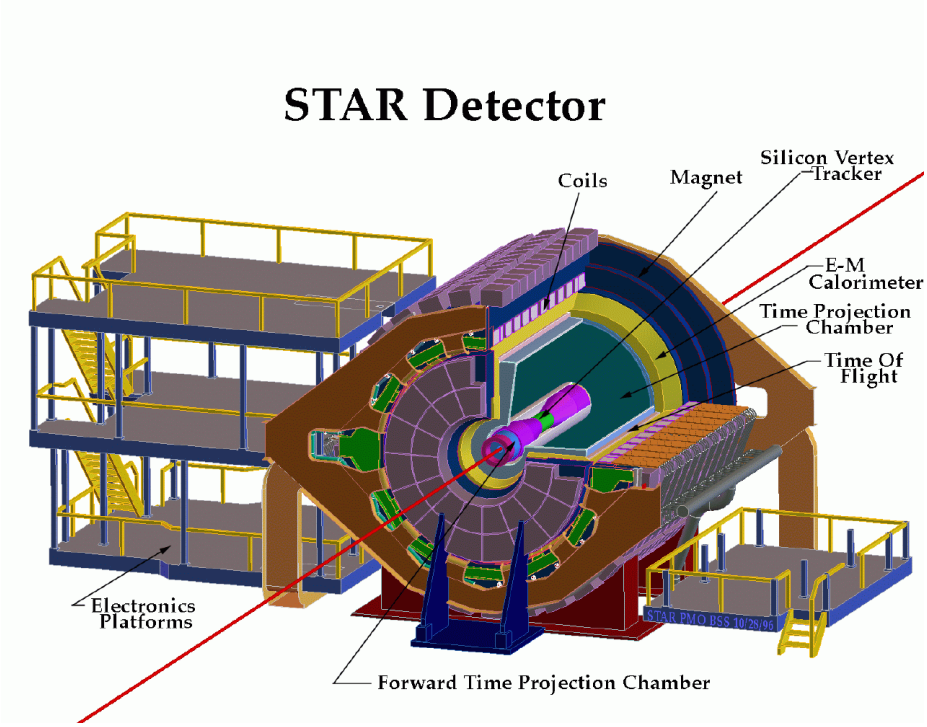

Figure 3.2: Perspective view of the STAR detector. Figure is taken from [Har03a].

device of STAR. A Barrel Electromagnetic Calorimeters (BEMC) [Bed03a] and an End-cap Electromagnetic calorimeter (EEMC) [All03a] are used to measure the transverse energy deposited by electrons and photons. The BEMC and EEMC are also used for triggering on events with high transverse energy or rare processes. Two cylindrical Forward Time Projection Chamber detectors (FTPCs) were constructed to extend the phase space coverage to the region $2.5 < |\eta| < 4.0$. Two Zero-Degree Calorimeters (ZDCs), two Beam Beam Counters (BBCs) and a Central Trigger Barrel (CTB) are used for event triggering. The Time-of-Flight (TOF) detector [Bon03a] which measures the flying time of charged particles in TPC, can significantly improve the particle identification (PID) capability of TPC. The Silicon Vertex Tracker (SVT) [Bel03a] was added to enhance physics capabilities of TPC. It can be used to improve the primary vertexing, e.g., the two track separation resolution and the energy loss measurement for particle identification. The Silicon Strip Detector (SSD) [Arn03a] constitutes the fourth layer of the inner tracking system. Installed between the SVT and the TPC, the SSD enhances the tracking capabilities of the STAR experiment by measuring accurately the two dimensional

hit position and energy loss of the charged particles.

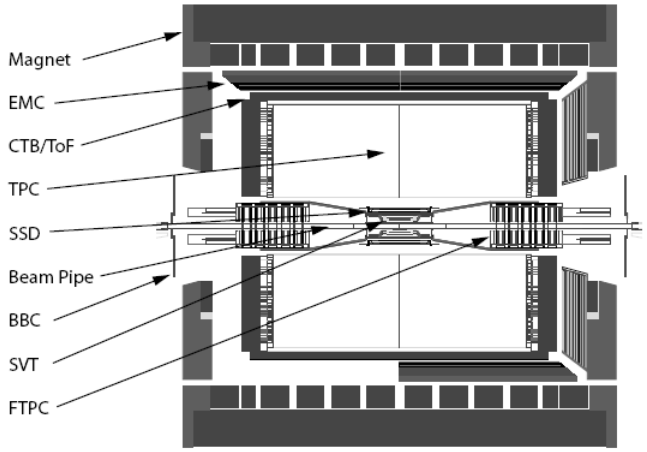

Figure 3.3: Cutaway side view of the STAR detector as configured in 2004.

3.2.1 STAR TPC

The Time Projection Chamber (TPC) is STAR's primary tracking device [And03a]. It records the tracks of particles, and measures their momenta. Its covers ± 1.8 units of pseudorapidity and full 2π azimuthal angle. Particles are identified over a momentum range from 100 MeV/c to greater than 1 GeV/c by measuring their ionization energy loss (dE/dx). Their momenta are measured over a range of 100 MeV/c to 30 GeV/c.

The STAR TPC is shown in Fig. 3.4. The diameter of TPC is 4 m and it's 4.2 m long. It sits in a large solenoidal magnet [Ber03a] which has an maximum magnitude field strength of 0.5 Tesla. It is an empty volume of gas in a uniform electric field of about 135 V/cm. At the center of the TPC is the high-voltage Central Membrane (CM) and at both end-caps are Multi-Wire Proportional Chambers (MWPC). When passing through the volume, charged particles are detected in drift chambers as they ionize the gas, and the corresponding electrons created from track ionization will drift in the longitudinal direction to the readout end-cap of the chamber along the TPC electric field lines.

The readout system locating on the ends of the TPC is based on Multi Wire Proportional Counter (MWPC) with readout pads. The readout MWPC is consisted of 3 wire

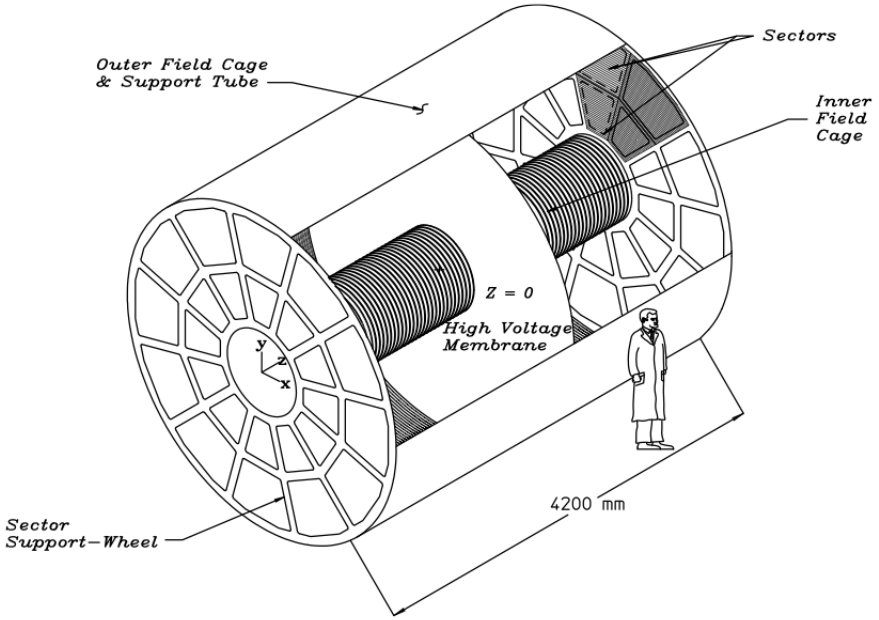

Figure 3.4: Perspective view of the STAR TPC.

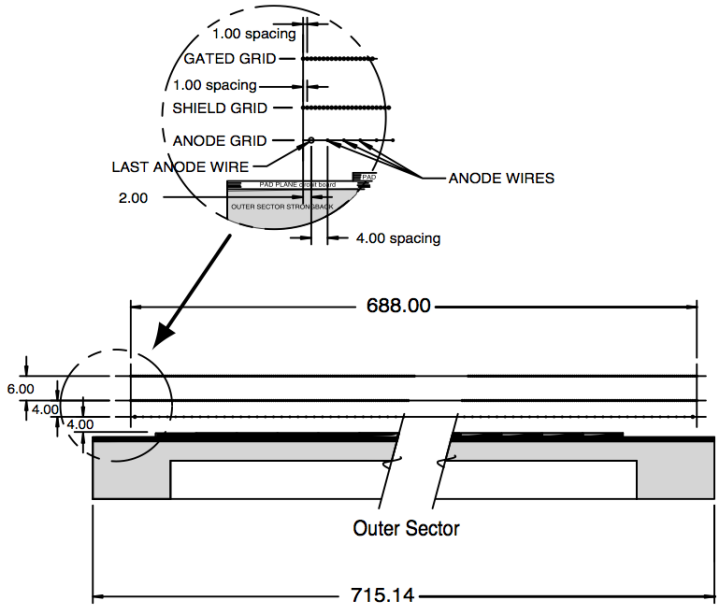

Figure 3.5: A cut-away view of an outer subsector pad plane. All dimensions are in millimeters. The figure is from [And03a].

planes: a gating grid, ground plane, and anode wires. The gating grid is the outermost wire plane. It separates the drift region from the amplification region, and controls the entry of electrons from the TPC drift volume into the MWPC. When a trigger is received, the drift electrons are allowed to pass through and the event is recorded. Electrons initiate avalanches when they pass the gating grid and drift to the anode wires. The ground grid terminates the field in the avalanche region as well as calibrate the pad electronics. The anode wires provide the necessary electric field to avalanche the electrons from the track ionization. The signal measured on the pads will be amplified, integrated and digitalized by the front-end electronics. The position of the ionizing particle along the drift direction (z coordinate) is reconstructed by the time bucket and the drift velocity. Figure 3.5 shows a cutaway view of the readout pad planes of an outer sector.

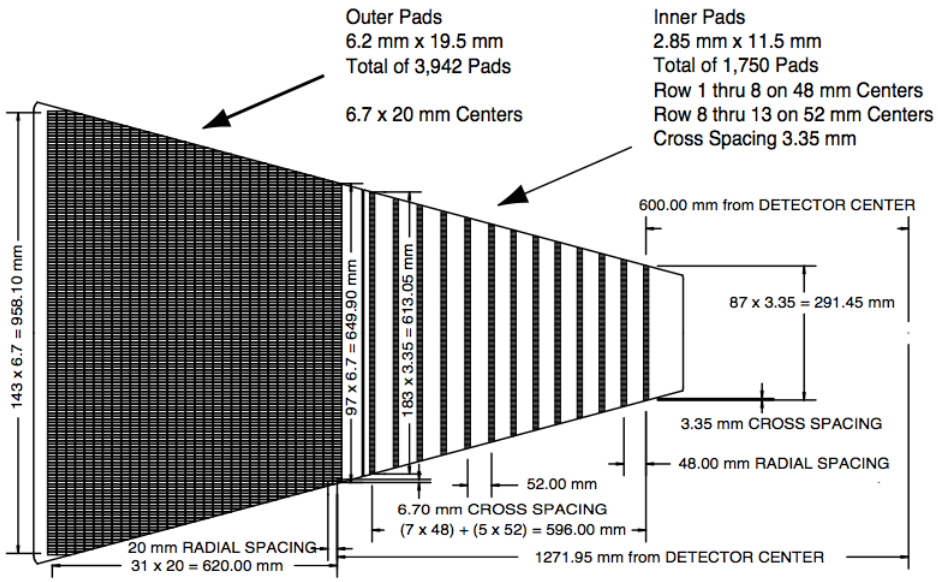

Figure 3.6: The anode pad plane with one full sector shown. The inner subsector is on the right and outer subsector is on the left. The figure is from [And03a].

The TPC is consisted of 24 super sectors, and each subsequently divided into an inner and outer sector. The anode pad plane with one full sector is shown in Figure 3.6. The inner sector are grouped into 13 pad rows, with a total of 1750 small pads (2.85 mm $\times$11.5 mm). The outer sector are grouped into 32 pad rows, with a total of 3940 smaller pads (6.20 mm $\times$19.5 mm).

3.2.2 STAR FTPCs

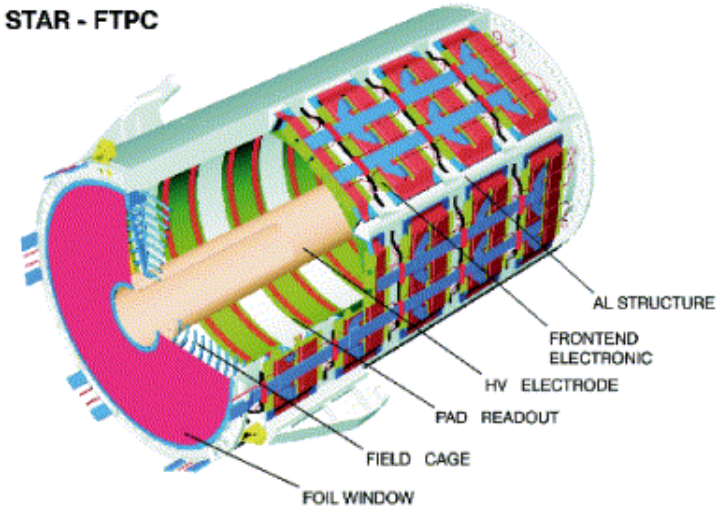

Figure 3.7: Schematic diagram of an FTPC.

The Forward Time Projection Chambers (FTPC) were built to extend the acceptance in forward region for the STAR experiment [Ack03b]. They cover the pseudorapidity range of $2.5 < |\eta| < 4.0$ on both sides. FTPCs measure momenta and production rates of particles. Meanwhile, the event-by-event measurements like $\langle p_T \rangle$, fluctuations of charged particle multiplicity and collective flow anisotropy can be studied due to the high multiplicity (approximately 1000 charged particles in a central Au + Au collision). The increased acceptance improves the general event characterization in STAR and the capability of studying the asymmetric systems.

Figure 3.7 shows the schematic diagram of one FTPC. It is 75 cm in diameter and 120 cm long with a cylindrical structure. Its radial drift field and readout chambers located in five rings on the outer cylinder surface. Each ring is consisted of two pad rows and subdivided azimuthally into six readout chambers. In the region close to the beam pipe, the radial drift configuration was chosen to improve the two track separation due to the highest particle density. The field region which is formed by the inner HV-electrode and the outer cylinder wall at ground potential, is closed by a planar structure of concentric rings at both ends. The front end electronics (FEE) mounted on the back of the readout chambers are used to amplify, shape, and digitize the signals.

CHAPTER 4

Analysis Method

In this chapter, we discussed the dataset and the cuts used for analysis. The particle identification for charged particles $\pi^{\pm}$, p ($\bar{p}$) and the reconstructed particles K^0_S, Λ ($\bar{\Lambda}$) are also presented. Event plane method and cumulant method have been developed to accurately measure the anisotropic flow.

4.1 Event and track selection

The STAR experiment collects about 25 million and 60 million minimum bias events during RHIC Run IV and VII for Au + Au collisions at $\sqrt{s_{NN}}$ = 200 GeV, separately. The trigger and event selection are summarized in Table 4.2. Events which are chosen for our analysis are listed in the most right column.

Trigger Setup Name	Production	Vertex Cut	Trigger ID	Events No.
productionMinBias	P05ic	$\|V_z\| < 30$ cm	15007	13.4 M
productionMinBias	P05ic	$-10 < V_z < 50$cm	15003	6.2 M
productionLowMidHigh	P05ic	$\|V_z\| < 30$cm	15007	6.3 M

Table 4.1: Run IV trigger and events selection for minimum bias in Au + Au collisions at $\sqrt{s_{NN}}$ = 200 GeV.

There are two kind of reconstructed tracks. One is called the global track, the other is called the primary track. After fitting all the hit points in TPC by helix, the global tracks are reconstructed. When all of the global tracks from one event are reconstructed, we can extrapolate tracks back to the origin and get the collision vertex. The primary

Trigger Setup Name	Production	Vertex Cut	Trigger ID	Events No.
2007ProductionMinBias	P08ic	$\|V_z\| < 30$ cm	200001, 200003	50 M
2007Production2	P08ic	$\|V_z\| < 30$ cm	200013	10 M

Table 4.2: Run VII trigger and events selection for minimum bias in Au + Au collisions at $\sqrt{s_{NN}} = 200$ GeV.

track is defined by the helix fit to the TPC points along with the vertex.

The centrality is defined by the TPC reference multiplicity. The TPC reference multiplicity is the number of the primary tracks in the TPC whose fitting points are 15 or more in the pseudo-rapidity range -0.5 to 0.5 and a distance of closet approach (DCA) to the primary vertex less than 3 cm. To reject the non-hadronic events, some low multiplicity events are rejected due to a lower cut on CTB. The total number of events are also corrected by the Glauber model. Finally, the nine centrality bins and the corresponding geometric cross section are listed in Table 4.3.

Centrality Bin	Reference Multiplicity	Geometric Cross Section
1	14-31	70%-80%
2	31-57	60%-70%
3	57-96	50%-60%
4	96-150	40%-50%
5	150-222	30%-40%
6	222-319	20%-30%
7	319-441	10%-20%
8	441-520	5%-10%
9	$\geq$520	0%-5%

Table 4.3: Run IV centrality bins in Au + Au collisions at $\sqrt{s_{NN}} = 200$ GeV.

Figure 4.1 shows charged particle multiplicity distribution without the Glauber correction. In the analysis, we use the mini-bias data which is centrality $0-80\%$. Sometimes we need to use wide centrality bins to get better statistic, thus the three combined centrality bins, $0-10\%$ (central), $10\%-40\%$ (mid-central) and $40\%-80\%$ (peripheral) are

used as indicated in the Fig. 4.1.

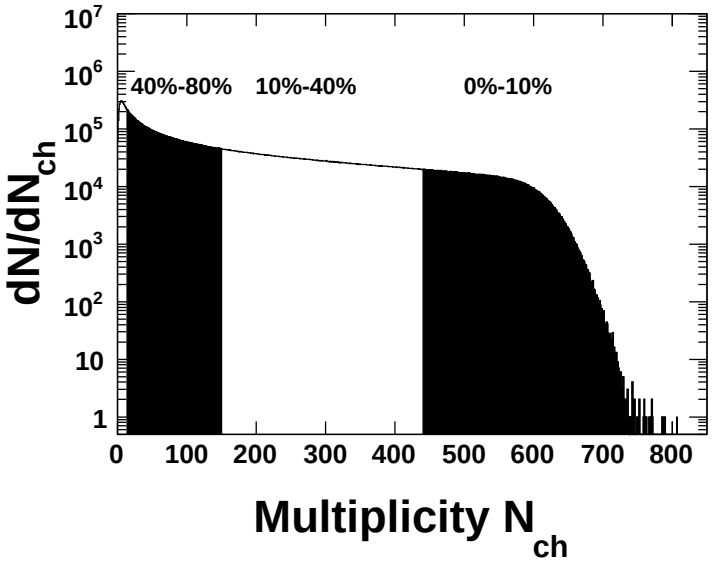

Figure 4.1: The TPC reference multiplicity distribution in Au + Au collisions at $\sqrt{s_{NN}}$ = 200 GeV of Run IV.

The inclusion of inner tracking for the Run VII Au + Au 200 GeV data rendered reference multiplicity a poor method to determine centrality. It's shown there is a dependence on the primary vertex position for the reconstruction efficiency in the $|V_z| < 30$ cm region. The dependence was generally absent for TPC only tracking used in many of the previous productions, and is undesirable since it requires the centrality cuts to change as a function of V_z. To this end, another variable was proposed called global reference multiplicity is used for centrality definition.

Global reference multiplicity is the number of global tracks in the TPC with the 10 or more fit points having the pseudo-rapidity from -0.5 to 0.5 and a distance of closet approach (DCA) to the primary vertex less than 3 cm. The nine centrality bins and the corresponding geometric cross section for Au + Au collisions are listed in Table 4.4 .

The remaining issues are biases on multiplicity distribution introduced by the main online Vertex Position Detector (VPD) trigger-setup (200013). The biases come from two sources. Firstly, over the full range in V_z, the VPD is more efficient at triggering on

Centrality Bin	Global Reference Multiplicity	Geometric Cross Section
1	10-20	70%-80%
2	21-38	60%-70%
3	39-68	50%-60%
4	69-113	40%-50%
5	114-177	30%-40%
6	178-268	20%-30%
7	269-398	10%-20%
8	399-484	5%-10%
9	$\geq$485	0%-5%

Table 4.4: Run VII centrality bins in Au + Au collisions at $\sqrt{s_{NN}} = 200$ GeV.

central events relative to peripheral. This leads to a general deficit in peripheral events for a given data sample. The second comes from a centrality dependence of the VPD's online V_z resolution which is worse for peripheral events relative to central. Since the trigger-setup (200013) insisted events events fall within the inner tracking acceptance, i.e., with an online cut of $|V_z| < 5$ centimeter, the resolution issue means that events at the higher $|V_z|$ are more likely to be peripheral whereas the events at lower $|V_z|$ are more likely to be central.

The V_z dependent biases in multiplicity distribution require a re-weighting correction to be applied for all analysis. For any analysis with a "signal" summed up over a range of global reference multiplicity, events at $|V_z| \sim 0$ will have their peripheral contribution scaled up in order to restore the unbiased case via the correction. The opposite will be true for events at higher $|V_z|$ where the peripheral contribution will be scaled down - again to the restore the the unbiased case. The correction has to be applied as function of V_z in 2 centimeter bins for acceptance reasons.

In a given V_z bin, firstly the weights have to be determined. This is done by normalizing the global reference multiplicity distribution by the number of events with global reference multiplicity larger than 500. The MC Glauber histogram then has be divided by the normalized global reference multiplicity distribution to calculate the weights. Fi-

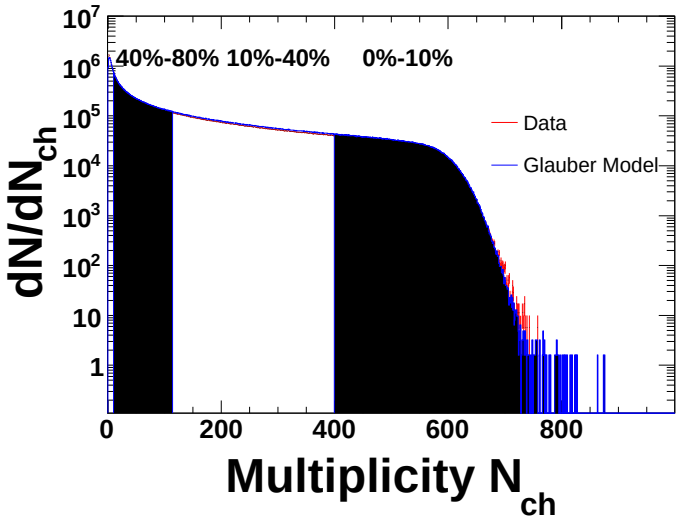

Figure 4.2: The TPC global reference multiplicity distribution in Au + Au collisions at $\sqrt{s_{NN}}$ = 200 GeV of Run VII.

nally in each event, we multiply the event quantities by its weight which is obtained according to V_z and global reference multiplicity in this event. Figure 4.2 shows global reference multiplicity distribution after the correction and the comparison with Glauber Monte-Carlo calculation.

4.2 Particle Identification

Charge particles passing through the TPC will lose energy via ionization. The charge collected for each hit on a track is proportional to the energy loss of the particle. For a particle with charge Z (in units of e) and speed $\beta = v/c$ transversing a medium with density ρ, the mean energy loss is described by the Bethe-Bloch formula

$$\langle \frac{dE}{dx} \rangle = 2\pi N_0 r_e^2 m_e c^2 \rho \frac{Z z^2}{A\rho^2} [\ln \frac{2m_e\gamma^2 v^2 E_M}{I^2} - 2\gamma^2], \tag{4.1}$$

where N_0 is Avogadro's number, m_e is the mass of electron, $r_e(= e^2/m_e)$ is the classical electron radius, c is the speed of light, z is the atomic number of the absorbing material, A is the atomic weight of the absorbing material, $\gamma = 1/\sqrt{(1-\beta^2)}$, I is the mean excitation energy, and $E_M(= 2m_e c^2\beta^2/(1-\beta^2))$ is the maximum transferable energy in

a single collision.

From the equation, it's clear that different particle species with the same momentum p lose different energy, thus we can identify charge particles by their specific energy loss in TPC. Fig. 4.3 shows the energy loss for particles in the TPC as a function of momentum.

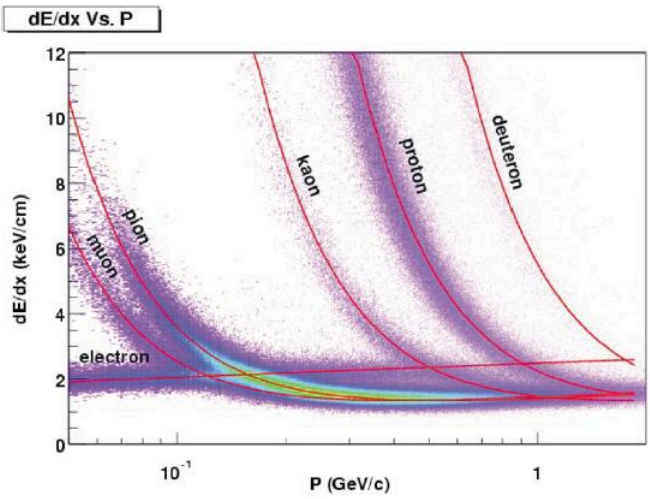

Figure 4.3: The energy loss distribution as a function of p_T in TPC.

In order to quantitatively describe the particle identification, a variable is defined (in the case of charged pion identification) as

$$n\sigma_\pi = \ln[\frac{dE}{dx}_{meas} - \langle\frac{dE}{dx}\rangle_\pi]/\sigma_{dE/dx}, \tag{4.2}$$

in which $\frac{dE}{dx}_{meas}$ is the measured energy loss of a track and $\langle\frac{dE}{dx}\rangle_\pi$ is the expected mean energy loss for charged pion. $\sigma_{dE/dx}$ denotes the resolution of specific ionization in the TPC. For the identification of charged kaon, proton and anti-proton, a similar definition can be given by $n\sigma_K$, $n\sigma_p$ and $n\sigma_{\bar{p}}$. The different particle species can be selected by applying the cuts on the variables.

The typical resolution of dE/dx for long tracks (nHit $\sim$ 40) at midrapidity inside TPC in Au + Au collisions is $\sim$ 8%, which allows for the π/K separation up to $p \sim 0.7$ GeV/c and p/π separation up to $p \sim 1.1$ GeV/c.

In high momentum region ($p_T > 2.5$ GeV/c), we can extend the pion and (anti)proton identification. This method is based on the clear separation of the mean dE/dx for

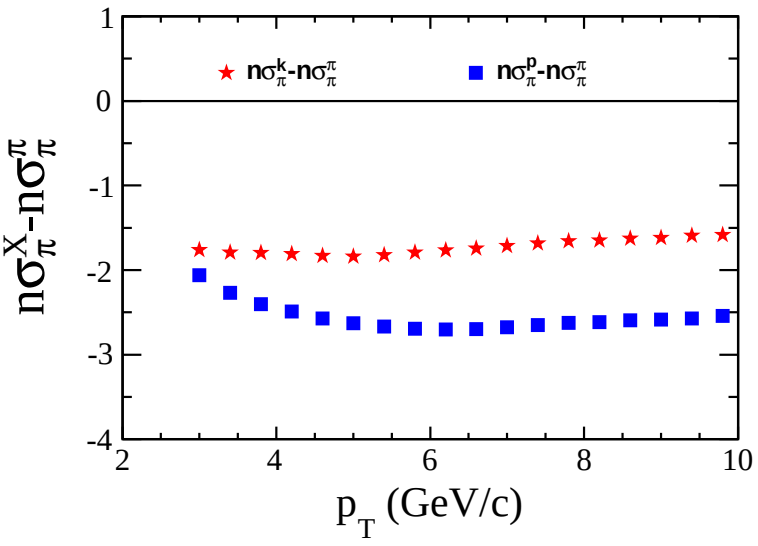

Figure 4.4: The relative dE/dx peak positions of $n\sigma_\pi^p$ and $n\sigma_\pi^K$ as a function of p_T.

different particles in the relativistic rise region of dE/dx as shown in Fig. 4.4. The differences of dE/dx between pion and other charged particles ($n\sigma_\pi^p$ and $n\sigma_\pi^K$) are shown in Fig. 4.4. The kaon band is about 1.8σ away from the pion band with little p_T dependence in $p_T > 2.5$ GeV/c region, while the proton band is about 2σ away from the pion band and leaver further in $3 < p_T < 5$ GeV/c region.

Pions and protons are identified with a cut of $n\sigma_\pi > 0$ and $n\sigma_p < 0$ respectively. The corresponding purities are 95% for pion and 67% fro proton, respectively. The purity of proton increase since the proton band separates further from the kaon band and pion band as p_T increases. The contamination to pion will decrease pions v_2 by less than 1% for the high purity of pions. The contamination to proton s arise from kaon (28%) and pions (5%) using at $3.0 < p_T < 3.5$ GeV/c region. Figure 4.5 shows an example of $n\sigma_p$ distribution with 3-Gaussian fit.

This method is confirmed by the STAR TOF measurements.

4.3 K_S^0 and Λ Reconstruction

The strange particles K_S^0 and Λ are reconstructed through their weak decay channel, and the properties are summarized in Table 4.5.

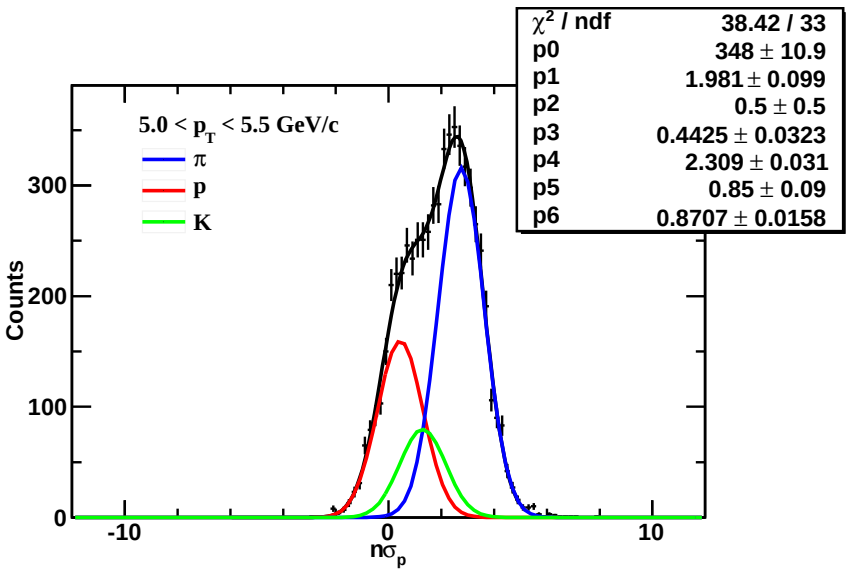

Figure 4.5: $n\sigma_p$ distribution at $5.0 < p_T < 5.5$ GeV/c. The black curve is the 3-Gaussian fit.

Particle Type	Decay Channel	Branching Ratio (%)	$c\tau$ (cm)	Mass (GeV/c^2)
K^0_S	$\pi^+ + \pi^-$	68.95 ± 0.14	2.68	0.497
Λ ($\bar{\Lambda}$)	$p + \pi^-$ ($\bar{p} + \pi^+$)	63.9 ± 0.5	7.89	1.115

Table 4.5: K^0_S and Λ ($\bar{\Lambda}$) weak decay properties

The identification of K^0_S and Λ is based on statistics-wise invariant mass distribution. The charged $\pi^{\pm}$ and p ($\bar{p}$) tracks are identified by their energy loss (dE/dx), and their momentums are measured from the helix in TPC. The invariant mass of all possible positive and negative charged particles pairs are then calculated.

The candidates include both signal and background. The experimental issues, e.g., the misidentification of daughter tracks, the decay vertex close to the primary vertex or daughter tracks of a pair coming from different candidates, may cause the combinatorial background. Some of the fake decay vertexes can be rejected according to the decay geometry. The decay topology is shown in Figure 4.6. The decay lengths ($c\tau$) of K^0_S and Λ are 2.68 and 7.89 centimeter separately, and most of them will decay within the TPC of 2 meter radius. In the laboratory frame, the decay vertex and primary vertex are well identified since decay vertex is a few centimeters further than primary vertex with several hundreds microns. The $V0$ is named after the "V" topology with the "0" net charge. The distance of closet approach (dca) between two daughter tracks is used to determine the point of the decay vertex. The dca1 (dca2) is the dca of the daughters to the primary vertex, and they are larger than the contributions from primary tracks. b is the dca from the primary vertex to the direction of $V0$ momentum, and it is equal to zero in the ideal case. rv is the traveling distance of $V0$ (decay length).

p_T (GeV/c)	< 0.8	0.8-3.6	> 3.6
π dca to primary vertex (cm)	> 1.5	> 1.0	> 0.5
dca between daughters (cm)	< 0.7	< 0.75	< 0.5
dca from primary vertex to V0	< 0.7	< 0.75	< 0.5
decay length (cm)	4-150	4-150	10-120

Table 4.6: Cuts selection criteria for K^0_S in Au + Au collisions at $\sqrt{s_{NN}} = 200$ GeV.

Table 4.6 and Table 4.7 list the $V0$ optimized cuts for K^0_S and Λ in Au + Au collisions at $\sqrt{s_{NN}} = 200$ GeV, respectively. The signal over background ratio will be significantly enhanced by using the cuts.

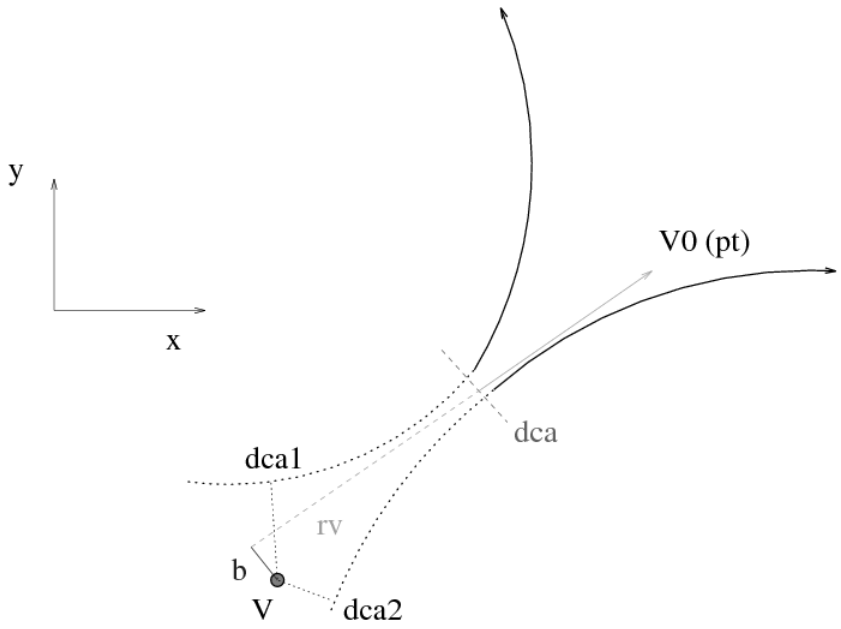

Figure 4.6: $V0$ decay topology. The figure is from [Mar98a]

p_T (GeV/c)	< 0.8	0.8-3.6	> 3.6
π dca to primary vertex (cm)	> 2.5	> 2.0	> 1.0
p dca to primary vertex (cm)	> 1.0	> 0.75	> 0
dca between daughters (cm)	< 0.7	< 0.75	< 0.4
dca from primary vertex to V0	< 0.7	< 0.75	< 0.75
decay length (cm)	4-150	4-150	10-125

Table 4.7: Cuts selection criteria for Λ in Au + Au collisions at $\sqrt{s_{NN}} = 200$ GeV.

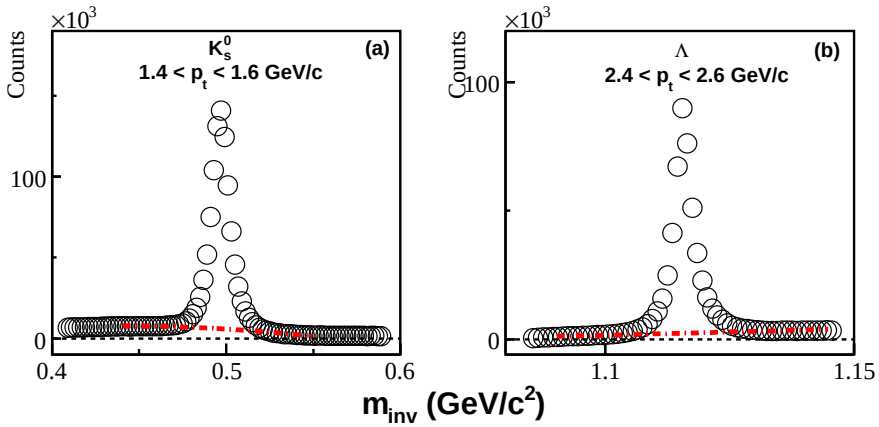

Figure 4.7: The invariant mass distributions of (a) K^0_S at $1.4 < p_T < 1.6$ GeV/c and (b) Λ at $2.4 < p_T < 2.6$ GeV/c at Au + Au collisions mini-bias (0-80%) are shown. The red dash lines are polynomial fit of the backgrounds.

For K^0_S and Λ , the remaining backgrounds are estimated by fitting the invariant mass distribution with function describing signals and backgrounds. The fitting function contains two gaussian functions plus a polynomial function. Two gaussian functions with the same mass peak parameter are used to describe the signal while a polynomial function is used to describe the background. Then the signal and background contributions which are obtained from fitting can be used to extract K^0_S and Λ signal v_2.

4.4 Standard event plane method

In this section, we introduce the method to estimate the reaction plane by using the flow signal and to calculate n^{th} harmonic coefficients.

4.4.1 Fourier expansion

In the triple differential distribution, the dependence on the particle emission azimuthal angle measured with respect to the reaction plane can be written in a form of Fourier

series

$$E\frac{d^3N}{d^3p} = \frac{1}{2\pi}\frac{d^2N}{p_T dp_T dy}(1 + \sum_{n=1}^{\infty} 2v_n \cos[n(\phi - \Psi_r)]), \tag{4.3}$$

where Ψ_r refers to the (true) reaction plane angle. The sine terms vanish due to the reflection symmetry with respect to the reaction plane. The finite multiplicity of the events can be corrected by the event plane resolution, which is the main advantage of this method. It is very important because after correction, the results for particles in a certain phase space region can be directly compared with theoretical predictions, or the simulations unfiltered for the detector acceptance.

4.4.2 Event plane determination

The Fourier coefficients in the expansion of the azimuthal distribution of particles with respect to event plane are evaluated to study the event anisotropy. The standard event plane method is proposed to study flow by reconstructing the reaction plane Ψ_r, and the estimated reaction plane is called the event plane.

Starting from the n^{th} harmonic event flow vector Q_n whose x and y components are given by

$$Q_n \cos(n\Psi_n) = X_n = \sum_i w_i \cos(n\phi_i) \tag{4.4}$$

$$Q_n \sin(n\Psi_n) = Y_n = \sum_i w_i \sin(n\phi_i) \tag{4.5}$$

The n^{th} harmonic event plane can be obtained by

$$\Psi_n = \left(\tan^{-1}\frac{\sum_i w_i \sin(n\phi_i)}{\sum_i w_i \cos(n\phi_i)}\right)/n, \tag{4.6}$$

here ϕ is the azimuthal angle of a particle. The sum goes over all the particles used in the event plane determination, and w_i is the weight to optimize the event plane resolution. Usually the weights are assigned with the transverse momentum. The choice of weights is to make the event plane resolution the best by maximizing the flow contributions to

the flow vector. The tracks selection criteria to reconstruct the event plane is listed in Table 4.8.

Flow track selection criteria	
nHits	> 15
nHits/nMax	> 0.52
dca	< 2 cm
transverse momentum	$0.1 < p_T < 2.0$ GeV/c

Table 4.8: Selection criteria for flow tracks used in the event plane reconstruction

For a given n, the corresponding Fourier coefficient v_n can be evaluated using the reaction planes determined from any harmonic m, with $n \geq m$, if n is a multiple of m. Writing the equation in terms of km instead of n, the event plane evaluated from the m^{th} harmonic the Fourier expansion is

$$\frac{d(wN)}{\phi - \Psi_m} = \frac{wN}{2\pi}(1 + \sum_{k=1}^{\infty} 2v_{km}^{\text{obs}} \cos[km(\phi - \Psi_m)]). \tag{4.7}$$

In order to remove the auto-correlation effect, when calculate the v_n of a particle of interest, the event plane will be re-calculated without this particle. This method of removing autocorrelations assumes that contributions from conservation of momentum are small.

At ultra-relativistic energies, the v_2 signal is the biggest one and the second order event plane Ψ_2 has the highest resolution. Elliptic flow and the higher order even harmonics estimated with respect to the Ψ_2 are denoted as $v_2\{\text{EP}_2\}, v_4\{\text{EP}_2\}$ etc.

4.4.3 Detector effect

The event plane angle is random in the laboratory frame, thus its distribution should be flat in the perfect detector. A straightforward detector induced bias is non-uniform azimuthal coverage which can be corrected for as long as the non-uniformities are small. Several procedures have been developed to flat the event plane angle distribution. One of most commonly used methods is to use the particle azimuthal angle itself as a measurement of the acceptance. The inverting ϕ distributions of detected tracks for a large

event sample is used as the corresponding weight, and it is called "ϕ weight". The ϕ weights are folded into the weight w_i in Equation 4.4 and 4.5.

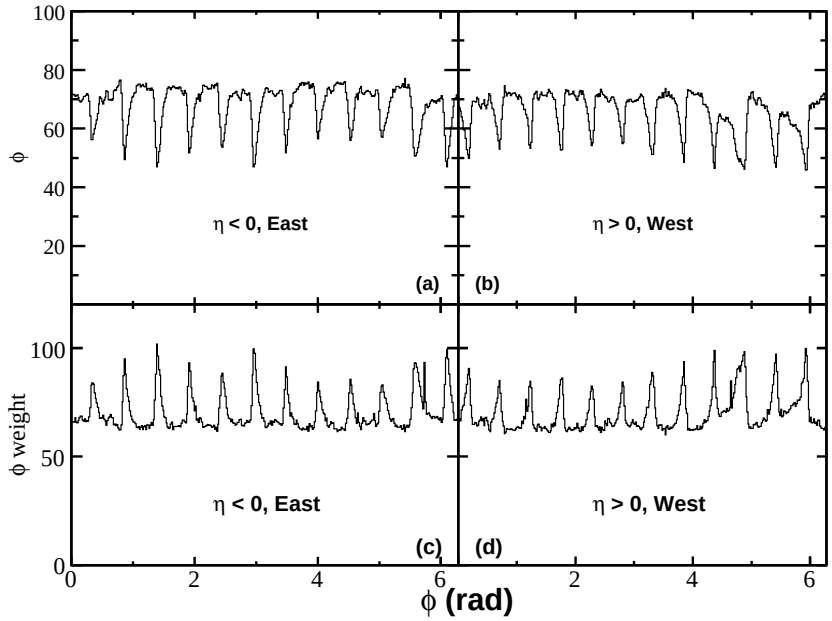

Figure 4.8: ϕ and the corresponding ϕ weight distributions in east and west TPC for $0-5\%$ centrality in Au + Au collisions at $\sqrt{s_{NN}} = 200$ GeV.

Fig. 4.8 (a) and (b) show the ϕ distribution of east TPC ($\eta < 0$) west TPC ($\eta > 0$) for $0-5\%$ centrality data in Au + Au collisions at 200 GeV. The corresponding ϕ weights are shown on Fig. 4.8 (c) and (d).

After using ϕ weight, the 2^{nd} order event plane distribution is shown in Fig. 4.9 as open circles. The black curve shows a constant fit to the event plane azimuthal distribution.

We also use both the Forward Time Projection Chambers (FTPCs) to determine an event plane for each event. The FTPCs cover pseudo-rapidity $|\eta|$ from 2.5 to 4.0. This rapidity gap helps to reduce non-flow contributions. Non-flow effects refer to the correlations that are not associated with the reaction plane. Included in non-flow effects are jets, resonance decay, short-range correlations such as the Hanbury-Brown Twis (HBT) effect, and momentum conservation.

Due to the several acceptance loss for FTPCs, ϕ weight method is not enough to

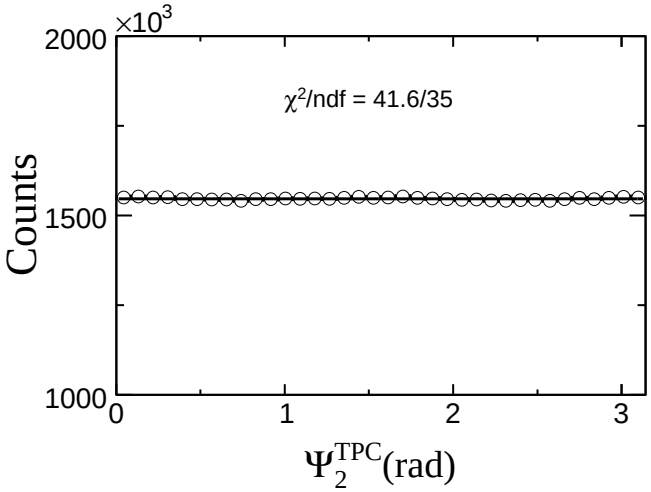

Figure 4.9: The distribution of 2nd harmonic event plane angle (Ψ_2) from TPC in Au + Au collisions at $\sqrt{s_{NN}} = 200$ GeV.

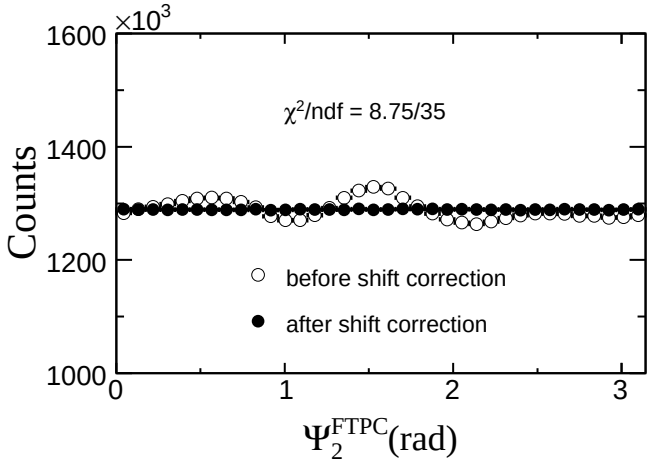

Figure 4.10: The distribution of 2nd harmonic event plane angle (Ψ_2) from FTPC in Au + Au collisions at $\sqrt{s_{NN}} = 200$ GeV. The black curve is the const fitting of the FTPC event distribution after shift correction.

generate the flat event plane distribution. Thus, the shifting method [Bar97a] is applied to force the event plane distribution to be flat. The corrected new angle is defined as

$$\Psi^{'} = \Psi + \Delta\Psi, \tag{4.8}$$

where $\Delta\Psi$ is written in the form

$$\Delta\Psi = \sum_{n}[A_n \cos(n\Psi) + B_n \sin(n\Psi)]. \tag{4.9}$$

Requiring the vanishing of the n^{th} Fourier moment of the new distribution, the coefficients A_n and B_n can be evaluated by the original distribution

$$\begin{aligned} A_n &= \frac{2}{n}\langle\cos(n\Psi)\rangle, \\ B_n &= -\frac{2}{n}\langle\sin(n\Psi)\rangle, \end{aligned} \tag{4.10}$$

$\langle\cdots\rangle$ is the average over the whole event sample

It gives the Equation 4.11 which shows the formula for the shift correction. The average in Equation 4.11 goes over a large sample of events. The higher harmonic applied, the flatter the event plane distribution is. In the analysis, the correction goes up to 20^{th} harmonic. The distributions of Ψ_2^{East} and Ψ_2^{West} are flatten separately and then the full-event plane distributions are constructed. Accordingly, the observed v_2 and resolution are calculated using the rotated (sub)event plane azimuthal angle

$$\Psi^{'} = \Psi + \sum_{n}\frac{1}{n}[-\langle\sin(2n\Psi)\rangle\cos(2n\Psi) + \langle\cos(2n\Psi)\rangle\sin(2n\Psi)]. \tag{4.11}$$

Figure 4.10 shows the second harmonic event plane azimuthal distribution after shift correction are applied in FTPC. The black curve shows a constant fit to the event plane azimuthal distribution.

As mentioned before, the finite multiplicity produces limited resolution when measuring the event plane angle, thus the coefficients in the Fourier expansion of the azimuthal distributions with respect to reaction plane must be corrected to what they would be relative to the real reaction plane

$$v_n = \frac{v_n^{\text{obs}}}{\langle\cos[km(\Psi_m - \Psi_r)]\rangle}, \tag{4.12}$$

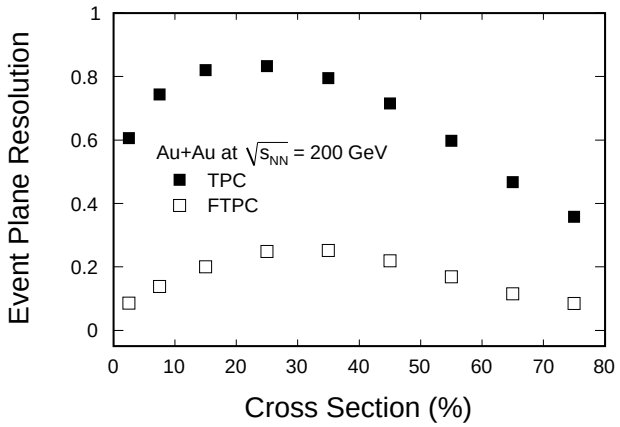

Figure 4.11: The 2nd order TPC event plane and FTPC resolution for v_2 in Au + Au collisions at $\sqrt{s_{NN}} = 200$ GeV for 9 different centrality intervals.

where v_2, $v_2^{\rm obs}$, Ψ_2 and Ψ_r refer to the real v_2, observed v_2, the event plane angle and the real reaction plane angle. $\langle\cdots\rangle$ is the average over the whole event sample. It is found that $< \cos[2(\Psi_2 - \Psi_r)] >$ is the reaction plane resolution. To calculate it, a full event is divided into two sub-events, and the event plane angles of two sub-events are calculated separately according to Equation 4.6. The event plane resolution for the sub-event is given by Equation 4.13.

$$\langle\cos[2(\Psi_2^A - \Psi_r)]\rangle = \sqrt{\langle\cos[2(\Psi_2^A - \Psi_2^B)]\rangle} \tag{4.13}$$

Since there are two independent event plane from west and east FTPC, the event plane resolution can be estimated by measuring the relative azimuthal angle $\Delta\Psi_2^{\rm FTPC} \equiv 2(\Psi_2^{\rm West} - \Psi_2^{\rm East})$. This is based on the assumption that there are no other correlations except flow effects. Taking into account that the multiplicity of the full event is twice as large as that of the sub-event, the full event plane resolution is given by Equation 4.14

$$\langle\cos[2(\Psi_2 - \Psi_r)]\rangle = \sqrt{2}\langle\cos[2(\Psi_2^A - \Psi_r)]\rangle. \tag{4.14}$$

Figure 4.11 shows the 2nd harmonic TPC and FTPC event plane resolution of v_2 determined in Au + Au collisions at $\sqrt{s_{NN}} = 200$ GeV for 9 different centrality intervals. The TPC resolution of v_2 is pretty good, and it is 0.75 for mini-bias data (0-80%). While

the FTPC resolution of v_2 is much smaller than TPC resolution, and it is about 0.185 for mini-bias data.

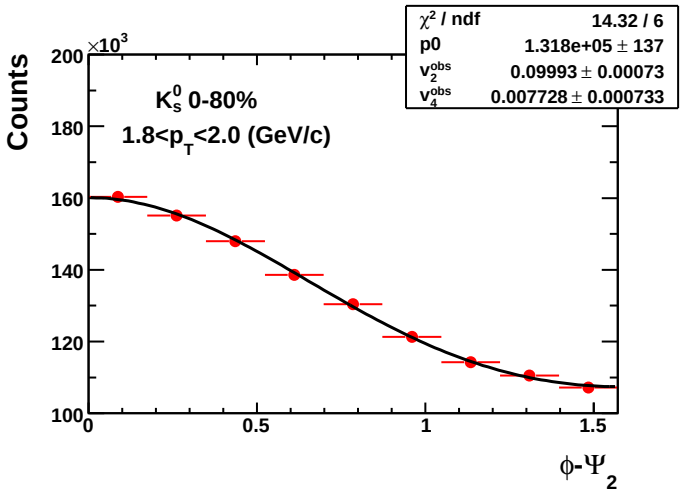

Figure 4.12: $dN/d(\phi - \Psi_2)$ distribution for K^0_S at $1.8 < p_T < 2.0$ GeV/c for $0-80\%$ Au + Au collisions. Black curve is the fitting of data.

After determining the event plane, the identified charged particle v_2 can be directly calculated by $\cos 2(\phi - \Psi)$. For reconstructed particles, the signal and background are firstly fitted as shown in Fig. 4.7. Then, the azimuthal space with respect to event plane $(\phi - \Psi_2)$ is divided in to 9 bins, and we can get the signal counts in each bin by subtracting background. Fig. 4.12 shows an example for K^0_S at $1.8 < p_T < 2.0$ for Au + Au collisions mini-bias (0-80%) data. The observed v_2 and v_4 is extracted by fitting $dN/d(\phi - \Psi_2)$ distribution with Fourier expansion of azimuthal distribution

$$\frac{dN}{d(\phi - \Psi_2)} = N(1 + 2v_2^{\rm obs}\cos(2(\phi - \Psi_2)) + 2v_4^{\rm obs}\cos(4(\phi - \Psi_2))), \tag{4.15}$$

where N, $v_2^{\rm obs}$ and $v_4^{\rm obs}$ are free parameters. The fitting is shown as black curve in Fig. 4.12.

4.5 Invariant Mass Method

In this section, we present invariant mass method to extract v_2 for strange hadrons since we can not directly know whether a reconstructed strange hadron candidate belongs to

signal or background. The result is also compared with event plane method.

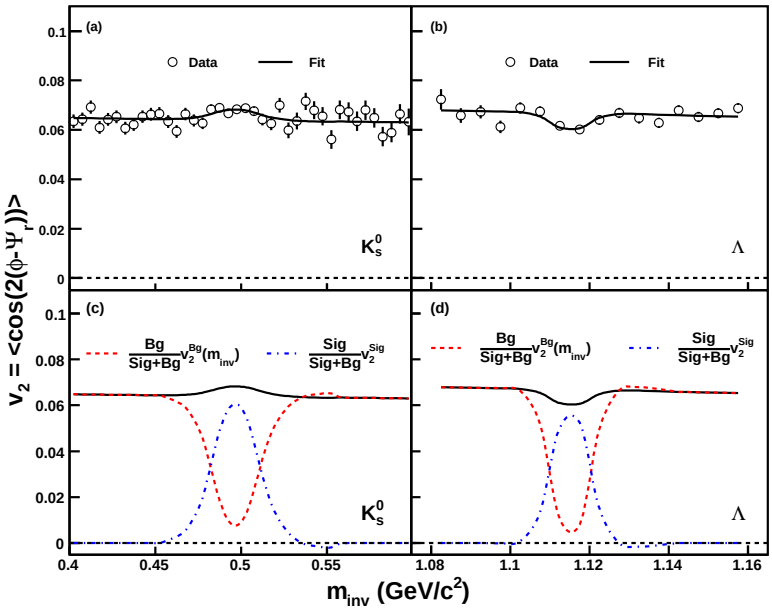

Figure 4.13: (a) K^0_S and (b) Λ candidates v_2 distributions at $1.6 < p_T < 1.8$ GeV/c for 0−80% Au + Au collisions are shown. Red and blue curves refer to (c) signal and (d) background v_2 separately.

The essence of invariant mass method is based on the following Equation [Bor04a]:

$$v_2^{\mathrm{Sig+Bg}}(m_{\mathrm{inv}}) = v_2^{\mathrm{Sig}}\frac{\mathrm{Sig}}{\mathrm{Sig+Bg}}(m_{\mathrm{inv}}) + v_2^{\mathrm{Bg}}(m_{\mathrm{inv}})\frac{\mathrm{Bg}}{\mathrm{Sig+Bg}}(m_{\mathrm{inv}}). \qquad (4.16)$$

The v_2 of all candidates is divided into two parts, one is the signal v_2 multiply the signal yields, and the other is the background v_2 multiply the background yields, as shown in the Eq. [Bor04a]. By fitting the signal and background, as shown in Fig. 4.7, $\frac{\mathrm{Sig}}{\mathrm{Sig+Bg}}$ and $\frac{\mathrm{Bg}}{\mathrm{Sig+Bg}}$ ratio can be obtained. Here we assume that v_2^{Bg} is as a linear function of invariant mass (m_{inv}), and then v_2^{Sig} can be extracted by fitting with Equation 4.16.

To illustrate this method, Figure 4.13 shows an example for K^0_s and Λ. Panel (a) and (b) show invariant mass distribution. A 4^{th} order polynomial fit to describe the background distribution is shown as solid line. $\frac{\mathrm{Bg}}{\mathrm{Sig+Bg}}(m_{\mathrm{inv}})$ is obtained by dividing fit line by data. $\frac{\mathrm{Sig}}{\mathrm{Sig+Bg}}$ is calculated by $(1 - \frac{\mathrm{Sig}}{\mathrm{Sig+Bg}})$. v_2 of K^0_S candidates represented by open circles are calculated and plotted in panel (b). The fitting of v_2 for K^0_S candidates

with Equation 4.16 is shown in solid line. The background contributions and the signal contributions are shown as dashed line and dot-dashed line in (c) along with the combination of them.

The fitting covers a relative wide $m_{\rm inv}$ region. Data points far from the mass peak region come from background contributions, thus $\frac{\rm Bg}{\rm Sig+Bg}$ is equal to 1. $v_2^{\rm Sig+Bg}$ data points in this region have strong constraints on $v_2^{\rm Bg}$ when doing the fit. $v_2^{\rm Sig+Bg}$ data points in the mass region under peak constraint $v_2^{\rm Sig}$ with given $\frac{\rm Sig}{\rm Sig+Bg}$ and $\frac{\rm Bg}{\rm Sig+Bg}$ ratios. A large variation of $v_2^{\rm Sig}$ would lead to an strong disagreement of the fit curves with the measured data. Thus the shape of dip or bump of $v_2^{\rm Sig+Bg}$ in the mass region under peak is not necessary to measure v_2. The systematic uncertainty of this method lies in the estimate of $\frac{\rm Sig}{\rm Sig+Bg}$ and $\frac{\rm Bg}{\rm Sig+Bg}$ ratio as a function of $m_{\rm inv}$. This systematic uncertainty is studied by using different functions to fit the background, which will be discussed in systematics section.

The observed $v_2^{\rm obs}$ ($v_4^{\rm obs}$) need to be corrected with event plane resolution by Eq. 4.12 for both of the methods.

4.6 Cumulant Method

In this section, we introduce the cumulant method which is base on a cumulant expansion of multi-particle azimuthal correlations.

4.6.1 Integral v_2

The principle of the cumulant method is that when cumulant of higher order is considered, the contribution of non-flow effects from lower order correlations will be eliminated. In the following we take a four-particle correlations as an example to illustrate how this approach works.

The measured two-particle correlations can be expressed as flow and non-flow com-

ponents in a perfect detector

$$\langle e^{in(\phi_1-\phi_2)}\rangle = \langle e^{in(\phi_1-\Psi_r)}\rangle\langle e^{in(\Psi_r-\phi_2)}\rangle + \delta_n = v_n^2 + \delta_n, \tag{4.17}$$

where n is the harmonic. The average is taken for all pairs of particles in a certain rapidity and transverse momentum region (typically corresponding to the acceptance of a detector) and for all events in a event sample. The δ_n refers to the non-flow contributions to 2-particle correlation. The measured 4-particle correlations can be decomposed as below:

$$\langle e^{in(\phi_1+\phi_2)-\phi_3-\phi_4}\rangle = v_n^4 + 2\cdot 2\cdot v_n^2\delta_n + 2\delta_n^2. \tag{4.18}$$

In this expression, two factors of "2" in front of the term $v_n^2\delta_n$ correspond to the two ways of pairing (1,3)(2,4) and (1,4)(2,3) and account for the possibility to have non-flow effects in the first pair and flow in the second pair or vice versa. The factor "2" in front of δ_n^2 is from two ways of airing. The 4-particle non-flow correlation is omitted in the expression.

Follows this, the flow contribution can be obtained by subtracting the 2-particle correlation from the 4-particle correlation:

$$\langle\langle e^{in(\phi_1+\phi_2)-\phi_3-\phi_4}\rangle\rangle = \langle e^{in(\phi_1+\phi_2)-\phi_3-\phi_4}\rangle - 2\langle e^{in(\phi_1-\phi_3)}\rangle^2 = -v_n^4, \tag{4.19}$$

where the notation $\langle\langle\cdots\rangle\rangle$ is used for the cumulant. The cumulant of order two is just $\langle\langle e^{in(\phi_1-\phi_2)}\rangle\rangle = \langle e^{in(\phi_1-\phi_2)}\rangle$.

The various quantities of interest are constructed from the real-valued generating function in practise

$$\begin{aligned} G_n(z) &= \prod_{j=1}^{M}[1 + \frac{w_j}{M}(z^* e^{in\phi_j} + z^* e^{-in\phi_j})] \\ &= \prod_{j=1}^{M}[1 + \frac{w_j}{M}(2x\cos(n\phi_j) + 2y\sin(n\phi_j))], \end{aligned} \tag{4.20}$$

where the product runs over M particles detected in a single event and $z = x + iy$ is an arbitrary complex number. This generating function has no physical meaning in itself, but after averaging over events, the coefficients of its expansion in powers of z and $z^* \equiv x - iy$ yield multi-particle azimuthal correlations of arbitrary orders.

In order to obtain the cumulants, one first averages $G_n(z)$ over events, which yields an average generating function $\langle G_n(z)\rangle$, we define

$$C_n(z) \equiv M[\langle G_n(z)\rangle^{1/M} - 1]. \tag{4.21}$$

The cumulant of 2k-particle correlations $c_n\{2k\}$ is the coefficient of $z^k z^{*k}/(k!)^2$ in the power-series expansion of $C_n(z)$.Once the values $C_n(z_{p,q})$ have been computed, they must be averaged over the phase of z:

$$C_p \equiv \frac{1}{q_{max}} \sum_{q=0}^{q_{max}-1} C_n(z_{p,q}), \quad p = 1, 2, 3. \tag{4.22}$$

The cumulants of 2-, 4- and 6-particle correlation are then give respectively by

$$\begin{aligned} c_n\{2\} &= \frac{1}{r_0^2}(3C_1 - \frac{3}{2}C_2 + \frac{1}{3}C_3), \\ c_n\{4\} &= \frac{2}{r_0^4}(-5C_1 - 4C_2 - C_3), \\ c_n\{6\} &= \frac{6}{r_0^6}(3C_1 - 3C_2 + C_3). \end{aligned} \tag{4.23}$$

From the measured $c_n\{2k\}$, we can obtain an estimate of the integral flow, which is denoted by $V_n\{2k\}$:

$$\begin{aligned} V_n\{2\}^2 &= c_n\{2\}, \\ V_n\{4\}^2 &= -c_n\{4\}, \\ V_n\{6\}^2 &= c_n\{6\}/4. \end{aligned} \tag{4.24}$$

Given an estimate of the n^{th} order integrated flow V_n, the estimate of differential flow v_p' (flow in a restricted phase-space window) in any harmonic $p = mn$, where m in an integer. For instance, the 4^{th} order differential flow v_4' can be analyzed using the integrated V_1, V_2, V_3 and V_4 as reference.

4.6.2 Differential v_2

The generating function of the cumulants for studying differential flow is given by

$$D_{p/n}(z) = \frac{e^{ip\psi G_n(z)}}{\langle G_n(z)\rangle}, \tag{4.25}$$

where ψ refers to the azimuthal of the particle of interest. On the right of the equation, the average of the numerator is performed over all particles of interest, while the denominator is averaged over all events. Following the same procedure as in the case of the integrated flow, the cumulant $d_p\{2k+m+1\}$ involving $2k+m+1$ particles is calculated. The differential flow $v'_p\{2k+m+1\}$ is estimated after this.

For instance, the differential flow estimated from the lowest order cumulant is shown for two cases($m=1$ or $m=2$):

$$\begin{aligned} v'_{n/n}\{2\} &= d_{n/n}\{2\}/V_n, \qquad v'_{n/n}\{4\} = d_{n/n}\{4\}/V_n^3, \\ v'_{2n/n}\{3\} &= d_{2n/n}\{3\}/V_n^2, \qquad v'_{2n/n}\{5\} = -d_{2n/n}\{5\}/2V_n^4, \end{aligned} \tag{4.26}$$

The generating functions will be automatically involve all possible k particle correlations when building the k-particle cumulants. Moreover, the formalism removes the non-flow correlations arising from detector inefficiencies. However, the disadvantage is that the use of higher order cumulants is often limited by statistics in real case.

4.7 Mixed Harmonics method

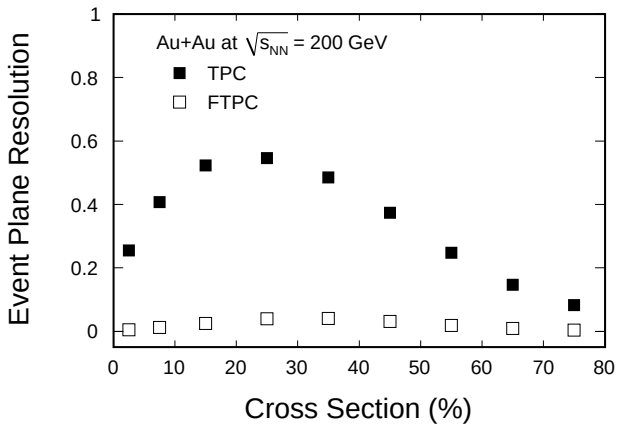

Figure 4.14: The 2nd order TPC event plane resolution and FTPC event plane resolution for v_4 in Au + Au collisions at $\sqrt{s_{NN}} = 200$ GeV for 9 different centrality intervals.

An event plane determined from harmonic m can be used to study the flow of har-

monics $n = km$, where k is an integer. The case of $k > 1$ is called the mixed harmonics method. It allows us to choose the biggest flow signal with largest resolution to reconstruct event plane according to the detectors. At the AGS and SPS, the fixed target setting the detectors usually cover well the region of rapidity where directed flow is large. While at RHIC, we mostly use the method to study higher ($n \geq 4$) harmonics relative to v_2 since it is the strongest signal near midrapidity.

Higher order Fourier coefficient v_4 is expected to become as large as 5% and should be clearly measurable. We used both TPC event plane method and FTPC event plane method to measure v_4. Figure 4.14 shows the 2^{nd} harmonic TPC event plane resolution and FTPC event plane resolution of v_4 determined in Au + Au collisions at $\sqrt{s_{NN}} = 200$ GeV for 9 different centrality intervals. The TPC resolution of v_4 is pretty good, and it is 0.42 for mini-bias data (0-80%). While the FTPC resolution of v_4 is much smaller than TPC resolution, and it is about 0.023 for mini-bias data.

CHAPTER 5

Results I: Azimuthal anisotropy

In this chapter, we present the result of elliptic flow v_2 and the higher harmonic v_4 in Au + Au collisions at $\sqrt{s_{NN}} = 200$ GeV. The results from TPC event plane method, FTPC event plane method and four-particle cumulant method are compared. Dependencies of the flow coefficients on transverse momentum, centrality and particle species are also presented.

5.1 The 2^{nd} order anisotropic flow v_2

5.1.1 Centrality dependence and non-flow effect

Elliptic flow, v_2, has been measured by different methods [Vol09a]. The previous study [Oll95a] shows that the major systematic uncertainty of v_2 measurement is the non-flow effect which has nothing to do with reaction plane, i.e., HBT, jet, resonance decay, etc. Therefore, it is important to study the non-flow effect to precise the measurement for flow study.

Here, the charged particle v_2 is calculated by TPC event plane method, FTPC event plane method and four-particle cumulant method. With large statistic data sample obtained in Au+Au collisions at $\sqrt{s_{NN}} = 200$ GeV during RHIC Run VII, anisotropic flow coefficients can be measured to higher p_T range for different centralities.

Figure 5.1 shows charged particle v_2 in centrality $20\% - 60\%$ at mid-rapidity ($|\eta| < 1$) for Au + Au collisions at $\sqrt{s_{NN}} = 200$ GeV as a function of transverse momentum p_T. The error bars are statistical only. The v_2 values are obtained with the TPC event plane

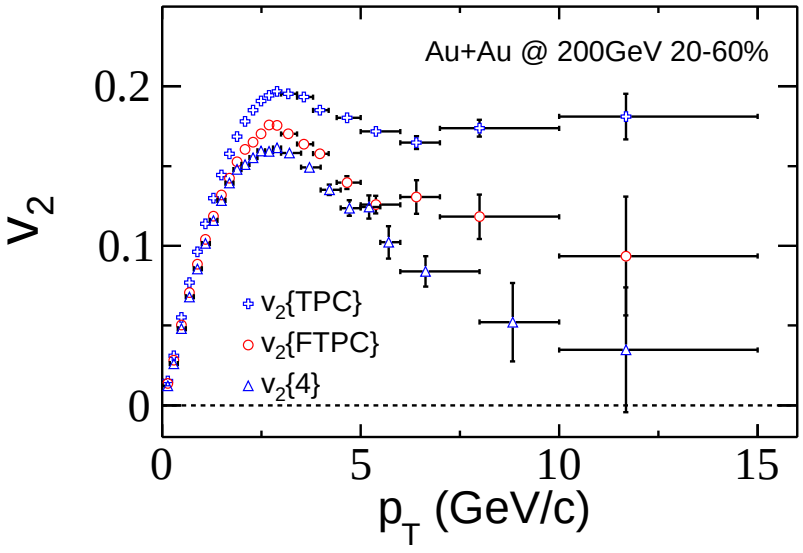

Figure 5.1: Charged particle elliptic flow (v_2) as a function of transverse momentum (p_T) for centrality $20\% - 60\%$ in Au + Au collisions at $\sqrt{s_{NN}} = 200$ GeV from the TPC event plane method (crosses), FTPC event plane method (circles) and four-particle cumulant method (triangles).

method (denoted by $v_2\{\text{TPC}\}$), FTPC event plane method (denoted by $v_2\{\text{FTPC}\}$) and four-particle cumulant method (denoted by $v_2\{4\}$). A systematic difference is observed for the values obtained from the three methods, especially between the TPC event plane method and four-particle cumulant method. v_2 obtained from TPC event plane method which includes non-flow effect shows the biggest value compared with other methods. v_2 obtained from FTPC event plane method, in which non-flow effect can be significant reduced by the large η gap, shows smaller value than $v_2\{\text{TPC}\}$. $v_2\{4\}$ can be considered as lowest bound of v_2 since it is not sensitive to non-flow and flow fluctuation will only make $v_2\{4\}$ smaller than it should be. There are also some differences between $v_2\{\text{FTPC}\}$ and $v_2\{4\}$, which may caused by both non-flow effect and v_2 fluctuation [Ack01a]. It is clear that the difference increases with transverse momentum, and it is significant when p_T is larger than 3 GeV/c, where non-flow effect plays an important role.

The plot shows that v_2 firstly increases with p_T, then begins decreasing after gets the maximum value at about 3 GeV/c. At low p_T region, v_2 can be well described

by hydrodynamics [Huo01a, Gyu01a]. However, the data starts to deviate from ideal hydrodynamics at about 1 GeV/c. The position of the onset of the deviation from ideal hydrodynamics and its magnitude are thought to constrain the shear viscosity of the fluid [Gyu01a]. Particle production at $p_T > 2$ GeV/c will be dominated by hard or semi-hard process. It is believed that fragmentation of high energy partons (jets) coming from initial hard scattering begins to dominate the particle production. Perturbative calculation predicts that high energy partons traversing nuclear matter lose energy through induced gluon radiation [Wan92a]. The energy loss called "jet quenching" is expected to depend strongly on the color charge density of the created system and the transverse path length of the propagating parton. In non-central collisions, the initial geometry of the overlap region has an almond shape as shown in Fig. 2.4. Partons emit to different directions may experience different path lengths and therefore different energy loss. This will cause azimuthal anisotropy in the hadron production. Thus, the turning point of v_2 signals the onset of contribution of hard processes and the magnitude of parton energy loss [Wan01a, Gyu02a]. Being consistent with scenario of parton energy loss [Wan01a], the estimated elliptic flow from the four-particle cumulant method, which is not sensitive to non-flow effect, shows a decreasing trend at high p_T and it is sizable up to 10 GeV/c.

Figure 5.2 shows charged v_2 as a function of p_T for centrality $70\% - 80\%$, $60\% - 70\%$, $50\% - 60\%$, $40\% - 50\%$, $30\% - 40\%$, $20\% - 30\%$, $10\% - 20\%$, $5\% - 10\%$ and $0 - 5\%$ in Au + Au collisions at $\sqrt{s_{NN}} = 200$ GeV. As before, v_2 obtained from the TPC event plane method (crosses), FTPC event plane method (circles) and four-particle cumulant method (triangles) are compared. As p_T increases, $v_2\{\text{TPC}\}$ continues increasing in most peripheral collisions, i.e., centrality $70\% - 80\%$ and $60\% - 70\%$, while it reaches the maximum value at 3 GeV/c in other centralities. $v_2\{\text{FTPC}\}$ and $v_2\{4\}$ have similar trend except the most central collisions, i.e., $0 - 5\%$. We failed to get the value of $v_2\{4\}$ in most central collisions because $2\langle(v_2)^2\rangle^2 - \langle(v_2)^4\rangle$ is negative. This indicates that $\langle(v_2)^4\rangle/\langle(v_2)^2\rangle^2 > 2$. It is suggested that if $2\langle(v_2)^2\rangle^2 - \langle(v_2)^4\rangle$ is scaled by $v_2\{2\}^4$, the ratio should be around -1, if $\langle(v_2)^4\rangle/\langle(v_2)^2\rangle^2 \simeq 3$. This would give invaluable information on the mechanism driving elliptic flow fluctuations.

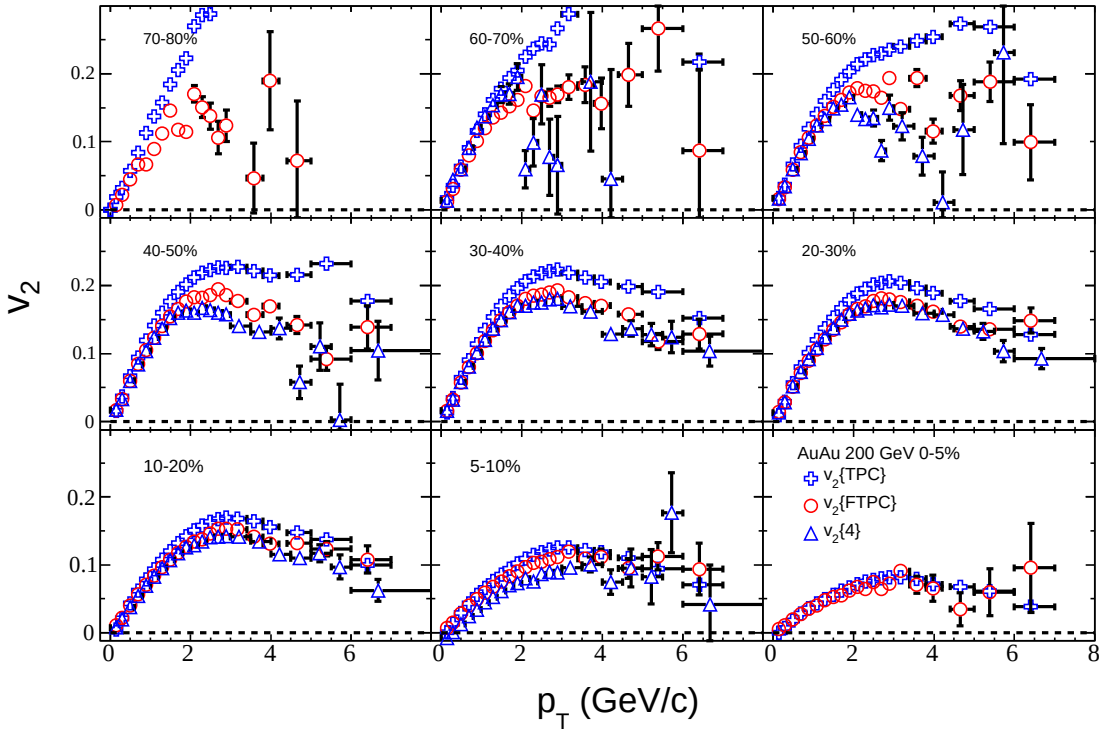

Figure 5.2: Charged particle elliptic flow (v_2) as a function of transverse momentum (p_T) for centrality $70\% - 80\%$, $60\% - 70\%$, $50\% - 60\%$, $40\% - 50\%$, $30\% - 40\%$, $20\% - 30\%$, $10\% - 20\%$, $5\% - 10\%$ and $0 - 5\%$ in Au + Au collisions at $\sqrt{s_{NN}} = 200$ GeV from the TPC event plane method (crosses), FTPC event plane method (circles) and four-particle cumulant method (triangles).

Comparing v_2 obtained from different methods, we can see that the non-flow effect is significant in high p_T region than in low p_T region, and in is more important in peripheral collisions than in central collisions.

5.1.2 Particle species dependence

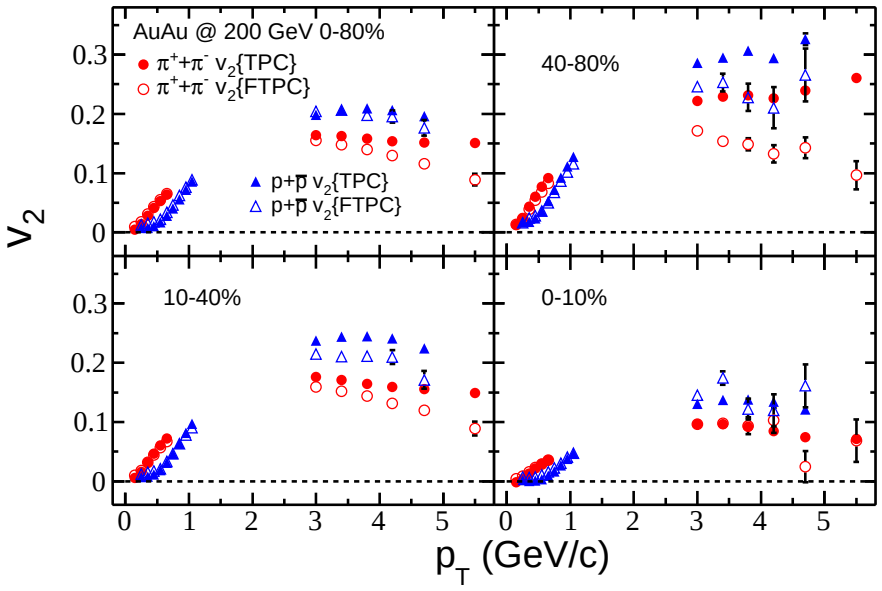

Figure 5.3: Charged pions and (anti)protons v_2 as a function of p_T for centrality $0-80\%$, $40\%-80\%$, $10\%-40\%$ and $0-10\%$ in Au + Au collisions at $\sqrt{s_{NN}} = 200$ GeV. Solid points are the results from TPC event plane while open points are the results from FTPC event plane.

Figure 5.3 shows v_2 of charged pions and (anti)protons as a function of p_T in centrality bins $0-80\%$, $40\%-80\%$, $10\%-40\%$ and $0-10\%$ in Au + Au collisions at $\sqrt{s_{NN}} =$ 200 GeV, and the errors are statistical only. In $p_T < 1$ GeV/c region, v_2 of (anti)proton is smaller than v_2 of pion which can be explained by hydrodynamics. The collective radial motion boosts particles to higher average momenta, heavier particles gain more momentum than lighter ones. This leads to a flattening of the spectra at low transverse momenta. This flattening reduces v_2 at low p_T, and therefore the heavier the particle the more the rise of $v_2(p_T)$ is shifted towards at larger p_T [Huo01a]. While in large p_T region, v_2 of proton is larger than v_2 of pion which can be explained by coalescence

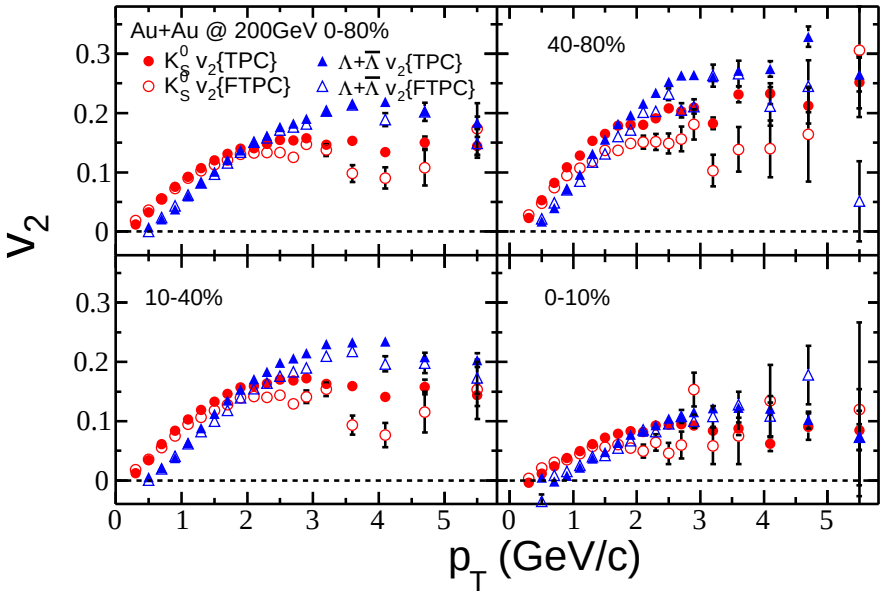

Figure 5.4: K^0_S and Λ v_2 as a function of p_T for centrality $0-80\%$, $40\%-80\%$, $10\%-40\%$ and $0-10\%$ in Au + Au collisions at $\sqrt{s_{NN}} = 200$ GeV. Solid points are the results from TPC event plane while open points are the results from FTPC event plane.

or recombination model [Mol03a, Lin02a, Hwa03b, Fri03a]. In those models, hadron v_2 (v_2^h)at intermediate p_T ($2 < p_T < 5$ GeV/c) is related to the v_2 of quarks v_2^q in QGP by the relationship: $v_2^h(p_T) \approx n_q v_2^q(p_T/n_q)$.

Also, the v_2 values from from the TPC event plane method and FTPC event plane method are compared. It is clear that FTPC result is significant smaller than TPC result in high p_T region, because FTPC can reduce the non-flow effect by large η gap. We observed the non-flow effect is larger in peripheral collisions than in central collisions for both charged pions and (anti)protons.

Figure 5.4 shows v_2 of K^0_S and Λ as a function of p_T in centrality bins $0-80\%$, $40\%-80\%$, $10\%-40\%$ and $0-10\%$ in Au + Au collisions at $\sqrt{s_{NN}} = 200$ GeV. The mass ordering is also observed at low p_T, while v_2 of Λ is larger than v_2 of K^0_S at intermediate and high p_T range. The v_2 values from from the TPC event plane method and FTPC event plane method are compared. It is clear that FTPC result is significant smaller than TPC result in high p_T region since the non-flow effect is reduced by large η

gap between two FTPCs. And the non-flow effect is larger in peripheral collisions than in central collisions for both K^0_S and Λ.

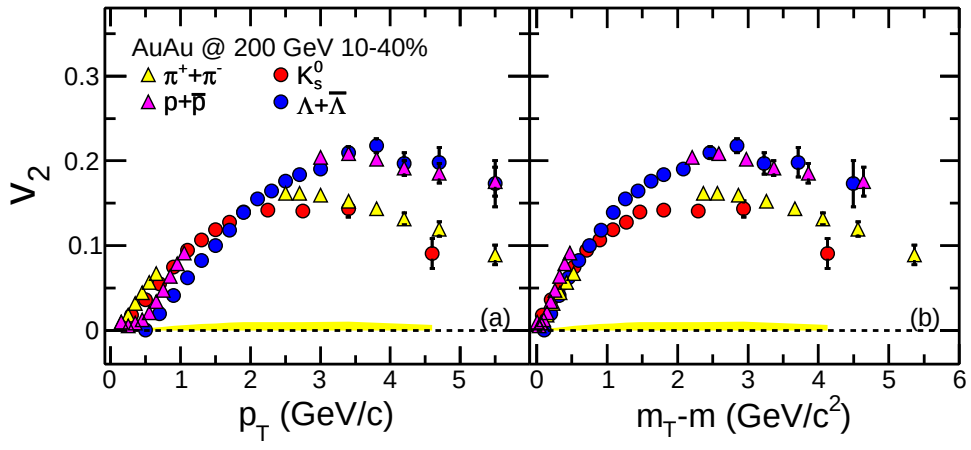

Figure 5.5: v_2 of $\pi^{\pm}$ (solid triangle), p ($\bar{p}$) (solid circle), K^0_S (open triangle) and $\Lambda(\bar{\Lambda})$ (open circle) with FTPC event plane for centrality $10-40\%$ in Au + Au collisions at $\sqrt{s_{NN}} = 200$ GeV. The errors are statistical only, and the systematic uncertainty of nonflow is shown as shaded band at bottom.

The results for $\pi^{\pm}$, p ($\bar{p}$), K^0_S and Λ ($\bar{\Lambda}$) at mid(pseudo)rapidity $|\eta| < 1$ are shown in Fig. 5.5 for $10-40\%$ centrality. At low p_T, the hadron mass ordering of v_2 (for a given p_T , the heavier the hadron, the smaller v_2) is observed (left panel). During the process of a hydrodynamic expansion, the radial flow plays an important role [Huo01a], and the pressure gradient that drives elliptic flow is directly linked to the collective kinetic energy of the emitted particles. Thus one expects v_2 for different particle species should scale with $m_T - m$ [Ada06a], where $m_T = \sqrt{m^2 + p_T^2}$. Following [Ada07a], in the right panel we present v_2 as a function of $m_T - m$. Good scaling is observed up to $m_T - m = 1$ GeV/c^2, beyond that, v_2 of different particles becomes diverged. Noticeably, v_2 from all particles species showing signs of decrease after reaching their maximum around $2-2.5$ GeV/c^2 in $m_T - m$. It is argued that jet conversion may cause a large number of extra strange quarks to be produced throughout the out-of-plane direction, thus the v_2 of kaons is systematically smaller than v_2 of pions and the difference between strange and non-strange baryons is much smaller than that between strange and non-strange mesons [Liu08a]. However, we can not make a definite conclusion due to the large

statistic errors of identified particles v_2 at large p_T for this dataset.

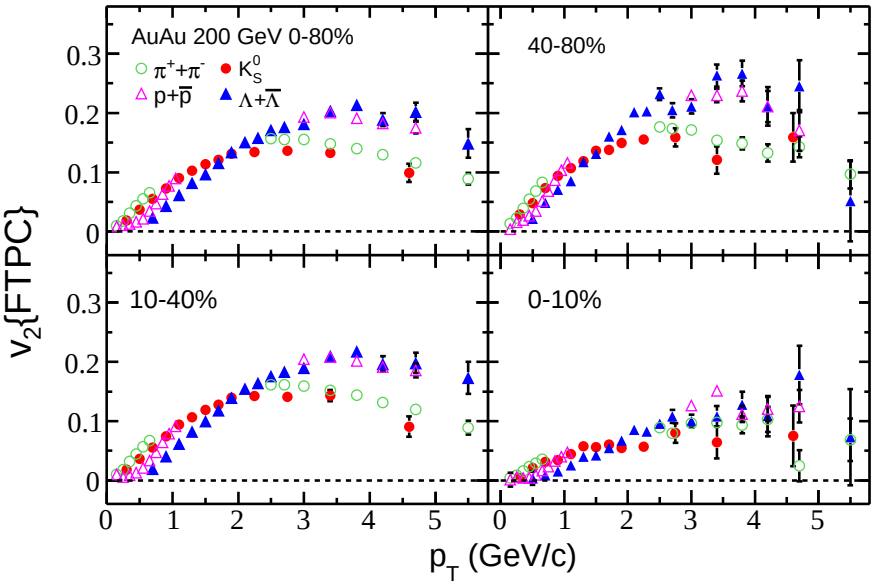

Figure 5.6: Charged pions (open triangles), (anti)protons (solid triangles), K^0_S (open circles) and Λ (solid circles) v_2 from FTPC event plane as a function of p_T for centrality $0-80\%$, $40\%-80\%$, $10\%-40\%$ and $0-10\%$ in Au + Au collisions at $\sqrt{s_{NN}} = 200$ GeV.

The major systematic uncertainty in this analysis comes from "nonflow", which are correlations not related to reaction plane. We take advantage of the large η gap between TPC and FTPCs to reduce the short-range correlations between particles of interest and particles used to reconstruct the event plane. The remaining nonflow correlations, along with event-by-event flow fluctuations, are estimated by the difference between v_2 obtained from FTPC event plane ($v_2\{\text{FTPC}\}$) and v_2 obtained from the multi-particle cumulant method ($v_2\{\text{LYZ}\}$). The Lee-Yang Zero method is supposed to suppress the known non-flow effects such as jets, resonances [Bha03a]. However, the Lee-Yang Zero method yields larger statistical errors [Abe08a]. Such nonflow effect is about 7% of v_2 value for strange hadrons as shown by shaded band at the bottom. Our estimation of systematic error stops at $m_T - m = 3$ GeV/c^2, because $v_2\{\text{LYZ}\}$ analysis is more statistics hungry and cannot reach the same p_T as that reached by $v_2\{\text{FTPC}\}$ method.

Figure 5.6 shows all the identified particles v_2 (Charged pions (open triangles),

(anti)protons (solid triangles), K^0_S (open circles) and Λ (solid circles)) from FTPC event plane as a function of transverse momentum (p_T) for centrality $0-80\%$, $40\%-80\%$, $10\%-40\%$ and $0-10\%$ in Au + Au collisions at $\sqrt{s_{NN}} = 200$ GeV.

5.1.3 Number of constituent quark scaling of v_2

One of the major findings from previous studies is that, at intermediate p_T (from $p_T \sim$ 1.5 GeV/c to roughly 4 -5 GeV/c), baryon and meson elliptic flow, if scaled by their corresponding number of constituent quarks (n_q) and plotted against (p_T/n_q), converges. It is so called the Number of Constituent Quark (NCQ) scaling, and it implies that hadrons are produced out of a deconfined partonic state by coalescence [Mol03a, Lin02a] or recombination [Hwa03b]. More importantly, as underlying quark flow is needed to explain the data, it provides the strongest evidence for the partonic collectivity.

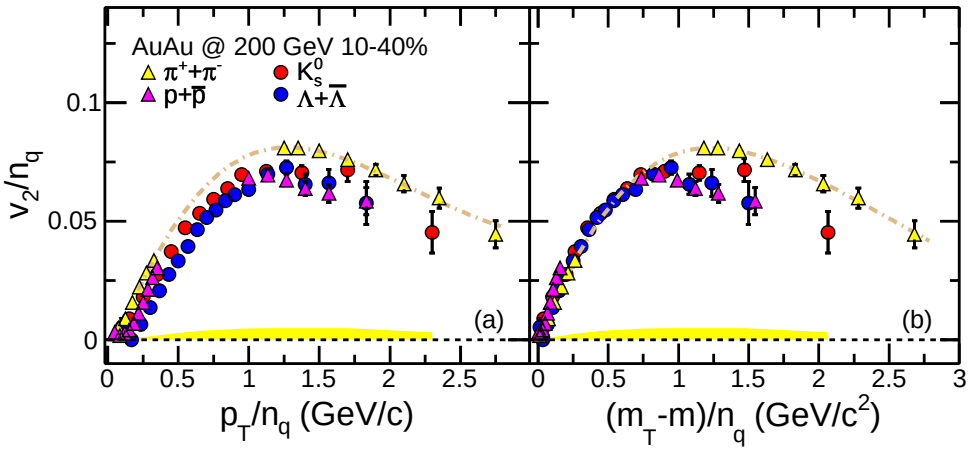

Figure 5.7: The v_2/n_q of charged pions (open triangles), (anti)protons (solid triangles), K^0_S (open circles) and Λ (solid circles)from FTPC event plane as a function of p_T/n_q for centrality $0-80\%$, $40\%-80\%$, $10\%-40\%$ and $0-10\%$ in Au + Au collisions at $\sqrt{s_{NN}} = 200$ GeV.

It is expected that such scaling will eventually break down at large p_T, at which the hard process begin to kick in and particles are no longer produced by quark coalescence. Thus it is desirable to locate the p_T range where it starts to break down – that will allow us to understand the transition of particle production mechanisms. It is as well important to examine the pattern with which the NCQ scaling breaks for various hadrons. Such

pattern will not only shed a light on the dynamics of jet fragmentation, it will also, being served as a counter example of NCQ scaling, deepen our understanding of quark coalescence.

In order to test the NCQ scaling at large p_T, we plot v_2/n_q as a function of p_T/n_q and $(m_T-m)/n_q$ in Figure 5.7 in centrality $10\%-40\%$ in Au + Au collisions at $\sqrt{s_{NN}} = 200$ GeV. The latter works at low p_T because the mass effect has been taken into account. The remaining systematical error in $v_2\{\text{FTPC}\}$, which is common for different particle species, is represented by the shaded band at bottom. This error is estimated by studying the difference between $v_2\{\text{FTPC}\}$ and $v_2\{\text{LYZ}\}$ for reconstructed particles K^0_S and Λ ($\bar{\Lambda}$). Since we can not identify charged pions at intermediate p_T, a phenomenologically motivated function [Sor09a]

$$v_2/n_q = \frac{a+bx+cx^2}{1+\exp[\frac{-(x-d)}{e}]} - \frac{a}{2} \tag{5.1}$$

is used to fit the v_2 of pions. Here x refers to p_T/n_q or $(m_T-m)/n_q$. There is no physical meaning to the function or the five fit parameters but simply be used as a convenient reference.

The plot shows that NCQ scaling works well at low p_T range, while the scaling breaks down at $(m_T - m)/n_q > 1$ GeV/c^2. It seems that baryons and mesons follow their own group again after break down for $(m_T - m)/n_q > 2$ GeV/c, however considering the errors from our current measurements we cannot make a definite conclusion.

The centrality dependence of NCQ scaling is plotted in Fig. 5.10 and Fig. 5.9 as function of p_T/n_q and $(m_T - m)/n_q$, respectively. From the plot we can see that, at intermediate p_T range, NCQ scaling works well for all the centralities. However, due to the large statistical errors of the dataset, the breaking of NCQ scaling is inconclusive for most central and most peripheral collisions.

To quantify the divergence from NCQ scaling, in Fig. 5.10 we present the difference between v_2/n_q for baryons and mesons, then divided by their average: ((B - M)/(B + M)/2). The deviation of v_2/n_q for lambda (proton) from the fitted formula of pions as shown in Fig. 5.10 is calculated point by point, and scaled by the sum of v_2/n_q of lambda (proton) and the corresponding value from the fitted formula as a function of

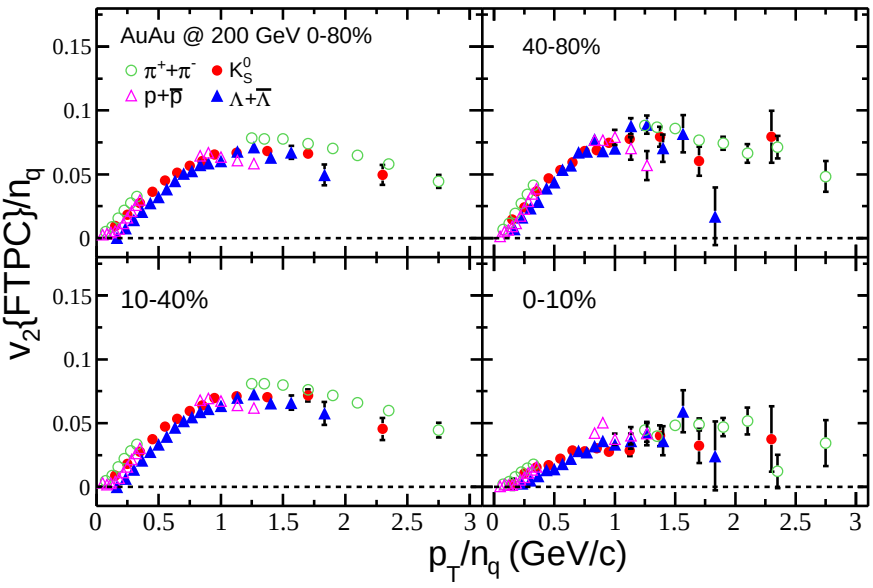

Figure 5.8: The v_2/n_q of charged pions (open triangles), (anti)protons (solid triangles), K^0_S (open circles) and Λ (solid circles)from FTPC event plane as a function of p_T/n_q for centrality $0-80\%$, $40\%-80\%$, $10\%-40\%$ and $0-10\%$ in Au + Au collisions at $\sqrt{s_{NN}} = 200$ GeV.

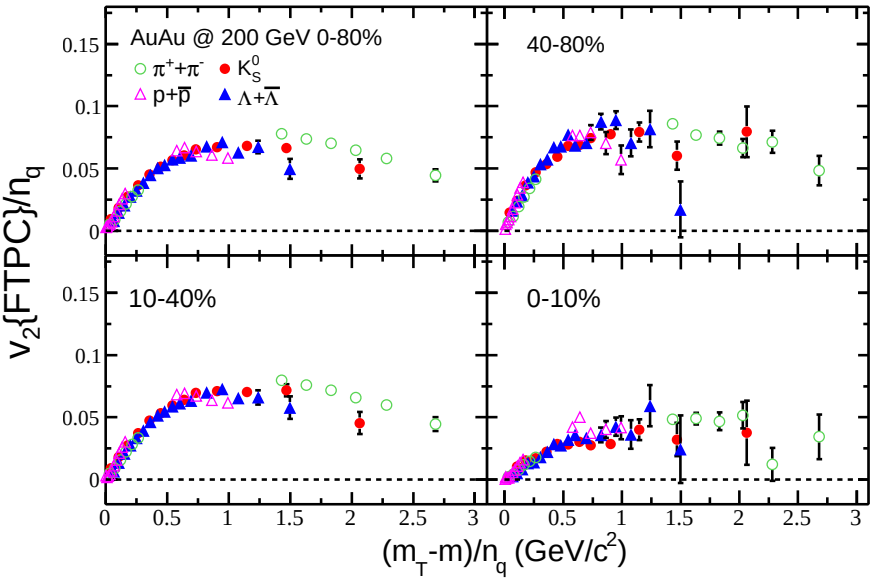

Figure 5.9: The v_2/n_q of charged pions, (anti)protons, K^0_S and Λ from FTPC event plane as a function of $(m_T - m)/n_q$ for centrality $0-80\%$, $40\%-80\%$, $10\%-40\%$ and $0-10\%$ in Au + Au collisions at $\sqrt{s_{NN}} = 200$ GeV.

(a) p_T/n_q and (c) $(m_T - m)/n_q$. The deviation is about 20% from 0.5 up to $p_T/n_q \simeq 1.5$ GeV/c, while it is close to 0 from 0.5 up to $m_T - m \simeq 1$ GeV/c^2. Although the statistical error is large, we still can see the decreasing trend of data as p_T increases. The similar calculation is done with kaon as a reference in Fig. 5.10(b) and (d); similar trend but smaller difference between baryons and kaons is observed. The shaded boxes are the systematic uncertainty due to nonflow, which is mostly canceled in the numerator but is enhanced in the denominator, thus the magnitude of the ratio would be even larger if the nonflow could be completely removed. Note that NCQ scaling is not expected to be a perfect scaling, as evidence by 5% from zero for models that take account realistic effects. However, our data shows much larger deviation than this value for the pions. This indicates that further theoretical work is needed in order to understand the details of the species dependence of v_2 at intermediate p_T.

Model predictions are also shown in the plot for comparison. Two of these models attempt to improve the naive NCQ scaling by introduction of realistic effects. The model that takes into account finite width in the hadron wave function [Gre04a] describes the data reasonably well in the region $0.5 < p_T/n_q < 1.5$ GeV/c when compared with kaons (panel (b)), but not as well when pions are chosen to represent the mesons (panel (a)). The model that adds sea quarks and gluons to the hadron structure is also shown. In this model, the lowest fock state [Fri03a] refers to the recombination of constituent quarks $|q\bar{q}\rangle$ or $|qqq\rangle$ only, while higher fock states ($C_2 = 0.3$) refers to moderate $|q\bar{q}g\rangle$ or $|qqqg\rangle$ contribution. The ratio of this model is slightly larger than data points. Both of the two models try to improve the naive NCQ scaling at intermediate p_T, and they are not expected to explain the difference at large p_T, as seen in this plot. A similar difference between data and models is observed (lower panels) if we assume mesons and baryons to be pions and protons (lambdas) and plotted as a function of $(m_T - m)/n_q$, respectively, in these two models. The model that includes a resonance decay effect [Gre04a] describes data slightly better than other models in the low p_T region, and beyond that region, it gives almost identical results as that given by the same model without resonance decay effect. This is understood as that the resonance effect is mostly relevant at low p_T [Don04a].

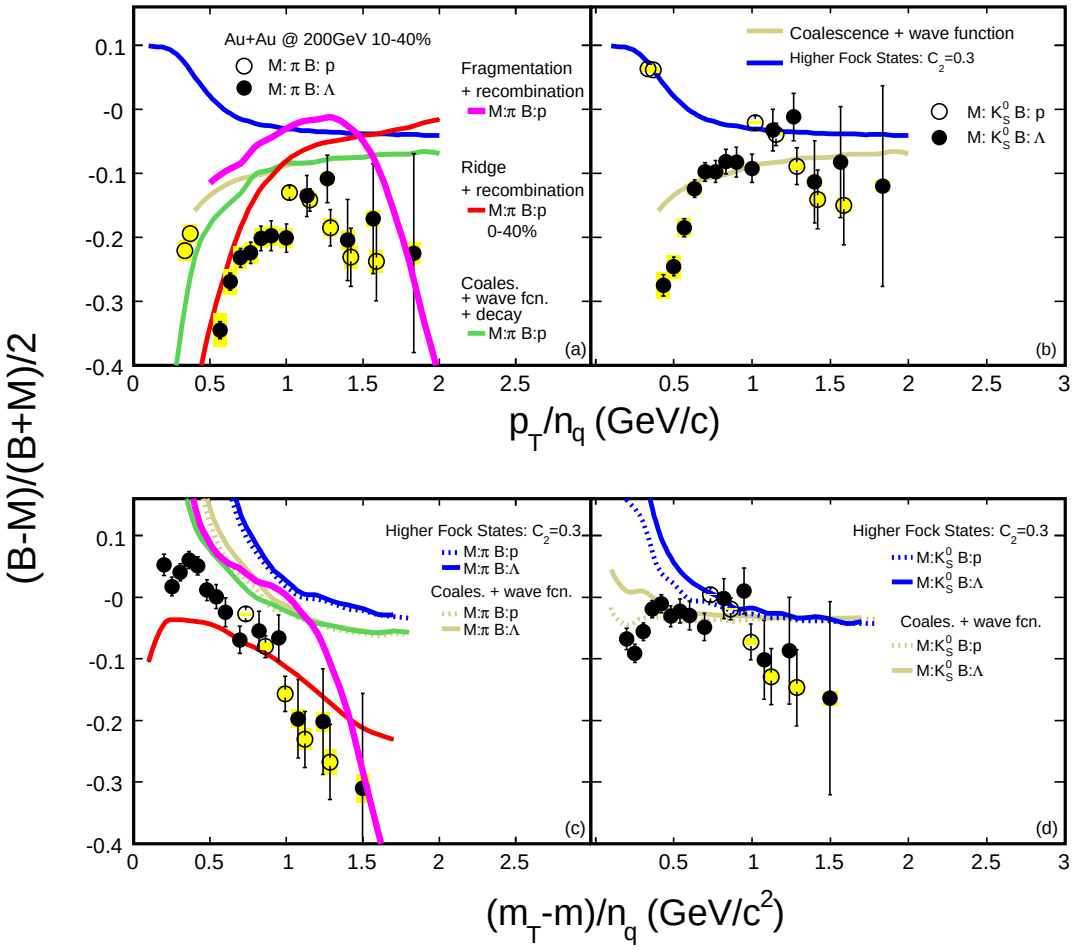

Figure 5.10: The v_2/n_q of charged pions (open triangles), (anti)protons (solid triangles), K^0_S (open circles) and Λ (solid circles)from FTPC event plane as a function of p_T/n_q for centrality $0-80\%$, $40\%-80\%$, $10\%-40\%$ and $0-10\%$ in Au + Au collisions at $\sqrt{s_{NN}} = 200$ GeV.

In Fig. 5.10, we also compare our data with models predicting NCQ violation at large p_T. In the Ridge + recombination model [Chi08a], partons are divided into two groups: soft thermal partons and shower partons created by hard partons. The formation of ridges due to weak jets will affect the azimuthal distribution, thus in the range from intermediate to large p_T, the thermal and shower partons contribute to v_2 differently which will cause the breaking of NCQ scaling. This effect looks prominent if viewed with $(m_T - m)/n_q$ but much less significant with p_T/n_q. The p_T/n_q is believed to be a more relevant quantity to address the NCQ scaling, and has been used in most of coalescence models [Mol03a, Hwa03b, Fri03a, Lin02a]. Our analysis illustrates that the choice of $m_T - m$ versus p_T can change the conclusions drawn from a study of NCQ scaling. In the Fragmentation + Recombination model [Fri03a], the competition between recombination of thermalized partons and fragmentation from perturbatively scattered partons is discussed. A violation of NCQ scaling is predicted coming from the perturbative QCD. It shows a decreasing trend for both p_T/n_q and $(m_T - m)/n_q$. From the model discussions above, only the Fragmentation + Recombination model can explain the trend, as well as the magnitude, at large p_T/n_q and $(m_T - m)/n_q$ which may indicate that the hard process is the most responsible cause for the possible deviation from NCQ scaling for this region.

5.2 The 4^{th} order anisotropic flow v_4

5.2.1 Centrality dependence and non-flow effect

Higher order Fourier coefficient v_4 is consider to be significant for intermediate to large transverse momenta. To study the non-flow effect on v_4, the charged particle v_4 is calculated by TPC event plane method and FTPC event plane method, both has mixture of harmonics by using the second order event plane to study v_4.

Figure 5.11 shows charged particle v_4 in centrality $0 - 80\%$ at mid-rapidity ($|\eta| < 1$) for Au + Au collisions at $\sqrt{s_{NN}} = 200$ GeV as a function of transverse momentum p_T. Here the 2^{nd} harmonic reconstructed the event plane is used. The so-called "mixed-

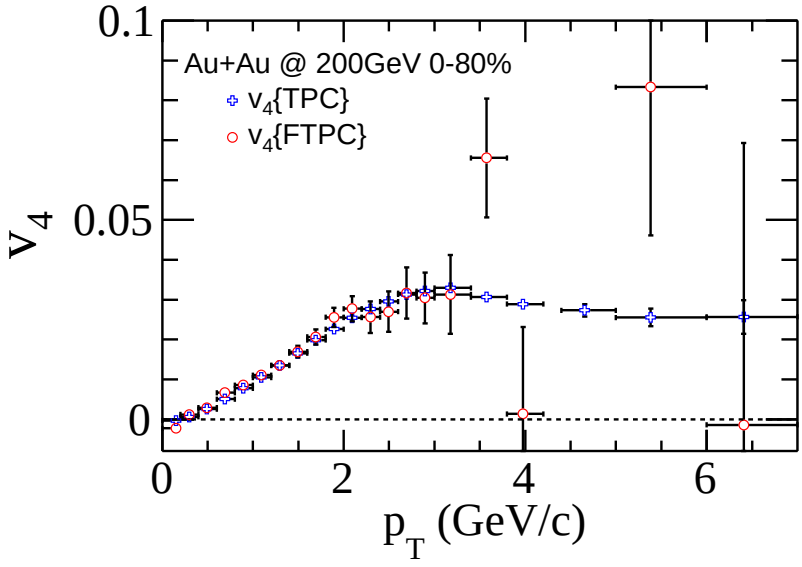

Figure 5.11: Charged particle v_4 as a function of transverse momentum (p_T) for centrality $0-80\%$ in Au + Au collisions at $\sqrt{s_{NN}} = 200$ GeV from the TPC event plane method (crosses) and FTPC event plane method (circles).

harmonic" method can reduce the non-flow effect. The v_4 values obtained from the TPC event plane method (denoted by $v_4\{\text{TPC}\}$) and FTPC event plane method (denoted by $v_4\{\text{FTPC}\}$) are compared. v_4 is observed to increase with p_T up to 3 GeV/c, and no significant difference is found between $v_4\{\text{TPC}\}$ and $v_4\{\text{FTPC}\}$ for p_T lower than 3 GeV/c region since some of the non-flow effects are removed by mixed-harmonic method and is not significant for low p_T region. The low FTPC v_4 resolution as shown in Fig 4.14 causes large errors for $v_4\{\text{FTPC}\}$. Therefore, the non-flow effect is inconclusive at high p_T region due to the errors.

Figure 5.12 shows charged particle v_4 as a function of transverse momentum (p_T) for centrality $70-80\%$, $60-70\%$, $50-60\%$, $40-50\%$, $30-40\%$, $20-30\%$, $10-20\%$, $5-10\%$ and $0-5\%$ in Au + Au collisions at $\sqrt{s_{NN}} = 200$ GeV. As before, v_4 is obtained from the TPC event plane method (crosses) and FTPC event plane method (circles). We can see that the centrality dependence of v_4 is quite similar as that of v_2. For peripheral collisions, as centrality $70\%-80\%$ and $60\%-70\%$, $v_4\{\text{TPC}\}$ continues increasing which may caused by non-flow effect or v_4 fluctuation. While for other centralities, v_4 gets

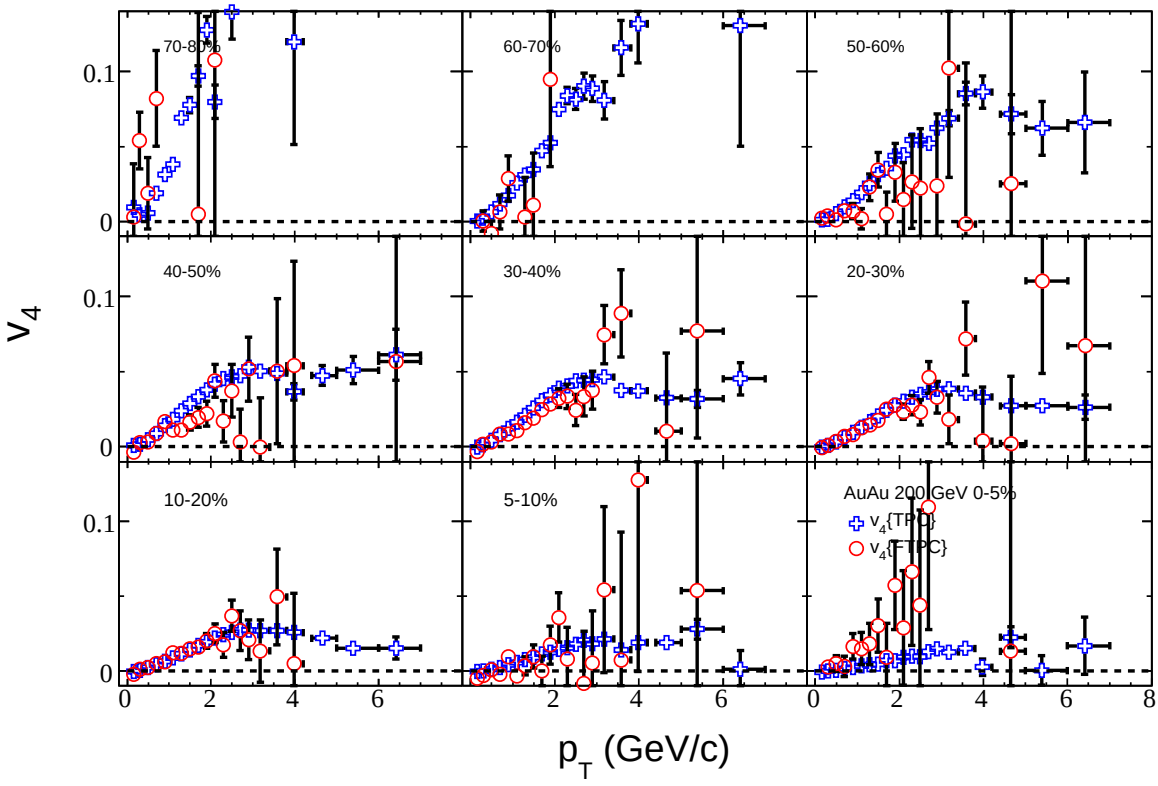

Figure 5.12: Charged particle v_4 as a function of transverse momentum (p_T) for centrality $70-80\%$, $60-70\%$, $50-60\%$, $40-50\%$, $30-40\%$, $20-30\%$, $10-20\%$, $5-10\%$ and $0-5\%$ in Au + Au collisions at $\sqrt{s_{NN}} = 200$ GeV from the TPC event plane method (crosses) and FTPC event plane method (circles).

maximum value and begins to decrease at about at 3 GeV/c. By comparing the v_4 values in mid-central centralities, i.e., $40-50\%$, $30-40\%$, $20-30\%$, we can also see that the non-flow effect is larger in peripheral collisions than in central collisions although the errors are large.

5.2.2 Particle species dependence

v_4 of reconstructed particles K^0_S and Λ ($\bar{\Lambda}$) is shown in Figure 5.13 as a function of transverse momentum p_T for centrality $0\% - 80\%$ at mid-rapidity ($|\eta| < 1$) in Au + Au collisions at $\sqrt{s_{NN}} = 200$ GeV. At low p_T, the v_4 for K^0_S is larger than for Λ ($\bar{\Lambda}$). This mass ordering effect is similar as that of v_2. Both v_2 for K^0_S and v_2 for Λ increase with p_T until reach their peak values at intermediate p_T (~ 3 GeV/c). When p_T is larger than 3 GeV/c, the heavier baryon (Λ) is larger than that of the lighter mesons (K^0_S).

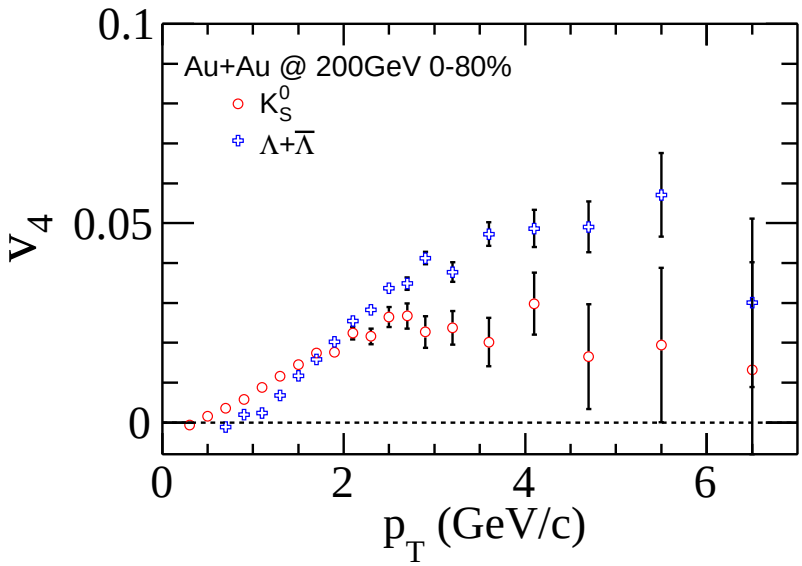

Figure 5.13: K^0_S and $\Lambda + \bar{\Lambda}$ v_4 as a function of transverse momentum (p_T) for centrality $0 - 80\%$ in Au + Au collisions at $\sqrt{s_{NN}} = 200$ GeV from the TPC event plane method.

The centrality dependence of v_4 for K^0_S and Λ ($\bar{\Lambda}$) is shown in Figure 5.14. Similar centrality dependence as charged particles is observed for both K^0_S and Λ ($\bar{\Lambda}$). The largest v_4 amplitude is observed in peripheral collisions while the smallest amplitude is observed in central collisions. The particle type dependence is similar as v_2 in all

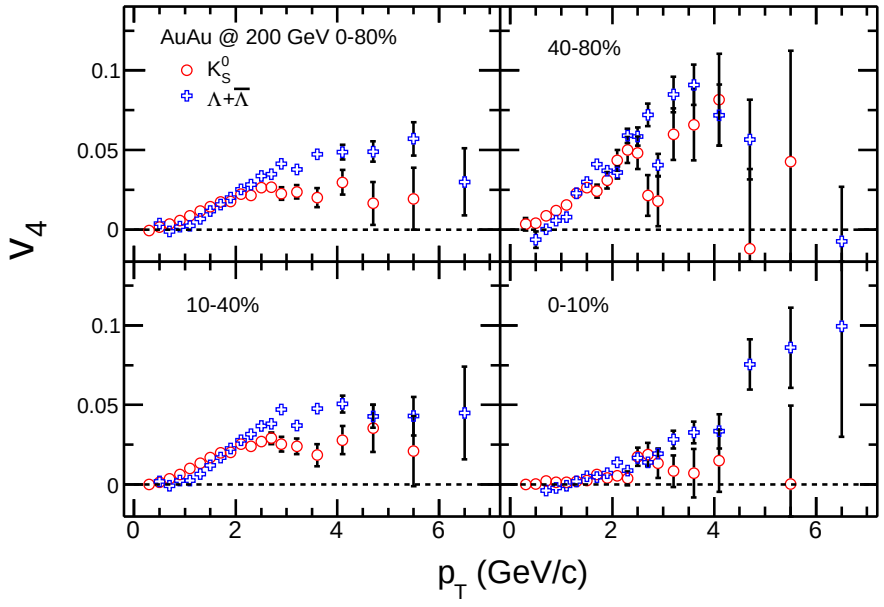

Figure 5.14: K^0_S (circles) and Λ (squares) v_4 as a function of transverse momentum (p_T) for centrality $0-80\%$, $40-80\%$, $10-40\%$ and $0-10\%$ in Au + Au collisions at $\sqrt{s_{NN}} = 200$ GeV from the TPC event plane method.

centralities. At low p_T, v_2 for K^0_S is larger than for Λ, while v_2 for K^0_S is smaller than for Λ at intermediate and large p_T.

5.2.3 Number of constituent quark scaling of v_4

In hydrodynamic calculation [Cle09a], particle v_2 is related to fluid 4-velocity. The ϕ dependence of particle distribution results from a similar ϕ dependence of the fluid 4-velocity:

$$u(\phi) = U(1 + 2V_2 \cos 2\phi + 2V_4 \cos 4\phi + \cdots), \tag{5.2}$$

where ϕ is the azimuthal angle of the fluid velocity with respect to the participant plane. And the second (fourth) coefficient V_2 (V_4) can be related to particle v_2 and v_4 as

$$\begin{aligned} v_2(p_T) &= \frac{V_2 U}{T}(p_T - m_T v) \\ v_4(p_T) &= \frac{1}{2}v_2(p_T)^2 + \frac{V_4 U}{T}(p_T - m_T v), \end{aligned} \tag{5.3}$$

where $v = U/\sqrt{1+U^2}$. Thus v_4 is the the sum of two contributions: an "intrinsic" v_4 proportional to the $\cos 4\phi$ term in the fluid velocity distribution, V_4, and a contribution induced by elliptic flow itself, which turns out to be exactly $\frac{1}{2}(v_2)^2$. The latter contribution becomes dominant as p_T increases.

Therefore, it is interesting to check the NCQ scaling of higher harmonic v_4. Figure 5.15 shows the v_4/n_q^2 of K_S^0 and Λ as a function of p_T/n_q for centrality $0-80\%$ in Au + Au collisions at $\sqrt{s_{NN}} = 200$ GeV from the TPC event plane method. It is clear to see that after divided by n_q^2, v_4 for K_S^0 and Λ coincide with each other very well until 1.5 GeV/c. It confirms that v_4 behaves like v_2^2 when $p_T > 1$ GeV/c as in hydrodynamic calculation.

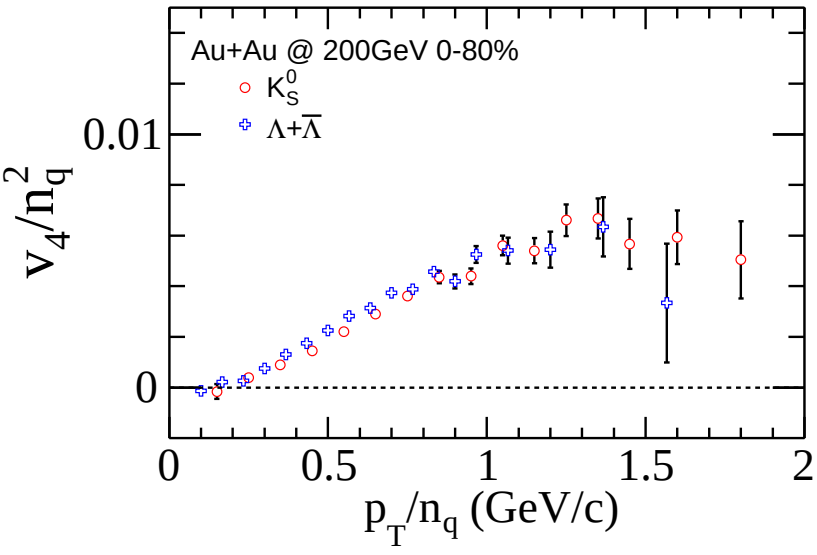

Figure 5.15: v_4/n_q^2 of K_S^0 and $\Lambda + \bar{\Lambda}$ as a function of p_T/n_q for centrality $0-80\%$ in Au + Au collisions at $\sqrt{s_{NN}} = 200$ GeV from the TPC event plane method.

5.3 Comparison with ideal hydrodynamic

In ideal hydrodynamic calculation as shown in Eq. 5.3, the ratio v_4/v_2^2 is expected to reach 0.5 when p_T increases. Therefore, it is important to check whether the ratio v_4/v_2^2 of data to see whether our system behaves like ideal hydro.

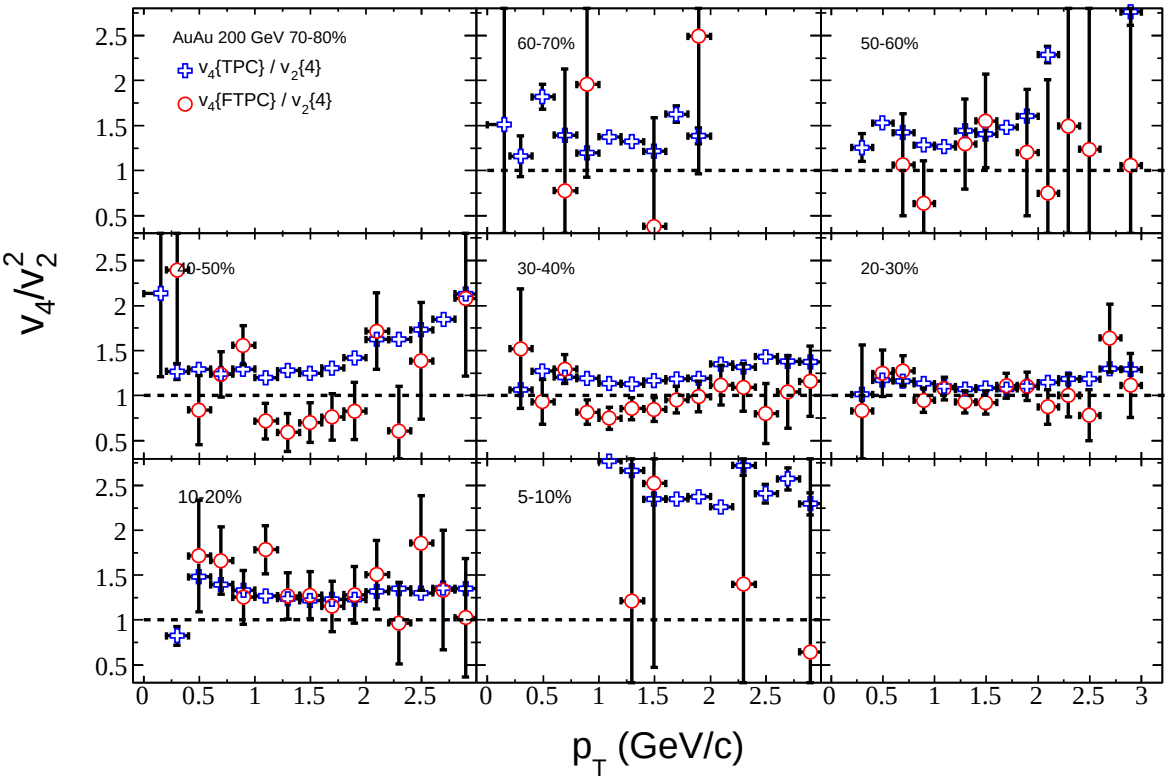

Figure 5.16: Charged particle v_4/v_2^2 as a function of p_T for centrality $70-80\%$, $60-70\%$, $50-60\%$, $40-50\%$, $30-40\%$, $20-30\%$, $10-20\%$, $5-10\%$ and $0-5\%$ in Au + Au collisions at $\sqrt{s_{NN}} = 200$ GeV. v_2 is from 4-particle cumulant method while v_4 is from TPC event plane (crosses) and FTPC event plane (circles).

Figure 5.16 shows charged particle v_4/v_2^2 as a function of transverse momentum (p_T) for centrality $70-80\%$, $60-70\%$, $50-60\%$, $40-50\%$, $30-40\%$, $20-30\%$, $10-20\%$, $5-10\%$ and $0-5\%$ in Au + Au collisions at $\sqrt{s_{NN}} = 200$ GeV. The ratio v_4/v_2^2 is very sensitive to the non-flow effect. As mentioned previously, the non-flow effect contributes to the estimation of bot v_2 and v_4. Since $v_2\{4\}$ is not sensitive to the non-flow effect, we use $v_2\{4\}$ as the denominator of v_4/v_2^2. Then the main non-flow effect contributing to the measurement v_4/v_2^2 is from v_4. It is clear that the non-flow effect would enhance the value of v_4 and also v_4/v_2^2. Here v_4 is measured from both TPC event plane (crosses) and FTPC event plane (circles). From the plot we can see that the ratio $v_4\{\text{TPC}\}/v_2^2$ is around 1 or larger for all the centralities. $v_4\{\text{FTPC}\}/v_2^2$ is a little smaller than $v_4\{\text{TPC}\}/v_2^2$, however, it is still larger than the ideal hydro predictions. One of the explanation is that interactions among the produced particles are not strong enough to produce local thermal equilibrium, so that the hydrodynamic description breaks down, the resulting value of v_4/v_2^2 is higher [Bor06a]. It is also argued that elliptic flow fluctuations may enhance the value of v_4/v_2^2 [Cle09a].

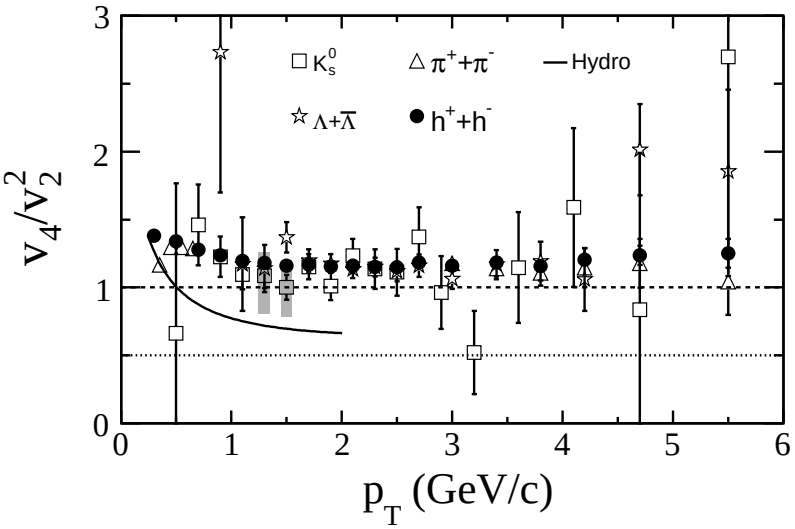

Figure 5.17: v_4/v_2^2 of $\pi^{\pm}$, p ($\bar{p}$), K_S^0 and $\Lambda(\bar{\Lambda})$ with TPC event plane as a function of transverse momentum for centrality $0-80\%$ in Au + Au collisions at $\sqrt{s_{NN}} = 200$ GeV. The solid curve is from hydro calculation [Bor06a].

The effects of v_2 fluctuations on the value of v_4/v_2^2 can be estimated as follow. The

v_2 from two-particle correlations is denoted by $v_2\{2\}$ and defined by $v_2\{2\} \equiv \langle\cos(2\phi_1 - 2\phi_2)\rangle$. If v_2 fluctuates within the sample of events, $\langle\cos(2\phi_1 - 2\phi_2)\rangle = \langle(v_2)^2\rangle$. Similarly, if v_4 and v_2 fluctuate, $\langle\cos(4\phi_1 - 2\phi_2 - 2\phi_3)\rangle = \langle v_4(v_2)^2\rangle$. We thus obtain

$$\frac{v_4\{3\}}{v_2\{2\}^2} = \frac{\langle v_4(v_2)^2\rangle}{\langle(v_2)^2\rangle^2} = \frac{1}{2}\frac{\langle(v_2)^4\rangle}{\langle(v_2)^2\rangle^2} \tag{5.4}$$

where, in the last equality, we have assumed that the prediction of hydrodynamics, $v_4 = (v_2)^2/2$ holds for a given value of v_2. If v_2 fluctuates, $\langle(v_2)^4\rangle > \langle(v_2)^2\rangle^2$, which shows that elliptic flow fluctuations increase the observed v_4/v_2^2.

If particle i is correlated with particle j by non-flow and correlated with particle k by flow, the 3-particle non-flow correlations can be written like:

$$g_2 \times \langle\cos(2\phi_i = 2\phi_k)\rangle = g_2 \times v_2\{4\}(p_T)v_2, \tag{5.5}$$

where g_2 is the non-flow effect from 2-particle correlations, and the average is taken over all the particles and events. Since it is observed that $g_2 \propto v_2^2\{2\}(p_T) - v_2^2\{4\}(p_T)$ [Adl02a, Bor02a], the non-flow contribution to $v_4(p_T)$ is obtained by:

$$\frac{g_2 \times v_2\{4\}(p_T)v_2}{v_2^2} = \frac{(v_2^2\{2\}(p_T) - v_2^2\{4\}(p_T)) \times v_2\{4\}(p_T)}{v_2}, \tag{5.6}$$

and the non-flow contribution to v_4/v_2^2 is then estimated by:

$$\frac{(v_2^2\{2\}(p_T) - v_2^2\{4\}(p_T))}{v_2 v_2\{4\}(p_T)}. \tag{5.7}$$

Figure 5.17 shows v_4/v_2^2 of charged hadron, $\pi^{\pm}$, p ($\bar{p}$), K_S^0 and $\Lambda(\bar{\Lambda})$ as a function of transverse momentum for centrality $0-80\%$ in Au + Au collisions at $\sqrt{s_{NN}} = 200$ GeV. Both v_2 and v_4 are from TPC event plane. The ideal hydrodynamic calculation [Bor06a] is shown as the black curve. The shaded band is the systematic uncertainty of charged hadron, the non-flow effect is calculated by Eq. 5.7. The values of v_4/v_2^2 for charged hadron and identified particles are close to unity when p_T is larger than 1 GeV/c, no obvious particle type dependence is observed. It means that even take the flow fluctuations into account, the value of v_4/v_2^2 of our data is still larger than ideal hydrodynamic prediction.

5.4 Summary

We analyze 60,000,000 minimum bias events from Au + Au collisions at $\sqrt{s_{NN}} = 200$ GeV collected from STAR experiment during RHIC Run VII. The two largest anisotropic flow coefficients, elliptic flow v_2 and the forth harmonic v_4 are measured for charged particles as well as charged pions, (anti)protons, K^0_S and Λ ($\bar{\Lambda}$). The flow coefficients are studied as function of transverse momentum, transverse energy and centrality. The main systematic uncertainty comes from so-called non-flow contributions and from the unknown fluctuations in the observables. Therefore, the TPC event plane method, FTPC event plane method and four-particle cumulant method are applied to study the anisotropic flow coefficients and estimate the systematic uncertainty based on the differences between the methods.

Elliptic flow v_2

Elliptic flow for charged particles is shown up to 15 GeV/c for different centralities using the TPC event plane method ($v_2\{\text{TPC}\}$), FTPC event plane method ($v_2\{\text{FTPC}\}$) and the four-particle cumulant method ($v_2\{4\}$) in this thesis. v_2 firstly increases with p_T, and then reaches its peak value at about 2 GeV/c. As p_T continues increasing, v_2 decreases significantly, and non-flow effect plays an important role in this region. $v_2\{4\}$ gives the low boundary of v_2. The sizable v_2 has been observed up to $p_T = 10$ GeV/c, which is consistent with the scenario of parton energy loss, and it is also the evidence for the formation of very dense matter.

Elliptic flow of identified particles (π, p ($\bar{p}$), K^0_S, Λ ($\bar{\Lambda}$)) are measured up to 6 GeV/c using both the TPC event plane and the FTPC event plane. At $p_T < 2$ GeV/c region, the mass ordering is observed as shown by previous studies. We find a deviation from the exact Number of Constituent Quark Scaling (NCQ) of pions compared to baryons by approximately 20% from 0.5 up to $p_T/n_q \simeq 1.5$ GeV/c, while models with realistic effects included can only explain a deviation up to 5% from a meson-baryon difference. The deviation from NCQ scaling between kaons and baryons are less prominent and less than 10%. The Coalescence models require a significant fragmentation contribution to

account for the large deviation from scaling at the upper end of the measured p_T/n_q and $(m_T - m)/n_q$ range. This suggests that fragmentation may kick in and becomes more dominant in this region.

The fourth harmonic v_4

Since v_4 signal is relatively small, we use the 2^{nd} harmonic reconstructed event plane. v_4 for charged particles is shown up to 7 GeV/c for different centralities using the TPC event plane method and FTPC event plane method, and v_4 for K^0_S and Λ ($\bar{\Lambda}$) is shown up to 7 GeV/c using the TPC event plane method. v_4 first increases with p_T at low p_T range and then becomes saturate at intermediate p_T. v_4 for K^0_S is larger than for Λ ($\bar{\Lambda}$) at low p_T while smaller at intermediate p_T, this behavior is similar to the behavior observed for identified particle v_2.

The ratio v_4/v_2^2 is proposed as a probe of ideal hydrodynamic behavior, and it is directly related to the degree of thermalization. The measured ratio v_4/v_2^2 as a function of p_T is studied for both charged particle and identified particles. It is found that the ratio v_4/v_2^2 is about 1 when p_T is about 2 GeV/c for all the particles, which is larger than the ideal hydrodynamic prediction. This may be due to the fluctuation of the measured v_2 and v_4, but also may indicate the incomplete thermalization of the system.

CHAPTER 6

Results II: Longitudinal property of Charge Balance Function

In this chapter, we present the results of charge balance function in π^+p and K^+p collisions from NA22 experiments and Au+Au collisions from STAR experiments. The dependencies on (pseudo)rapidity windows, transverse momentum, colliding energy and system size are studied. The longitudinal property and the width of charge balance function are also investigated with Monte Carlo models.

6.1 Boost invariance of charge balance function

Conventionally, boost invariance refers to single particle density being independent of rapidity as originally assumed in [Fey69a]. It has been applied in hydrodynamic model [Coo74a, Bjo83a] to simplify the equation of state. In heavy ion collisions, there is a plateau of the single particle density distribution in mid-rapidity which can satisfy the requirement of the assumption. However, the boost invariance of the balance function only requires that the charge correlation between final state particles be the same in any longitudinally-Lorentz-transformed frame. Therefore, it is interesting to check the longitudinal property of BF in whole phase space.

6.1.1 Hadron-hadron collisions

We first study the boost invariance of the charge balance function in π^+p and K^+p data at 250 GeV/c ($\sqrt{s_{NN}}$ =22 GeV) of the NA22 experiment. The experiment was equipped

with a rapid cycling bubble chamber as an active vertex detector, and it covered full momentum and 4π azimuthal acceptance. The latter feature allows us to study the properties of the balance function in full phase space for the first time.

Two data samples, π^+ and K^+, are combined in the analysis because no statistically significant differences are seen between the results. A total of 44,524 non-single-diffractive events are used after all necessary selections, i.e., the tracks reconstruction, exclusion of elastic and single-diffractive events. All the detail about data can be found in [Ada86a, Ata01a]. In particular, possible contamination from secondary interactions is suppressed by a double visual scan with 99.5% efficiency and the requirement that overall charge balance be satisfied within the whole event; γ conversions near the primary vertex are removed by electron identification.

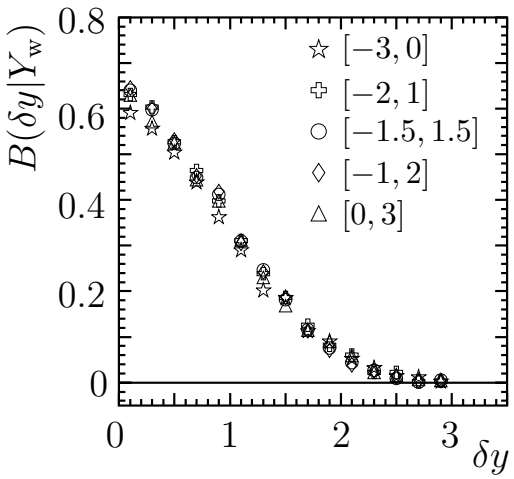

Figure 6.1: The balance function in five different positions of a rapidity window of size $Y_w = 3$.

In Figure 6.1, the BF is shown in five rapidity windows with width $Y_w = 3$, located at different positions, $[-3,0]$, $[-2,1]$, $[-1.5,1.5]$, $[-1,2]$, and $[0,3]$. Here the errors are statistical only and some of them are smaller than the size of the symbols. It is clear that the five functions coincide with each other within the errors, except a few points in $[-3,0]$ are a little lower than in other rapidity windows. This is caused by the very low multiplicity in the rapidity region $[-3,-2]$, where unidentified protons contribute and the rapidity distribution is not completely symmetric to the rapidity region $[+2,+3]$. From the plot we can conclude that, despite a strong rapidity dependence of the particle density as shown in Figure 6.2, the balance function is independent of the position of the

rapidity window, i.e., the charge correlation described by balance function is essentially the same in any longitudinally-Lorentz-transformed frame.

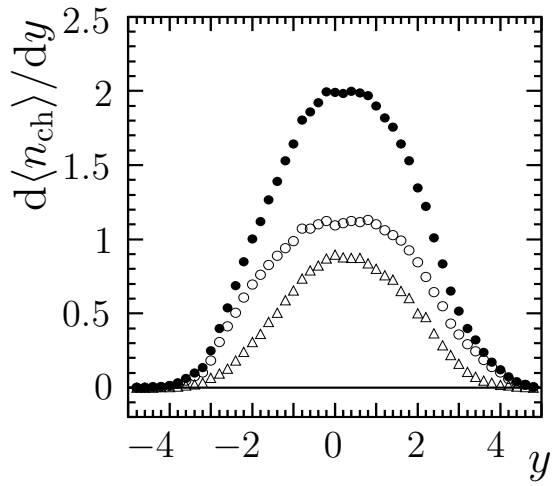

Figure 6.2: The rapidity distributions of positively (open circles), negatively (open triangles), and all (solid circles) charged particles.

Since we found that BF is boost invariant over the whole rapidity region, it is interesting to see if the BF in a limited rapidity window can be deduced from that in the full phase space by Eq. 2.11, and vice versa. In Figure 6.3, the balance function, $B(\delta y|Y_{\mathrm{w}})$ (solid points) in four rapidity windows (central in Fig. 6.3a, non-central in Fig. 6.3b), are compared with $B(\delta y|\infty)(1-\frac{\delta y}{Y_{\mathrm{w}}})$ (open points) obtained from the corresponding window of the BF in the whole rapidity region. The result means that the relation Eq. 2.11 does approximately hold in hadron-hadron collisions, and it is independently of size or position of the window. It further illustrates that the BF becomes narrower with decreasing Y_{w}, and this is in agreement with Eq. 2.11.

6.1.2 Nucleus-nucleus collisions

Since the boost invariance property of balance function has been observed in hadron-hadron collisions, it is also interested to check such property in heavy ion collisions. Here we analyze about 25 M mini-bias events in Au + Au collisions from STAR during RHIC Run IV.

Figure 6.4(a) displays the distributions of BF obtained from five different pseudora-

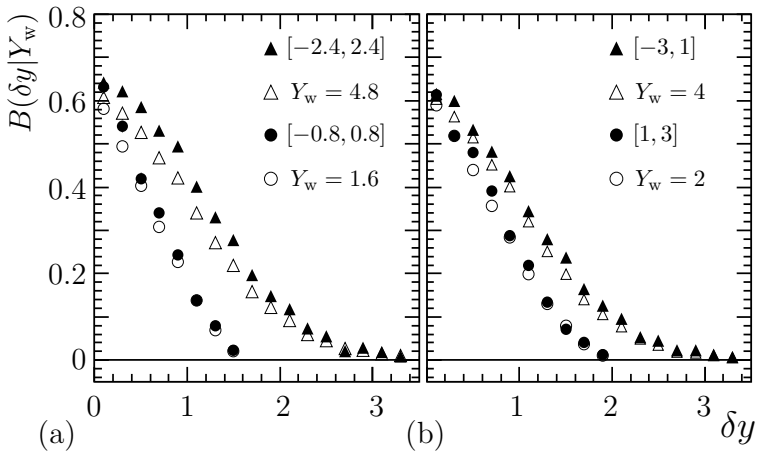

Figure 6.3: The balance functions $B(\delta y|Y_{\rm w})$ (solid symbols) (a) for two central rapidity windows, $[-2.4, 2.4]$ and $[-0.8, 0.8]$ and (b) two asymmetric rapidity windows $[-3, 1]$, and $[1, 3]$, compared with the corresponding $B(\delta y|\infty) \cdot (1 - \frac{\delta y}{Y_{\rm w}})$ (open symbols).

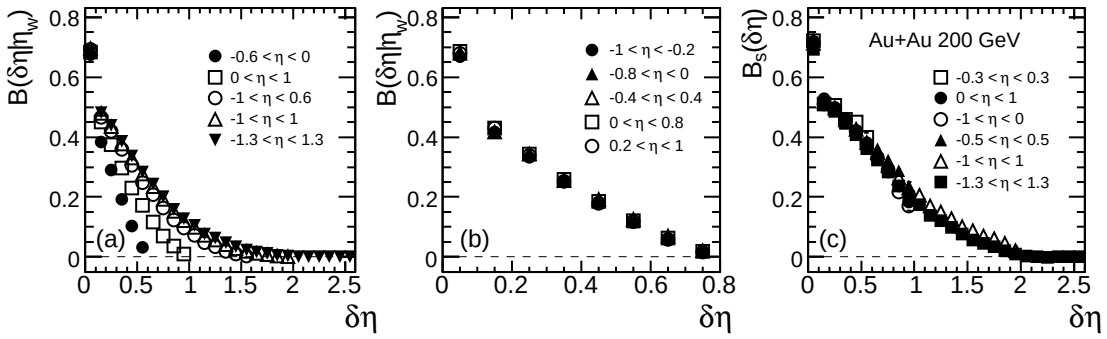

Figure 6.4: (a) Balance functions in five pseudorapidity windows of different width; (b) Balance functions observed at five different positions of pseudorapidity windows with $|\eta_{\rm w}| = 0.8$; (c) Scaled balance function, $B_s(\delta\eta)$, obtained for various pseudorapidity window widths and positions. Where $0 - 80\%$ centrality are selected and particle p_T range is $0.15 < p_T < 2$ GeV/c for Au + Au collisions at 200GeV. Statistical errors are smaller than the symbol sizes. Systematic errors are of the order of 5%.

pidity windows, located at various positions, and with sizes ranging from $|\eta_{\rm w}| = 0.6$ to 2.6. The BF strongly depends on the width of the pseudorapidity window. The error are statistical only. The systematic uncertainty is about 5%, coming from the uncertainties in the track reconstruction efficiency associated with the track cuts and the vertex position.

In order to directly test the boost-invariant of BF within the STAR TPC, five BFs are measured in equal size ($|\eta_{\rm w}| = 0.8$) pseudorapidity windows located at different positions as shown in Fig. 6.4(b). We find that the five BFs overlap with each another, thereby indicating that the BF is independent of the position of the pseudorapidity window, i.e., $B(\delta\eta|\eta_{\rm w})$ is invariant under a longitudinal translation within the range $-1 < \eta < 1$. Note that the large BF values measured at $\delta\eta = 0.1$ arise in part from HBT and Coulomb effects [Jeo02a, Ada03c].

In Fig. 6.4(c), the scaled balance functions, B_s, are obtained from BFs measured with four distinct pseudorapidity window widths ($|\eta_{\rm w}|$ =0.6, 1, 2, 2.6) and six window as suggested in Eq. 2.11. It is found that the scaled balance functions have almost the same shape and magnitude within experimental errors. It means that B_s is independent of the size and position of the window $\eta_{\rm w}$ in the pseudorapidity range $-1 < \eta < 1$. A similar invariance property of B_s was observed in hadron-hadron collisions over the whole rapidity range [Ata06a].

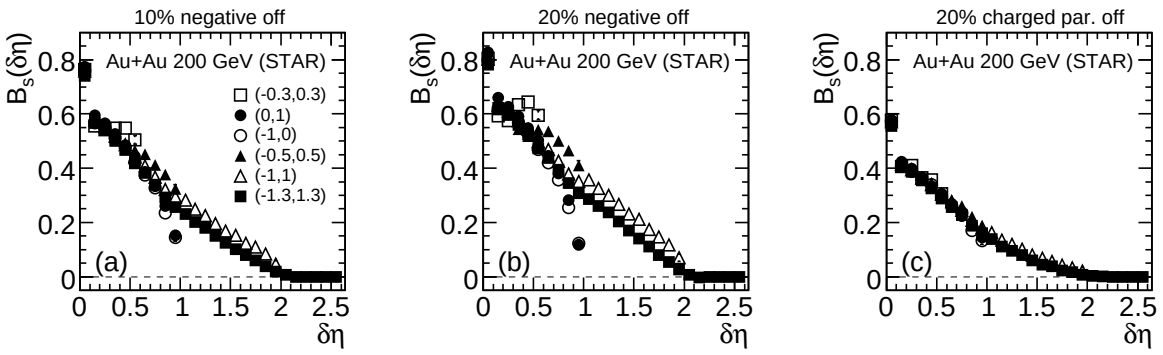

Figure 6.5: $B_s(\delta\eta)$ for three subsamples, in which (a) 10% negative, (b) 20% negative and (c) 20% charged particles are randomly thrown away, respectively..

This longitudinal property of BF is coming from the longitudinal interaction of

charged particles under the constraint of global electric charge balance. In order to check whether the global charge balance is a necessary condition for the observed longitudinal property of BF, two sub-samples are constructed by randomly throwing 10% and 20% negative particles respectively from each of the minimum bias events. Since the global net charge is out of balance in each event of these two samples, the longitudinal charge correlation in the whole phase space is uniformly changed. The scaled BF for these two samples are shown in Figure 6.5(a) and (b), respectively. We can see from the figure that the farther the charge is out of balance, the more seriously the longitudinal property of BF is violated. Therefore, the longitudinal property of balance function is sensitive to the global charge balance.

In addition, if both positive and negative particles are randomly thrown off from each events, e.g., 20% charged particles off as shown in Fig 6.5(c), the longitudinal property of BF holds. It is because that the global electric charge balance maintains more or less in each event. This is the same as data reconstruction. Therefore, the observed longitudinal property of BF also shows that the global charge conservation are well taken into account in the data reconstruction in STAR TPC.

6.1.3 Transverse momentum dependence

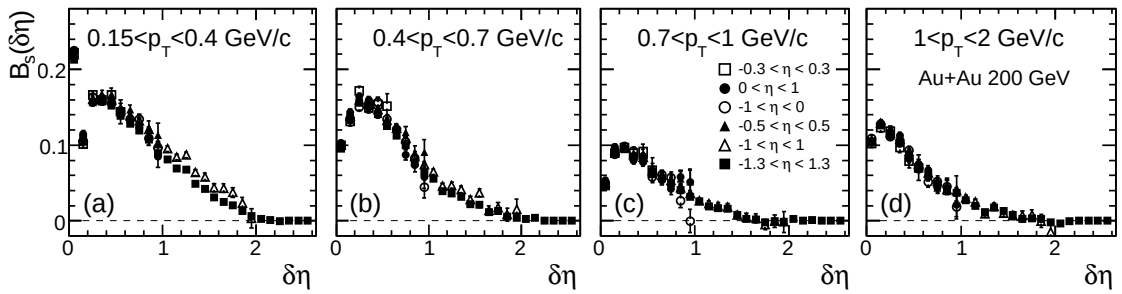

Figure 6.6: $B_s(\delta\eta)$ based on $B(\delta\eta|\eta_{\rm w})$ values measured in different pseudorapidity windows for particles in four p_T bins. Where $0-80\%$ centrality are selected and particle p_T range is $0.15 < p_T < 2$ GeV/c for Au+Au collisions at 200GeV. Error bars are statistical only. Systematic errors are of the order of 5%.

We also investigated the scaling property of the BF in different p_T ranges. Fig. 6.6

shows B_s distributions obtained for four p_T ranges: (0.15, 0.4), (0.4, 0.7), (0.7, 1) and (1, 2) GeV/c and the pseudorapidity windows is the same as used in Fig. 6.4(c). We can see that the scaled BFs in the same p_T bin but different positions of pseudorapidity window are consistent with each other very well. It means that such longitudinal boost invariance doesn't have p_T dependence. Comparing the distributions shown in Fig. 6.6(a) to Fig. 6.6(d), it is clear that the scaled balance function, $B_s(\delta\eta)$, changes significantly in shape and amplitude in different p_T range.

6.1.4 Centrality dependence

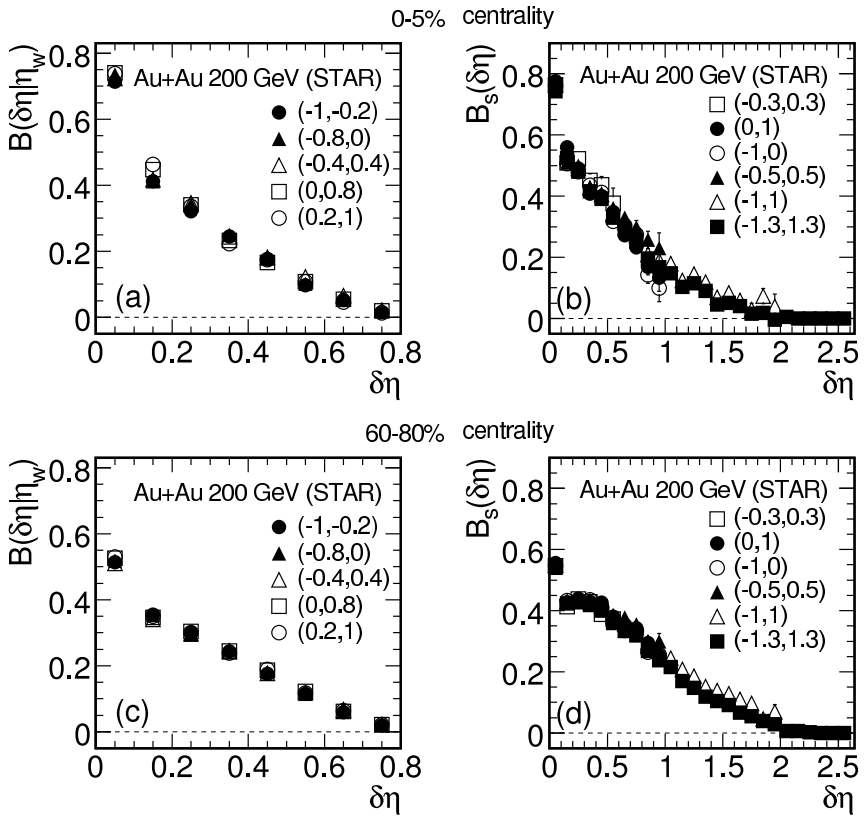

Figure 6.7: $B(\delta\eta|\eta_{\rm w})$ and scaled balance function, $B_s(\delta\eta)$, in central collisions $(0-5\%)$ and peripheral collisions $(60-80\%)$, respectively.

The centrality dependence of Balance Function is show in Figure 6.7. BFs with same width but different positions in (a) central collisions $(0-5\%)$ and (c) peripheral collisions are shown. We can see that BFs still overlap with each other in the same

centrality, although their shapes and widths have changed in different centralities. BFs in five pseudorapidity windows of different width in central collision $0-5\%$ is shown in Fig. 6.7(a). The scaled balance function, $B_s(\delta\eta)$, obtained from six pseudorapidity windows is shown in Fig. 6.7 for (b) central and (d) peripheral collisions. As shown in min-bias data in Fig. 6.4(c), the scaled balance functions are almost identical in the same centrality. It indicates that there is little centrality dependence for the charge compensate mechanism described by Balance Function.

6.1.5 Model investigation

The results from both hadron-hadron and nucleus-nucleus collisions indicate that charge balance of produced particles in strong interactions is boost-invariance in whole longitudinal phase space, without requiring the boost invariance of particle density. Therefore, it is interesting to check whether those properties are taken into account in the models which can describe hadron-hadron and nucleus-nucleus collisions, and more important, how they are associated with the mechanisms of particle production in the models.

In order to directly check whether the BF is invariant under a longitudinal Lorentz transformation over the whole rapidity range in hadron-hadron collisions, four equal size ($|\eta_{\rm w}| = 3$) pseudorapidity windows locating at different positions $(-3, 0)$, $(-2, 1)$, $(-1, 2)$ and $(0, 3)$ are chosen to measure the BF. The results for $p + p$ collisions at $\sqrt{s} = 22$ GeV and $\sqrt{s} = 200$ GeV are shown in Figure 6.8 (a) and (b) respectively. It shows that the BF measured in four windows are approximately the same at two incident energies. This indicates that the charge compensation is essentially the same in any longitudinally-Lorentz-transformed frame for $p + p$ collisions in the PYTHIA model which consistent with the data from NA22 experiment. The results demonstrate that the string fragmentation mechanism implemented in PYTHIA can well describe the production mechanisms of charge particles and their charge balance in longitudinal phase space.

Fig. 6.8 (c) and (d) are the scaled balance function $B_s(\delta\eta)$ at two incident energies. They are deduced from directly measured $B(\delta\eta|\eta_{\rm w})$ at six different pseudorapidity win-

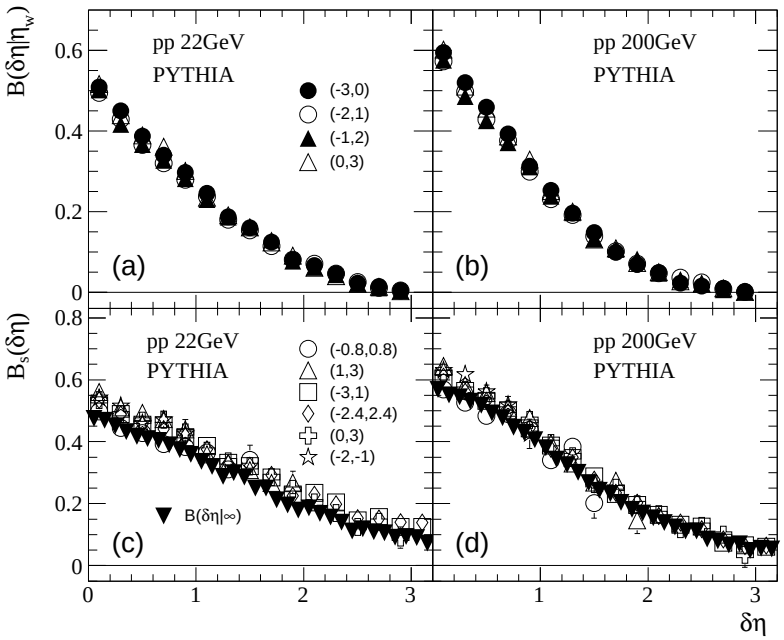

Figure 6.8: Upper panel: the $B(\delta\eta|\eta_{\rm w})$ in four pseudorapidity windows with equal size $|\eta_{\rm w}| = 3$ at the different positions for $p+p$ collisions at (a) $\sqrt{s} = 22$ GeV and (b) $\sqrt{s} = 200$ GeV by PYTHIA model. Lower panel: the scaled balance function, $B_s(\delta\eta)$, deduced from the directly measured BF at six different sizes and positions of pseudorapidity windows for $p+p$ collisions at (c) $\sqrt{s} = 22$ GeV and (d) $\sqrt{s} = 200$ GeV by PYTHIA model. The solid down triangle is the BF of the whole η range.

dows, $(-0.8, 0.8)$ (open circles), $(1, 3)$ (open triangles), $(-3, 1)$ (open squares), $(-2.4, 2.4)$ (open diamonds), $(0, 3)$ (open crosses), and $(-2, -1)$ (open stars). From the figures we can see that all the $B_s(\delta\eta)$ deduced from different windows overlap with each other within errors, as expected from boost-invariance of the BF [Jeo02a]. The solid down triangles in the same figures are the BF of the whole pseudorapidity range, $B(\delta\eta|\eta_\infty)$. It is close to the scaled balance function $B_s(\delta\eta)$. The result indicates that the scaled BF is corresponding to the BF of the whole pseudorapidity range $B(\delta\eta|\infty)$ [Jeo02a].

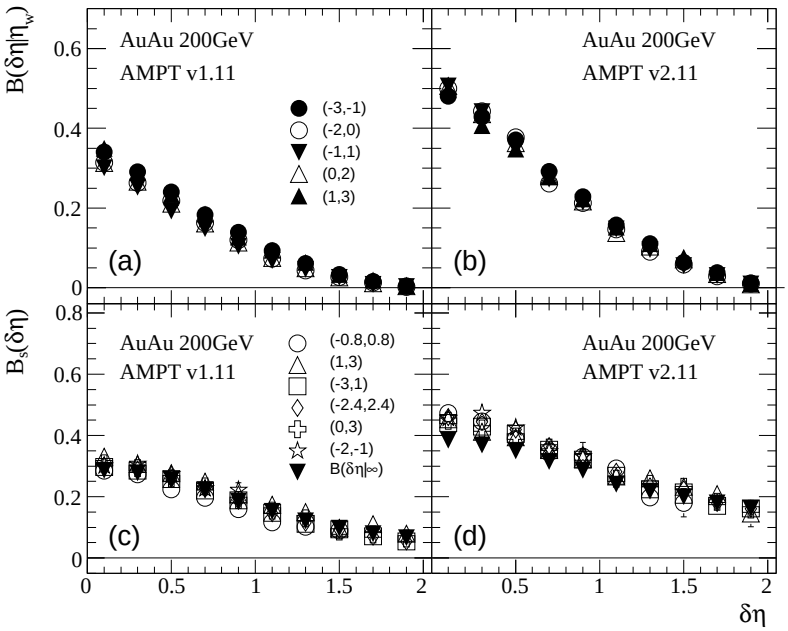

Figure 6.9: Upper panel: the $B(\delta\eta|\eta_{\rm w})$ in five pseudorapidity windows with equal size $|\eta_{\rm w}| = 2$ at the different positions for Au+Au collisions at $\sqrt{s} = 200$ GeV by (a) the AMPT default and (b) the AMPT with string melting. Lower panel: the scaled balance function, $B_s(\delta\eta)$, deduced from the directly measured BF at various pseudorapidity windows with different sizes and positions for Au+Au collisions at $\sqrt{s} = 200$ GeV by (c) the AMPT default and (d) the AMPT with sting melting.

It is then interesting to see whether the boost-invariance of the BF is held in nucleus-nucleus collisions. The boost-invariance of BF observed from STAR experiment is in central pseudorapidity range $-1 < \eta < 1$ [Zhi07a], where the single particle distribution is almost flat, or boost-invariance. Now with model investigation, we can carefully examine the property in the whole pseudorapidity range.

The upper panel of Figure 6.9 is the BF in five pseudorapidity windows with equal size $\eta_{\rm w} = 2$ at different positions $(-3,-1)$, $(-2,0)$, $(-1,1)$, $(0,2)$ and $(1,3)$. Where the Fig. 6.9 (a) and (b) are the results from the AMPT default (v1.11) and the AMPT with string melting (v2.11), respectively. Both figures show that the BF is boost-invariance in pseudorapidity range (-3, 3) in two versions of the AMPT.

The lower panel of Fig. 6.9 is the scaled balance functions obtained from directly measured BF at six different windows as indicated at legend of the figure, while the solid down triangles are the BF in pseudorapidity range (-4, 4). It shows that, in two versions of the AMPT models, the scaled BF does not depend on the size and position of the observed windows, and correspond to the BF of the whole pseudorapidity. This is consistent with the results of $p + p$ collisions in the PYTHIA model.

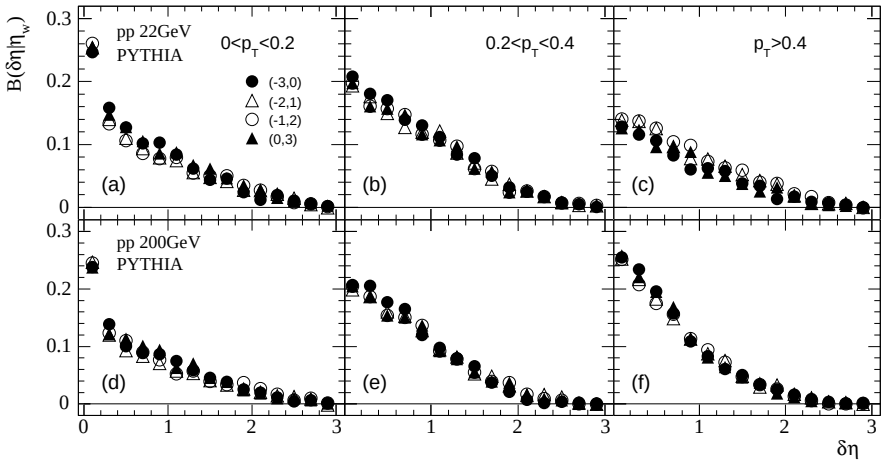

Figure 6.10: For each of three p_T ranges, the $B(\delta\eta|\eta_{\rm w})$ in four pseudorapidity windows with equal size $|\eta_{\rm w}| = 3$ at the different positions for $p+p$ collisions at $\sqrt{s} = 22$ GeV and $\sqrt{s} = 200$ GeV in upper and lower panels, respectively.

The longitudinal property of boost invariance of BF is coming from the special longitudinal interaction of charged particles under the constraint of global electric charge balance. Global electric charge conservation not only applies to all final state charged particles, but also constrains their production time during the evolution of the system. The transverse momentum of final state particles is considered to be roughly used as a scale of the proper time of particle production in the expansion of nuclear collisions [Hwa00a, Asa08a, Ham95a, Sin02a]. Study the p_T dependence of longitudinal

property of the BF may provide the direct access on checking whether particles in specified p_T range are consistent to be produced simultaneously with well balanced electric charge.

Figure 6.10 shows the BF for $p + p$ collisions at $\sqrt{s} = 22$ GeV and $\sqrt{s} = 200$ GeV from PYTHIA in three transverse momentum bins $(0 < p_T < 0.2)$, $(0.2 < p_T < 0.4)$, and $(p_T > 0.2)$ GeV/c, respectively. These p_T bins are selected to make the multiplicity in each bin comparable. It is clear that the points at a given $\delta\eta$ in a restricted p_T interval are approximately overlap with each other, i.e., the boost-invariance of the BF hold in small p_T ranges. This indicates that particles produced at different p_T ranges are also boost-invariant for hadron-hadron collisions in the PYTHIA model.

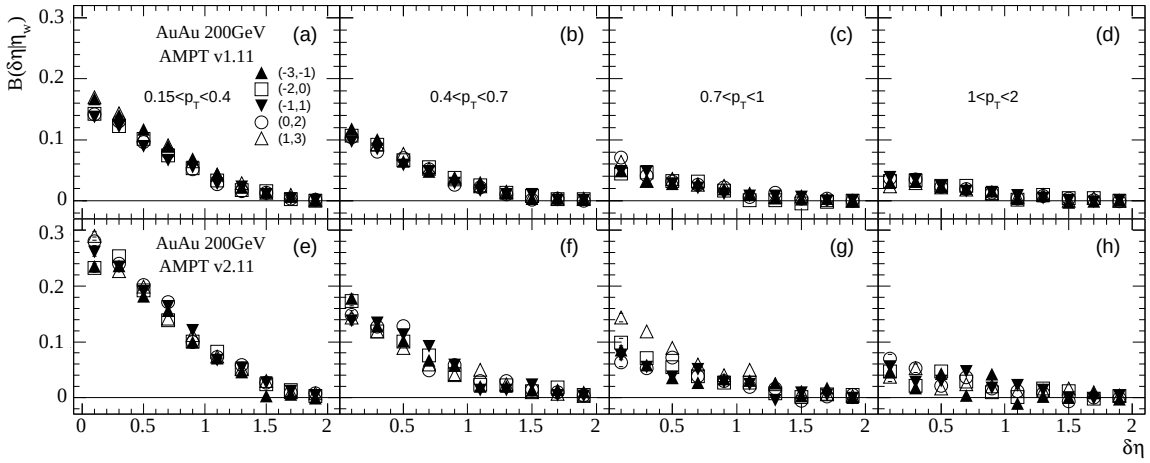

Figure 6.11: For each of four p_T ranges, the $B(\delta\eta|\eta_{\rm w})$ in five pseudorapidity windows with equal size $|\eta_{\rm w}| = 2$ at the different positions for Au+Au collisions at $\sqrt{s} = 200$ GeV from the AMPT default (in upper panel) and the AMPT with string melting (in lower panel).

The same study for Au + Au 200 GeV collisions from the two versions of the AMPT are presented in the upper and lower panels of Figure 6.11, respectively. We choose four p_T bins, $(0.15, 0.4)$, $(0.4, 0.7)$, $(0.7, 1)$ and $(1, 2)$ GeV/c. From the upper panel of the figure, we can see that the BF of different pseudorapidity windows in each p_T bin are close to each other, which is consistent with the data from STAR experiment [Zhi07a]. However, in the AMPT with string melting, as shown in the lower panel of the figure, the BF of different pseudorapidity windows does not coincide with each other very well.

The reason is that in the AMPT with string melting version, in the evolution of

nuclear collisions, each parton has its own freeze-out time, which may last a very long period after the interaction of two nucleus [Mei06a]. The particles in the same transverse momentum range are not freezed-out simultaneously with well balanced charge, and thus the longitudinal boost invariance of the BF in small p_T ranges is broken. While in the AMPT default version, the partons recombined with their parent strings immediately after they stop interacting, and converted to hadrons. Therefore, the charge balance of the produced particles in the same p_T ranges is preserved and boost-invariance of the BF keeps.

6.2 The width of charge balance function and delay hadronization

The width of charge balance function is considered at a probe of QGP for clocking hadronization [Bas00b], however, the BF itself has multiplicity dependence. Thus, it is important to study the multiplicity dependence of BF to understand experimental result.

6.2.1 Multiplicity dependence

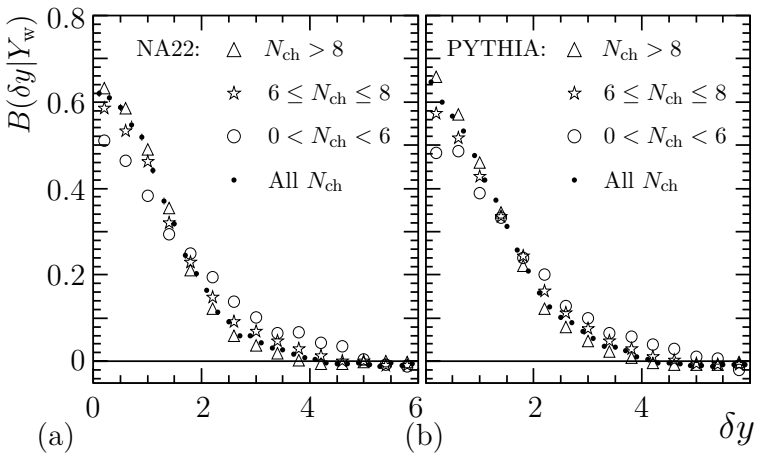

Figure 6.12: The balance function for all charged particles and for three multiplicity intervals from NA22 and PYTHIA.

In Figure 6.12(a), the full-rapidity balance function in three multiplicity intervals is

Table 6.1: The width of the BF in three multiplicity intervals and for all charged particles.

Multiplicity	$\langle\delta y\rangle_{\mathrm{NA22}}$	$\langle\delta y\rangle_{\mathrm{PYTHIA}}$
$n_{ch} > 8$	0.957 ± 0.011	0.755± 0.010
$6 \leq n_{ch} \leq 8$	1.096 ± 0.014	0.929±0.011
$0 < n_{ch} < 6$	1.359 ± 0.026	1.159±0.023
all n_{ch}	0.991 ± 0.008	0.816±0.007

compared in π^+p and K^+p data at $\sqrt{s_{NN}}$ =22 GeV from the NA22 experiment. The widths of the BFs for the corresponding multiplicity intervals are listed in Table I. The width decreases with increasing multiplicity, which is qualitatively consistent with the narrowing of the BF with increasing centrality observed in current heavy ion experiments [Ada03c, Alt05a]. The corresponding results from PYTHIA 5.720 [Sjo94a] are given in Figure 6.12(b) and Table 6.1. The hadronization scheme with string fragmentation implemented in PYTHIA qualitatively reproduces the trend of the data. Therefore, before interpreting the narrowing of the balance function with increasing centrality and increasing number of the colliding nuclei as a probe of delayed hadronization, which is connected to the possible formation of a QGP, the multiplicity effect observed here, which has nothing to do with the formation of a new state of matter, should be properly taken into account. This will relax the apparent contradiction between the narrowing of BF and the charge fluctuation measurement in current heavy ion experiments.

6.2.2 Energy Dependence

From the previous experimental studies, we know that the BF also becomes narrower as the increasing of multiplicity in hadron-hadron collisions at $\sqrt{s_{NN}}$ = 22 GeV [Ata06a]. It is important to see the how significant the multiplicity dependence is. Here, we study the width of BF in $p + p$ collisions from PYTHIA Monte-Carlo generator at four energy at $\sqrt{s_{NN}}$ = 22, 64, 130 and 200 GeV with full rapidity space.

It can be seen from the Figure. 6.13 that for $p + p$ collision, where no quark-parton

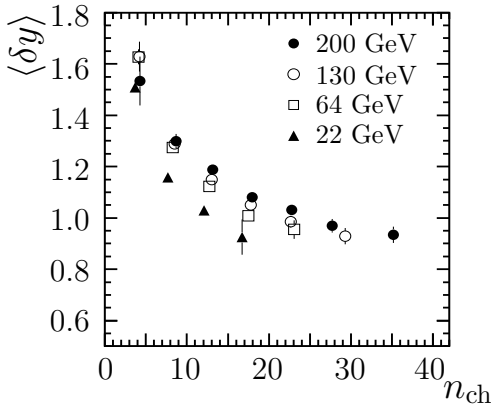

Figure 6.13: The width of full-phase-space balance function for different multiplicity in $p+p$ collisions at $\sqrt{s_{NN}}$ = 22, 64, 130 and 200 GeV.

phase is expected, the width of BF decreases with the increase of multiplicity, i.e., the width of BF is narrower for larger multiplicity. It is expected that the hadronization in hadron-hadron collisions is almost instantaneous, thus this effect has nothing to do with hadronization time. Also, the width of BF depends on collision energy. For the same multiplicity, the higher the collision energy is, the wider the width of balance function.

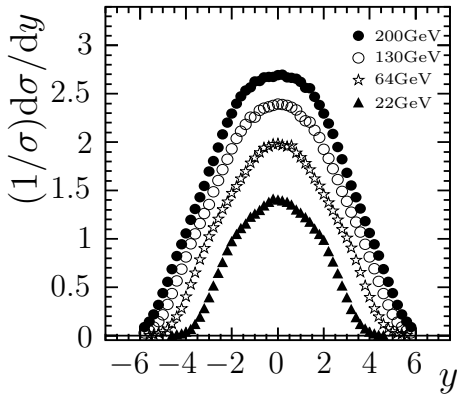

Figure 6.14: The rapidity distribution of all charged particles in $p+p$ collision at $\sqrt{s_{NN}}$ = 22, 64, 130, 200 GeV.

However, it also should be noticed that the BF is sensitive to the size of observed window [Ata06a], and the full rapidity region is wider for higher energy, as shown in Fig. 6.14. To remove the influence of the width of rapidity region, we choose a fixed-size observation window $-3 \leq y \leq 3$ to calculate the width of BF for all four energies. The results, presented in Fig. 6.15, show that when the (average) rapidity density dN/dy is

the same, the width of balance function is almost independent of energy, especially for high dN/dy. From the plot we can conclude that in hadron-hadron collisions, the width of BF becomes narrower as multiplicity increases when the multiplicity is small (about ≤ 20). And as the multiplicity continue increases, the width of BF gradually reaches its low limit. Also, the width of BF is independent of energy which is consistent with instantaneous hadronization in hadron-hadron collisions.

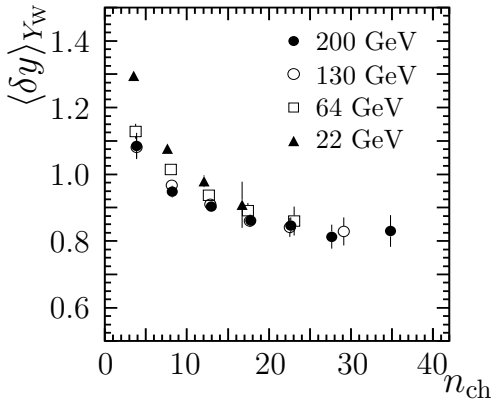

Figure 6.15: The width of balance function in the rapidity region $[-3, 3]$ for different multiplicity in $p + p$ collision at $\sqrt{s_{NN}} = 22$, 64, 130 and 200 GeV.

6.2.3 Transverse momentum and centrality dependencies

Balancing particle are separated in momentum space according to the thermal properties of the freezed-out stage of the system. As we know that the thermal velocities are determined by local temperature and particle mass, and they are related to transverse mass and transverse momentum for relativistic particles. Therefore, the BF is affected by transverse expansion (collective flow).

The widths of scaled $B_s(\delta\eta)$ are presented in Table 6.2 for Au + Au collisions at 200 GeV. The first data point in Fig. 6.6(a) is affected by HBT correlations, which result in a strong correlation at small relative p_T. On the other hand, track merging effects would deplete the balance function at small $\delta\eta$. To assess the systematic uncertainties on the extracted width, we use extrapolated values for the two lowest $\delta\eta$ data points instead of their measured ones in calculating the width. For the lower bound of systematic uncer-

Table 6.2: The widths $\langle\delta\eta\rangle$ of the $B_s(\delta\eta)$ for four p_T bins. The first and second errors are statistic and systematic, respectively.

p_T(GeV/c)	$\langle\delta\eta\rangle$
(0.15, 0.4)	$0.652 \pm 0.006^{+0.081}_{-0.029}$
(0.4, 0.7)	$0.609 \pm 0.008^{+0.049}_{-0.037}$
(0.7, 1)	$0.536 \pm 0.016^{+0.047}_{-0.041}$
(1, 2)	$0.487 \pm 0.014^{+0.079}_{-0.021}$

tainty estimate, the extrapolations from the larger $\delta\eta$ data are done by two functional forms. One is exponential for the p_T in (0.15, 0.4) and Gaussian for the other three p_T bins. For the upper bound of systematic uncertainty estimate, the extrapolated function is multinomial for all four p_T bins. Table 6.2 demonstrates that the width of the scaled BF becomes narrower for increasing p_T. This observation is qualitatively consistent with expectations from thermal models [Jeo02a].

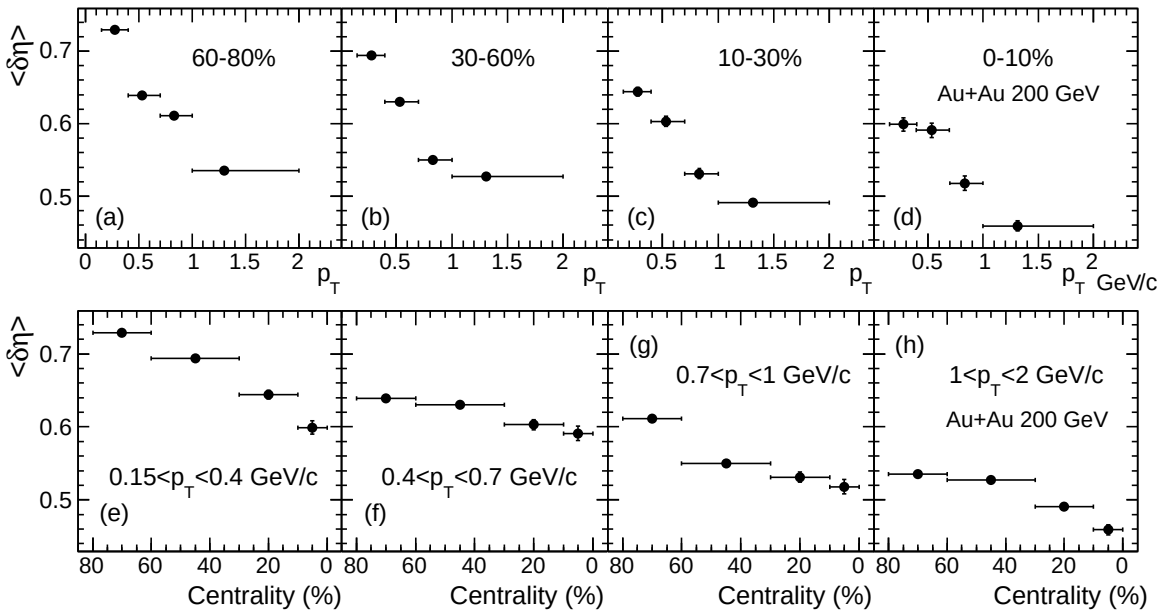

Figure 6.16: Upper panel: the p_T dependence of the width of the BF in different centrality bins; Lower panel: the centrality dependence of the width of the BF in different p_T intervals, for Au + Au collisions at 200 GeV.

As has been shown in [Ada03c], the width of the BF decreases with collision centrality. The decreases in the BF width with increasing p_T and increasing centrality could be

associated with transverse radial flow [Bas03a, Bas00b, Vol06b]. In order to disentangle these effects, we further study the p_T dependence of $\langle\delta\eta\rangle$ in different centrality bins. This is shown in the upper panel of Fig. 6.16. It shows clearly that the width of the BF decreases with the transverse momentum of final state particles in each centrality bin. We also study the centrality dependence of $\langle\delta\eta\rangle$ in different p_T intervals. This is presented in the lower panel of Fig. 6.6. It shows that the narrowing of the BF with increasing centrality is present in all p_T bins. Our results demonstrate that the BF becomes narrow with increasing p_T at all given centrality bins, and in more central collisions at all given p_T bins. The width of BF depends on both centrality and p_T. The origins of these narrowing and their possible connections should provide more insight into the particle production dynamics in relativistic heavy ion collisions.

6.3 The relation with charge correlation and fluctuation

Balance function measures the correlation of balancing charge, and it can be related to charge correlation and fluctuation.

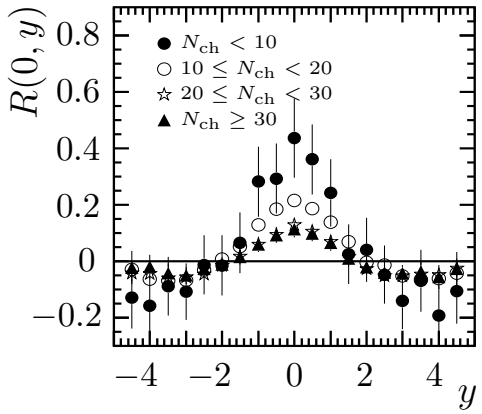

Figure 6.17: The 2-particle correlation function $R(0, y)$ as function of y for different multiplicities in $p + p$ collision at $\sqrt{s_{NN}} = 200$ GeV.

Charge balance function measures the correlation length between oppositely charged particles, and it can be related to standard two-particle correlation function [Foa75a].

For comparison we calculate the standard two-particle correlation function of oppositely charged particles

$$R^{+-}(y_1, y_2) = \frac{1}{2}[\frac{\rho^{(2)}(y_1^+, y_2^-)}{\rho^{(1)}(y_1^+)\rho^{(1)}(y_2^-)} + \frac{\rho^{(2)}(y_1^-, y_2^+)}{\rho^{(1)}(y_1^-)\rho^{(1)}(y_2^+)}] - 1 \tag{6.1}$$

for different multiplicities in $p + p$ collision at $\sqrt{s_{NN}} = 200$ GeV, for $y_1 = 0$, $y_2 = y$. The results plotted in Fig. 6.17 show that the width of R is consistent with being independent of multiplicity. A possible explanation of the width of R is cluster decay. Comparing with the definition of balance function, Eq. 2.9, the difference between the correlations of opposite- and like-charged particles shows a clear multiplicity dependence, which is unrelated with cluster decay and it is mainly due to the string fragmentation mechanism implemented in PYTHIA model.

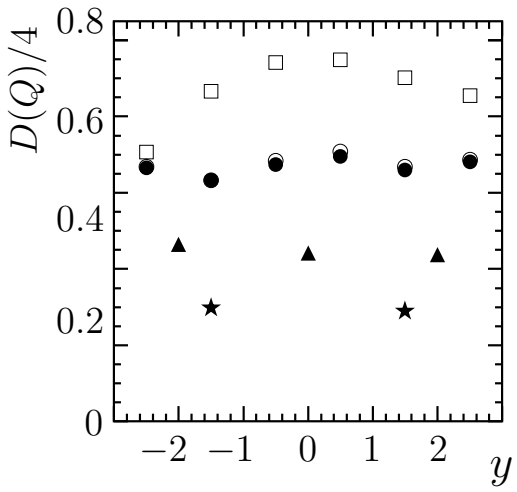

Figure 6.18: $D(Q)/4$ versus the position of a rapidity window of size $Y_{\rm w} = 1$ (circles), 2 (triangles), and 3 (stars). Open circles and open squares are, respectively, $D(Q)/4$ under the same transverse momentum and azimuthal angle cuts as used by STAR ($p_T > 0.1$ GeV/c) and PHENIX ($p_T > 0.2$ GeV/c and $\Delta\phi = \pi/2$).

Since the charge fluctuation $D(Q)$ defined in Eq. 2.12 is related to BF as Eq. 2.13, it is interesting to see how the charge fluctuation changes with position and size of a rapidity window. For this purpose, $D(Q)/4$ is presented in Figure 6.18 for different positions and sizes of a rapidity window. The results confirm that for the given window size the measured charge fluctuation is independent of the position of that window [Ata05a], in agreement with boost invariance of the BF. The data also show that the smaller the

rapidity window the larger the fluctuation. So it is necessary to give the exact size of the rapidity region when the fluctuation is treated quantitatively [Jeo00a, Asa02a].

As has been demonstrated in [Ata05a], $D(Q)$ also depends on the acceptance in transverse momentum and/or azimuthal angle. $D(Q)/4$ under the same cuts as used by STAR ($p_T > 0.1$ GeV/c) and PHENIX ($p_T > 0.2$ GeV/c and $\Delta\phi = \pi/2$) with $Y_{\rm w} = 1.0$ is presented in Figure 6.18 as open points. The cut used by STAR has little influence on the result, while those used by PHENIX destroy the boost invariance of $D(Q)$. These results show that a limited acceptance can destroy the boost invariance of charge fluctuations and the effect is the larger the larger the percentage of particles lost.

6.4 Summary

We study the longitudinal property of boost invariance for charge balance function (BF) in hadron-hadron and nucleus-nucleus collisions.

In π^+p and K^+p collisions from NA22/EHS at $\sqrt{s_{NN}} = 22$ GeV, in contrast with signal particle density distribution, the BF is found to be invariant under longitudinal boost over the whole rapidity range of produced particles ($-5 < y < 5$), i.e., the ratio of $B(\delta y|y_{\rm w})$ to $(1 - \delta y/|y_{\rm w}|)$ is independent of the observed window, $|y_w|$, and corresponds to the BF of the whole rapidity range. Such longitudinal property is also observed in Au + Au collisions from STAR/RHIC at $\sqrt{s_{NN}} = 200$ GeV within a relatively wide pseudorapidity coverage ($|\eta| < 1.3$). Furthermore, we find that this scaling property has little dependence on p_T and centrality. In order to compare with experimental data, we also systematically study the longitudinal boost invariance of the BF and its p_T dependence for p + p and Au + Au collisions using the PYTHIA and the AMPT Monte Carlo models. It shows that the BF is boost invariant in both hadron-hadron and nuclear interactions, in contrast to the single-particle density. As expected, this boost invariance of the BF results that the BF properly scaled by window size is independent of the window and corresponds to the BF of the whole pseudorapidity range.

Therefore, the BF can be considered as a good measurement which free from the re-

striction of finite longitudinal acceptance, i.e, the scaled BF, $B_s(\delta\eta)$, can be quantitively compared from different experiments with different pseudorapidity coverages. Since the BF measures how the conserved electric charge compensate in the phase space, the longitudinal property of boost invariance of BF means that production of charged particles are constrained by charge balance, and it is essentially the same in any longitudinally-Lorentz- transformed frame.

It is argued that the width of charge balance function, $< \Delta y >$ ($< \Delta\eta >$), can be considered as a probe of late hadronization, we measure it in both hadron-hadron and nucleus-nucleus collisions.

In π^+p and K^+p collisions from NA22/EHS at $\sqrt{s_{NN}} = 22$ GeV, where no QGP phase space is expected, $< \Delta y >$ is found to be narrower as multiplicity increasing. To investigate this trivial effect, we studied $< \Delta y >$ in $p + p$ collisions at $\sqrt{s_{NN}} = 22$, 64, 130, 200 GeV using PYTHIA Monte-Carlo generator. The result shows that the width of BF first decreases with increasing multiplicity, and it changes little when multiplicity is about larger than 20. When the same size of observation window ($Y_{\rm w}$) is used, the width of BF is independent of colliding energy, which is consistent with expectation of instantaneous hadronization in hadron-hadron collisions. Also, $< \Delta y >$ is found sensitive to the size of observed windows, and it is consistent with charge correlation and fluctuation. In Au + Au collisions from STAR/RHIC at $\sqrt{s_{NN}} = 200$ GeV, $< \Delta y >$ decreases with increasing transverse momentum and increasing centrality. The origin of these narrowings is associated with transverse radial flow and their possible connections should provide more insight into the particle production dynamics in relativistic heavy ion collisions.

CHAPTER 7

Outlook

7.0.1 Test thermalization

Hydrodynamics is expected to be a good description of the hot and dense matter created in heavy ion collisions. There are two main components in hydrodynamic flow: collectivity and (local) thermalization. The collectivity has already been observed in the experiments, thus, it is important to study the thermalization of colliding system for the next step.

Comparing the experimental results with hydrodynamic calculations can help us to understand the characters of the created medium. Unlike light quarks, heavy quark masses are not modified by the surrounding QCD medium and the value of their masses is much higher than the initial excitation of the system. Heavy quarks are expected to thermalize much more slowly than light partons, they are believed to be ideal probes to study the degree of the early thermalization of the medium created in heavy ion collisions. STAR has upgraded several detectors related to this analysis: Data Acquisition (DAQ1000), Time-Of-Flight (TOF), Heavy-Flavor Tracker (HFT) and High Level Trigger (HLT).

Data Acquisition

To improve the DAQ rate, STAR has upgraded the TPC readout and Data Acquisition electronics in 2009. The new system is so called "DAQ1000" with DAQ rate more than 1000 Hz. It significantly improves STAR's data taking capabilities by almost a factor of 10, thus almost eliminating the system dead time.

Time-Of-Flight

The barrel TOF detector has been completed in 2010. It surrounds the outer edge of the TPC, and cover $-1 < \eta < 1$ and 2π in azimuthal. It improves the STAR PID capability: π/K separation range can be extended from 0.7 GeV/c to 1.6 GeV/c and $p/(\pi, K)$ separation range can be extended from 1.1 GeV/c to $\sim$ 3 GeV/c. The TOF allows STAR to identify charged hadrons and electrons from low to high p_T when combined with TPC dE/dx and Electromagnetic Calorimeter (EMC). Without misidentification of charged particles, the signal/background ratio for reconstructed particles will increase, which means that the statistic will be significantly improved.

Heavy-Flavor Tracker

The Heavy-Flavor Tracker (HFT) is a high resolution Si pixel detector that will surround the interaction point at STAR and provide high resolution space points for forming tracks. It will enhance STAR's capability of directly reconstructing charmed and bottomed hadrons.

High Level Trigger

The HLT makes a trigger decision online by combining TPC tracks from fast online tracker with information collected from STAR調other subsystems. With the HLT, all the upgraded components will perform at their full potential far beyond STAR調current trigger abilities. HLT reduces the amount of data written to tape while still maintaining a high sampling rate to fully utilize the delivered luminosity, thus assures timely physics output of the interesting physical topics.

7.0.2 Beam energy scan

The first decade of RHIC running has established the existence of a strongly coupled Quark Gluon Plasma (sQGP), a new state of nuclear matter with partonic degrees of freedom is believed to be created at RHIC. The transition from QGP to hadronic gas

depends on both baryon chemical potential (μ_B) and temperature (T). The lattice QCD predicts that there is a critical point between the cross-over (low μ_B and high T) and 1st order transition (high μ_B and low T) when the transition happens. Experimentally we can vary these initial conditions by altering the beam energy.

To mapping the phase diagram, STAR is running a Beam Energy Scan (BES) program close to the QGP-hadron gas boundary in RHIC run 2010. Several analyses related to this analysis are listed to give a taste of the physics that will be revealed by a BES.

Critical point

At the critical point extreme long wavelength fluctuations in the susceptibilities of conserved quantities are expected to occur [Koc08a, Che08a]. A non-monotonic behavior of the event-by-event fluctuation is expected to be observed around the critical point, e.g., the moments of such variables as the particle ratios (e.g. K/π and p/π), net baryon number and net strangeness etc. Although some of these measurements have been attempted previously at the SPS, STAR調large acceptance allows us to measure such variables with increased sensitivity in each event, and making these measurements in the same detector gives improved control of the systematics as a function of collision energy.

1st order transition

Directed flow, v_1, is generated during the nuclear passage time, $T_{\rm pass}$, and can therefore probe the onset of bulk collective dynamics as long as the passage time, $T_{\rm pass} > \tau_0$. It is predicted that a "wiggle" should appear at mid-rapidity when passing through a first order phase transition [Bra00a, Sto05a].

"Turn-off" of sQGP signatures

The number of constituent quark (NCQ) scaling of elliptic flow is one of the strongest evidence of partonic degrees of freedom at RHIC top energy. Such scaling is only expected to hold if the energy density is sufficient to ensure a deconfined phase. Therefore, it is interesting to see whether this property will "turn-off" at lower energy where the energy

density drops below that required to produce a sQGP.

References

[Abe08a] B. I. Abelev et al. *Phys, Rev. C*, **77** 54901, 2008.

[Ack01a] K. H. Ackermann et al. *Phys. Rev. Lett.*, **86** 402, 2001.

[Ack03a] K. Ackermann et al. *Nucl. Instru. Methd A*, **499** 624, 2003.

[Ack03b] K. Ackermann et al. *Nucl. Instru. Methd A*, **499** 709, 2003.

[Ada03a] M. Adamczyk et al. *Nucl. Instru. Methd A*, **499** 437, 2003.

[Ada03c] J. Adams et al. *Phys. Rev. Lett*, **90** 172301, 2003.

[Ada05a] J. Adams et al. *Nucl. Phys. A*, **757** 102, 2005.

[Ada05b] J. Adams et al. *Phys. Rev. C*, **72** 014904, 2005.

[Ada06a] A. Adare et al. *nucl-ex/0608033*

[Ada07a] A. Adare et al. *Phy. Rev. Lett.*, **98** 162301, 2007.

[Ada86a] M. Adamus et al. Z. Phys, **C32** 475, 1986.

[Ata01a] M. R. Atayan et al. Eur. Phys. J, **C21** 271, 2001.

[Adc03a] K. Adcox et al. *Nucl. Instru. Methd A*, **499** 469, 2003.

[Adl02a] C. Adler et al. *Phys. Rev. C*, **66** 034904, 2002.

[Adl03b] S. S. Adler et al. *Phys. Rev. Lett.*, **91** 182301, 2003.

[All03a] C. E. Allgower et al. *Nucl. Instr. Method A*, **499** 740, 2003.

[Alt05a] C. Alt et al. *Phys. Rev. C*, **71** 034903, 2005.

[Alv07a] B. Alver et al. *Phys. Rev. Lett.*, **98** 242302, 2007.

[Ams08a] C. Amsler et al. *Phys. Lett. B*, **667** 1, 2008.

[And03a] M. Anderson et al. *Nucl. Instr. Method A*, **499** 659, 2003.

[Arn03a] L. Arnold et al. *Nucl. Instr. Method A*, **499** 652, 2003.

[Asa00a] M. Asakawa, U. Heinz, and B. Muller. *Phys. Rev. Lett.*, **85** 2072, 2000.

[Asa02a] M. Asakawa, V. Koch, M. Bleicher and S. Jeon. *Nucl. Phys. A*, **698** 261, 2002.

[Asa08a] M. Asakawa, S. A. Bass, B. Muller and C. Nonaka. *Phys. Rev. Lett.*, **101** 122302, 2008.

[Ata05a] M. R. Atayan et al. *Phys. Rev. D*, **71** 012002, 2005.

[Ata06a] M. R. Atayan, et al. *Phys. Lett. B*, **637** 39, 2006.

[Bac03a] B. B. Back et al. *Nucl. Instr. Methd A*, **499** 603, 2003.

[Bar97a] J. Barrette et al. *Phy. Rev. C*, **56** 3254, 1997.

[Bas99a] S. A. Bass, M. Gyulassy, H. Stöcker, W. Greiner. *J. Phys. G*, **25** R1, 1999.

[Bas00b] S. A. Bass, P. Danielewicz, S. Pratt. *Phys. Rev. Lett.*, **85** 2689, 2000.

[Bas03a] S. Pratt, S. Cheng. *Phys. Rev. C*, **68** 014907, 2003.

[Bed03a] M. Beddo et al. *Nucl. Instr. Methd A*, **499** 725, 2003.

[Bei03a] F. S. Beiser et al. *Nucl. Instr. Methd A*, **499** 762, 2003.

[Bel03a] R. Bellwied, et al. *Nucl. Instr. Method A*, **499** 636, 2003.

[Ben87a] H.U. Bengtsson and T. Sjöstrand. *Comp. Phys. Comm.*, **46** 43, 1987.

[Ber03a] F. Bergsma, et al. *Nucl. Instr. Method A*, **499** 629, 2003.

[Bet03a] S. Bethke. *Nucl. Phys. Proc. Suppl.*, **121** 74, 2003.

[Bha03a] R. S. Bhalerao, N. Borghini, J.-Y. Ollitrault. *Nucl. Phys. A*, **727** 373, 2003.

[Bha05a] R. S. Bhalerao, J. P. Blaizot, N. Borghini and J. Y. Ollitrault. *Phys. Lett. B*, **627** 49, 2005.

[Bjo83a] J. D. Bjorken. *Phys. Rev. D*, **27** 140, 1983.

[Bon03a] B. Bonner et al. *Nucl. Instru. Method A*, **508** 181, 2003.

[Bor01a] N. Borghini, P. M. Dinh, J.-Y. Ollitrault. *Phys. Rev. C*, **63** 054906, 2001.

[Bor02a] N. Borghini, P. M. Dinh and J. Y. Ollitrault. *Phys. Rev. C*, **66** 014905, 2002.

[Bor04a] N. Borghini, J.-Y. Ollitrault. *Phys. Rev. C*, **70** 064905, 2004.

[Bor06a] N. Borghini, J.-Y. Ollitrault. *Phys. Lett. B*, **642** 227, 2006.

[Bra00a] J. Brachmann, S. Soff, A. Dumitru, H. Stöcker, J. A. Maruhn, W. Greiner, L. V. Bravina and D. H. Rischke. *Phys. Rev. C*, **61** 024909, 2000.

[Che08a] M. Cheng, P. Hegde, C. Jung, F. Karsch, O. Kaczmarek, E. Laermann, R. D. Mawhinney, C. Miao, P. Petreczky, C. Schmidt and W. Soeldner. *arXiv: 0811.1006*, 2008.

[Chi08a] C. B. Chiu, R. C. Hwa and C. B. Yang. *Phys. Rev. C*, **78** 044903, 2008.

[Cle09a] C. Gombeaud and J.- Y. Ollitrault *arXiv: 0907.4664*.

[Coo74a] F. Cooper and G. Frye. *Phys. Rev. D*, **10** 186, 1974.

[Dis03a] G. Dissertori, I. Knowles, and M. Schmelling. *Quantum Chromodynamics - High Energy Experiments and Theory*, Oxford Universidy Press, 2003.

[Don04a] X. Dong et al. *Phys. Lett. B*, **597** 328, 2004.

[Dum07a] A. Dumitru, E. Molnar, Y. Nara. *Phys. Rev. C*, **76** 024910, 2007.

[Eid04a] S. Eidelman et al. *Phys. Lett. B*, **592**, 2004.

[Fey69a] R.P. Feynman. *Phys. Rev. Lett.*, **23** 1415, 1969.

[Foa75a] L. Fo$\grave{A}$. Phys. Rep., **22** 1, 1975.

[Fri03a] R. J. Fries, B. Müller, C. Nonaka, S. A. Bass. *Phys. Rev. Lett.*, **90** 202303, 2003.

[Fri04a] R. J. Fries. *J. Phys. G*, **31** S379, 2005.

[Koc08a] V. Koch. *arXiv: 0810.2520*, 2008.

[Gre03a] V. Greco, C. M. Ko, P. Levai. *Phys. Rev. Lett.*, **90** 202302, 2003.

[Gre04a] V. Greco and C. M. Ko. *Phys. Rev. Lett.*, **70** 024901, 2004.

[Gyu01a] M. Gyulassy, I. Vitev and X. N. Wang *Phys. Rev. Lett.*, **86** 2537, 2001.

[Gyu02a] M. Gyulassy, I. Vitev, X. N. Wang and P. Huovinen. *Phys. Lett. B*, **526** 301, 2002.

[Ham95a] F. Grassi, Y. Hama, and T. Kodama. Phys. Lett. B, **355** 9, 1995.

[Huo01a] P. Huovinen, P. F. Kolb, U. Heinz, P. V. Ruuskanen and S. A. Voloshin. *Phys. Lett. B*, **503** 58, 2001.

[Huo03a] P. Huovinen. "Private Communication (2003)."

[Huo05a] P. Huovinen. *Nucl. Phys. A*, **761** 296, 2005.

[Hwa00a] R. C. Hwa and Y. Wu. Phys. Rev. C, **60** 054904, 1999.

[Hwa03a] R. C. Hwa, X. N. Wang. *World Scientific, Singapore*, 2003.

[Hwa03b] R. C. Hwa and C. B. Yang. *Phys. Rev. C*, **67** 064902, 2003.

[Hwa04a] R. C. Hwa and C.B. Yang. *Phys. Rev. C*, **70** 024904, 2004.

[Jeo02a] S. Jeon, and S. Pratt. *Phys. Rev. C*, **65** 044902, 2002.

[Jeo00a] S. Jeon and V. Koch *Phys. Rev. Lett*, **85** 2076, 2000.

[Kar02a] F. Karsch. *Nucl. Phys. A*, **698** 199, 2002.

[Kar06a] F. Karsch. *arXiv:hep-lat/0601013.*

[Kol00a] P. F. Kolb, J. Sollfrank and U. Heinz. *Phys. Rev. C*, **62** 054909, 2000.

[Kol03a] P. F. Kolb, U. Heinz. *nuch-th/0305084.*

[Kol03b] P. F. Kolb. *Phys. Rev. C*, **68** 031902, 2003.

[Lin02a] Z. W. Lin, C. M. Ko. *Phys. Rev. Lett.*, **89** 202302, 2002.

[Lin05a] Z. W. Lin, C. M. Ko, B. A. Li, B. Zhang and S. Pal. *Phys. Rev. C.*, **72** 064901, 2005.

[Liu08a] W. Liu and R. J. Fries. *arXiv: 0805.3721.*

[Mei06a] M. Yu, J. Du, and L. Liu. *Phys.Rev. C*, **74** 044906, 2006.

[Mar98a] S. Margetis. *STAR Note 0367*, 1998.

[Mat03a] H. S. Matis et al. *Nucl. Instru. Method A*, **499** 802, 2003.

[Mil03a] M. Miller. *PhD thesis*, Yale University, 2003.

[Mol03a] D. molnar and S. A. Voloshin. *Phys. Rev. Lett.*, **91** 092301, 2003.

[Old04a] M. Oldenburg et al. *J. Phys. G*, **31** S437, 2004.

[Oll92a] J.-Y. Ollitrault. *Phys. Rev. D*, **46** 229, 1992.

[Oll93a] J.-Y. Ollitrault. *Phys. Rev. D*, **48** 1132, 1993.

[Oll95a] J.-Y. Ollitrault. Nucl. Phys. A, **590** 561C, 1995.

[Oll07a] *Phys. Rev. C*, **76** 024905, 2007.

[Rei04a] W. Reisdorf, H.G. Ritter. *Ann. Rev. Nucl. Part. Sci.*, **47** 663, 1997.

[Har03a] J. Harris et al. *Nucl. Instrum. Meth. A*, **499** 624, 2003.

[Hah03b] H. Hanh et al. *Nucl. Instrum. Meth. A*, **499** 245, 2003.

[RHIC] *http://www.rhic.bnl.gov/.*

[Sat00a] H. Satz. *Rept. Prog. Phys.*, **63** 1511, 2000.

[Sin02a] Y. M. Sinyukov, S. V. Akkelin, and Y. Hama. Phys. Rev. Lett, **89** 052301, 2002.

[Sjo94a] T. Sjostrand. *Comp. Phys. Commun.*, **82** 74, 1994.

[Sor97a] H. Sorge. *Phys. Lett. B*, **402** 251, 1997.

[Sor97b] H. Sorge. *Phys. Rev. Lett.*, **78** 2309, 1997.

[Sor99a] H. Sorge. *Phys. Rev. Lett.*, **82** 2048, 1999.

[Sor09a] P. Sorensen. *arXiv: 0905.0174.*

[Sto81a] H. Stöcker, M. Gyulassy, J. Boguta. *Phys. Lett. B*, **103** 269, 1981.

[Sto86a] H. Stöcker and W. Greiner. *Phys. Rept.*, **137** 277, 1986.

[Sto05a] H. Stöcker. *Nucl. Phys. A*, **121** 750, 2005.

[Tan08a] A. Tang. *arXiv: 0808.2144*.

[Tho02a] J. H. Thomas. *Nucl. Instru. Method A*, **478** 166, 2002.

[Vol96a] S. Voloshin and Y. Zhang. *Z. Phys. C*, **70** 665, 1996.

[Vol98a] A. M. Poskanzer and S. A. Voloshin. *Phys. Rev. C*, **58** 1671, 1998.

[Vol00a] S. A. Voloshin and A. M. Poskanzer. *Phys. Lett. B*, **474** 27, 2000.

[Vol02a] D. Molnar, S. Voloshin. *Phys. Rev. Lett.*, **91** 092301, 2003.

[Vol06a] S. A. Voloshin. *arXiv: nucl-ex/0701038*, 2006.

[Vol06b] S.A. Voloshin. *Phys. Lett. B*, **632** 490, 2006.

[Vol09a] S.A. Voloshin, A. M. Poskanzer and R. Snellings arXiv:0809.2949

[Wan92a] X. N. Wang, M. Gyulassy. *Phys. Rev. Lett.*, **68** 1480, 1992.

[Wan98a] X. N. Wang. *Phys. Rev. C*, **58** 2321, 1998.

[Wan01a] X. N. Wang. *Phys. Rev. C*, **63** 054902, 2001.

[Wil74] K. G. Wilson. *Phys. Rev. D*, **10** 2455, 1974.

[Zhi07a] Z. Li, N. Li, L. Liu and Y. Wu. *Int. J Mod. Phys. E*, **16** 3347, 2007.

Presentations and publication List

Presentations

1. Study of the Number of Quark Scaling of v_2 at High Transverse Momentum (oral)
   APS April Meeting 2010, Washington DC, February 13-17, 2010.

2. Event Anisotropy at STAR (oral)
   RHIC & AGS Annual Users' Meeting, New York, USA, July 7-11, 2009.

3. PID v2 and v4 in Au+Au collisions at 200 GeV at RHIC (poster)
   Quark Matter 2009, Knoxville, TN, March 29 - April 4, 2009.

4. PID v2 and v4 in Au+Au collisions at 200 GeV at RHIC (oral)
   Winter Workshop on Nuclear Dynamics, Big Sky, Montana, USA, February 1-8, 2009.

5. Relative v_2 fluctuation in High-Energy Nuclear Collisions (poster)
   Quark Matter 2008, Jaipur, India, Feb. 4-10, 2008.

6. Longitudinal scaling property of the charge balance function in in Au+Au collisions at $\sqrt{s_{NN}} = 200$ GeV (poster)
   Quark Matter 2008, Jaipur, India, Feb. 4-10, 2008.

7. Boost-invariance and multiplicity dependence of charge balance function in π^+p and K^+p collisions at $\sqrt{s_{NN}}$ =22 GeV (oral)
   XXXV International Symposium on Multiparticle Dynamics, Czechoslovakia, August 9-15, 2005.

8. The property of Charge Balance Function (oral)
   The 9th Particle Physics Conference, Chongqing, China, May 9-13, 2005.

Publication list

1. **N. Li**, Z. M. Li, Y. F. Wu. "Longitudinal boost invariance of the charge balance function in hadron-hadron and nucleus-nucleus collisions", *Phys. Rev. C*, **80** 064910, 2009.

2. Yanping Huang, **N. Li**, Jiaxin Du, Zhiming Li and Yuanfang Wu. "Two-particle azimuthal angle correlations and azimuthal charge balance function in relativistic heavy ion collisions", *Phys. Rev C*, **79** 054912, 2009.

3. J. Du, **N. Li**, and L. Liu. "Narrowing of the charge balance function and hadronization time in relativistic heavy-ion collisions", *Phys. Rev C*, **75** 021903, 2007.

4. A. Feng, **N. Li**, J. Fu and Y. Wu. "Rapidity dependence of charge fluctuations and correlations in hadronic nuclear collisions", *International Journal of Modern Physics A*, **22** 2909, 2007.

5. Li Zhiming, **Li Na**, Liu Lianshou and Wu yuanfang. "Pseudorapidity and transverse momentum dependence of charge balance in Au + Au collisions at $\sqrt{s_{NN}} =$ 200 GeV", *International Journal of Modern Physics E*, **16** 3347, 2007.

6. Du Jiaxin, **Li Na** and Liu Lianshou. "On the relation between the width of charge balance function and hadronization time in relativistic heavy ion collision", *International Journal of Modern Physics E*, **16** 3355, 2007.

7. M.R. Atayan et al, (EHS/NA22 Collaboration). "Boost invariance and multiplicity dependence of the charge balance function in π^+p and K^+p collisions at $\sqrt{s_{NN}} =$ 22 GeV", *Phys. Lett. B*, **637** 39, 2006.
   Primary authors: **Na Li**, Yuanfang.Wu, Lianshou Liu.

8. **N. Li** and Y. Wu. "Boost Invariance and Multiplicity Dependence of the Charge Balance Function in π^+p and K^+p collisions at 22 GeV", *AIP Conf. Proc.* **828** 113, 2006.

9. B. I. Abelev *et al.*, STAR Collaboration. "Longitudinal scaling property of the charge balance function in in Au + Au collisions at $\sqrt{s_{NN}} = 200$ GeV",
   Primary authors: **Na Li**, Zhiming Li and Yuanfang Wu.
   Accepted by Phys. Lett. B.

10. B. I. Abelev *et al.*, STAR Collaboration. "The breaking of number of constituent quark scaling at high p_T in Au+Au collisions at $\sqrt{s_{NN}} = 200$ GeV",
    Primary authors: D. Gangadharan, **N. Li**, S.S. Shi, A.H. Tang, Y.F. Wu.
    STAR internal review

Acknowledgements

I would like to express my deep and sincere gratitude to my supervisor, Professor Yuanfang Wu, who guide me to the field of high energy physics. Her wide knowledge and her logical way of thinking have been of great value for me. Her understanding, encouraging and personal guidance have done great help to both of my work and life.

I am deeply grateful to my supervisor, Professor Nu Xu, for his important support throughout my work. He introduced me to the field of flow study, and his impressive ideals and concepts deepen and further my understanding. His unique sight of view always gives remarkable influence on me.

I wish to express my warm and sincere thanks to Scientist Aihong Tang, who gave me important guidance during my first steps into flow studies. His knowledge and working gain my great respect. I really enjoy a happy time when work with him.

I would like to show my soulful acknowledgement to Professor Liu Lianshou who just left us. He offered lots of help when I started my research. I still remember that he insisted on discussion when he was ill. His scientific attitudes and spirits will drive me towards the scientific achievement forever!

I would like to thank all the professors, staffs and classmates in Institute of Particle Physics, they help me a lot during this work. And I wish to extend my thanks to Berkeley RNC group, Brookhaven STAR group, bulk-correlation physics working group and Flow discussion group, they offer much help when I work in STAR collaboration.

Thanks Professor Art Poskanzer, Professor Sergei Voloshin, Professor Fuqiang Wang, Professor Huanzhong Huang, Dr. James Dunlop, Dr. Jerome Lauret and Dr. Paul Sorensen for the valuable discussions and help on my work.

Thanks to Zhiming Li, Jinghui Chen, Yuting Bai, Hua Pei, Shengli Huang, Lijuan Ruan, Yifei Zhang, Xin Dong, Zebo Tang, Yichun Xu, Xinhua Shi, Shusu Shi, Xiaoping Zhang, Fu Jin, Hao Qiu, Yi Zhou, Xuan Li, , Xiaofeng Luo, Mingmei Xu, Hui Liu, Jiaxin Du, Meijuan Wang, Kejun Wu Liling Zhu, and Yanping Huang for their help on both

work and life.

Thanks to all my friends.

I owe my loving thanks to my dear parents. Thanks for all their love and their confidence in me when I meet trouble. Without their encouragement and understanding, I won't be here.